The Sensor Based Manipulation of Irregularly Shaped Objects with Special Application to the Semiconductor Industry

by

Vivek Anand Sujan

Bachelor of Science in Mechanical Engineering
California Institute of Technology (1996)

Bachelor of Arts in Physics and Mathematics
with minor in Computer Science
Ohio Wesleyan University (1996)

Submitted to the
Department of Mechanical Engineering
in partial fulfillment of the requirements for the degree of

Master of Science in Mechanical Engineering

at the

Massachusetts Institute of Technology

June, 1998

Signature of Author ______________________
Department of Mechanical Engineering
May 8, 1998

Certified By ______________________
Steven Dubowsky
Thesis Supervisor

Accepted By ______________________
Ain A. Sonin
Chairman, Departmental Graduate Committee

The Sensor Based Manipulation of Irregularly Shaped Objects with Special Application to the Semiconductor Industry

Submitted to the Department of Mechanical Engineering
on May 8, 1998, in partial fulfillment of the requirements for the degree of
Master of Science in Mechanical Engineering

by

Vivek Anand Sujan

Abstract

A Robot Assisted Crucible charging System (RACS) has been proposed in the automation of the crucible packing process in the CZ semiconductor wafer production procedure, involving the delicate manipulation and placement of polycrystalline silicon nuggets, into a stiff and fragile fused silica crucible. Two of the key elements in this design have been described in this thesis, a non-intrusive nugget and crucible surface geometry acquisition module, and a nugget placement and packing algorithm.

A non-contact 3-D surface geometry measuring system has been developed based on the principal of optoelectronic active laser triangulation after a thorough investigation of a range of non-intrusive range sensing methodologies. This system measures both the nugget geometry profile and the internal crucible geometry profile, with a resolution of 1mm.

Additionally, a novel on-line, multidimensional, flexible packing algorithm has been developed based on a principal of "Virtual Trial and Error" and extensively tested by simulation for cost function optimization. Four general cost function principals are tested in six critical combinations, in a two dimensional simulation of the packing algorithm using random non-convex polygons. The final cost function choice of lowest fit is shown to have the best performance index. For general comparison, the algorithm with all six packing schemes, has been applied to random sized rectangular object packing.

This final packing algorithm scheme has been applied to a simulation of the 3D case, that compares well with the expected performance of human packing. These key technology components and requirements have been successfully demonstrated in order to provide for a feasible solution for a Robot Assisted Crucible charging System.

Thesis Supervisor:	Dr. Steven Dubowsky Professor of Mechanical Engineering

Acknowledgements

I would like to thank my academic and research advisor, Prof. S. Dubowsky, for guiding me over the course of the past two years, for pushing me to reach farther, for teaching me what it takes, for believing in and trusting me, and for giving me my freedom to explore the fascinating world of machine vision. It is through his tutelage and his friendship that I have learnt how to be strong in the face of adversity and how to see the big picture. His drive and love for technology has helped us transform a concept into reality and see the fruits of our efforts come to life.

Next, I would like to thank Shit-Etsu Handotai, Co. Ltd. of Japan, for giving us the opportunity and resources necessary in order to carry out the research presented here, and help explore and refine a new window of technology application. I would also like to thank my project colleagues Joe Calzaretta, Tony Leier and Melissa Tata, for providing the support and friendship during both the tough and facile times over the past two years. Many thanks to Mike Mulqueen for being the big brother that I never quite had, who understood and cared through times of both sadness and joy, who was always there when I needed him and for whom I will always be there.

It is Prof. B. Andereck and Prof. L.T. Dillman, of Ohio Wesleyan University, Prof. Erik K. Antonsson and Prof. J Burdick, of Caltech, that helped guide and set me on the track of academic research. It is through their direction, patience and support that I have learned to believe in myself and in realizing the dreams that otherwise would have been unachievable. With their friendship and brilliance that, over the course of the past several years, I have learnt how never to give up and to continue on to the next level in search for excellence.

And yet none of this could have ever been done without my kind yet strong mother, and my firm but loving father. It is through their love and optimism for life that I have learnt how never to feel weak, how never to feel down, how never to be boastful, and how never to accept defeat. It is they who have taught me love, patience, courage, discipline and honor. It is they who have taught me that the challenges of life are what makes it all worthwhile. It is they who have taught me how to be a man and that there is always another round.

Finally, I would like to thank the Almighty, for blessing me with the opportunities to explore this wonderful world of ours. This thesis is dedicated to the memories of my grandmother Sati H. Sujan.

Table of Contents

List of Figures

Chapter 1. Introduction

1.1. *Motivation*

The continual push towards higher productivity in the manufacturing industry has lead to the automation of many manual tasks. The progress of the solid state device technology since the invention of the transistor in 1948 has depended not only on the development of device concepts but also on the improvement of materials. Integrated circuits made today, are the result of a considerable breakthrough in the growth of pure, single crystal silicon (Si). The requirements on the growing of device grade semiconductor crystals are more stringent than those for any other materials in that both single large crystals and high purity levels (on the order of 1 part in 10 billion) are required. Such purities require careful handling and treatment of the material at each step of the manufacturing process. Elemental Silicon and Germanium are obtained by chemical deposition of compounds such as GeO_2, $SiCl_4$ and $SiHCl_3$. Once the semiconductor material has been isolated and preliminary purification steps have been performed, it is melted and casted into ingots, which are then broken down into smaller nuggets, typically with the aid of a tungsten mallot. Upon cooling from the casting process, the Si or Ge is polycrystalline where the atoms are arranged in a diamond lattice over small random regions of the ingot.

A common technique for growing single crystals involves selective cooling of the molten material so that the solidification occurs along a particular crystal direction. Adding a small "seed" crystal at the end being cooled first enhances crystal growth. This technique, commonly called the *Czochralski* (CZ) method, is widely used in growing Si, Ge and some of the compound semiconductors. After the growth of the entire monocrystalline semiconductor ingot, a diamond blade is used to precision cut semiconductor wafer slices.

In cooperation with the Tokyo Institute of Technology and Shin-Etsu Handotai (SEH) Co. Ltd., a leading silicon wafer producing company in Japan, the Field and Space Robotics Laboratory at MIT, has designed and tested parts of a Robot Assisted Crucible charging System (RACS) that performs the tasks required to load (charge) a fused quartz crucible with polycrystalline silicon nuggets for the CZ semiconductor wafer production process. Protection of the crucible from damage, minimization of contamination, and maintaining the required charge density are key constraints during the process. The factory system design requirements are listed in Table 1-1 [Dubowsky].

Table 1-1 : Factory System Requirements

SYSTEM REQUIREMENTS	EXPECTED PERFORMANCE
TECHNICAL FEASIBILITY: Utilize commercially available technology	All components in system utilize technology commercially available
RELIABILITY: Low system downtime	Substantial unplanned downtime of the system expected less than once every 5 years
ECONOMICS: Cost less than manual packing with three year return on investment	$356,000 annual savings (1 year return on investment)
CONSISTENCY & PRODUCTIVITY: Obtain a packing density at least as good as that from manual packing with consistency	Robotic system is more consistent than manual packer and has possibility of obtaining a higher packing density with important financial impact*
OPERATOR SAFETY: Minimal risk of serious injury	Requires simultaneous operator error and equipment error to result in potential injury
FACTORY SPACE: Approximately the same space requirements as manual packing	Space should be about equal to manual packing for same production rate

The task focuses on charging an 18" crucible (giving 125mm diameter wafers) with a total charge weight of 70kg (including the crown). Due to the economical advantage of larger wafer diameters, future extension to 36" crucibles (for 300mm diameter wafers) is important and hence design scalability is critical. Figure 1-1 describes the general charging process characteristics and rules. The process is initiated with the placement of a bed layer of small/medium sized nuggets. After filling the lower hemispherical section of the crucible, wall contact nuggets are critically placed to avoid planar contacts, which could otherwise result in nuggets sticking to the crucible walls during the melting phase. Such a case is undesirable and costly, as it requires temperature increases to dislodge such "stickers". With each outer ring of nuggets, a central bulk fill is required consisting of nuggets of all sizes. This incremental layer build up is carried out till 10cm below the top of the crucible. At this stage a crown build up is initiated, consisting primarily of larger nuggets. Typical crown heights for an 18" crucible range between 3" to 5" above the crucible lip.

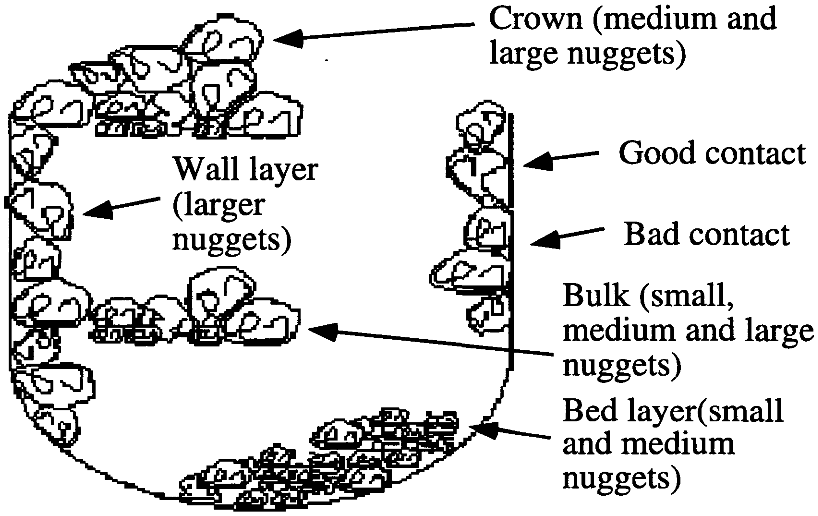

Figure 1-1 : Crucible charging constraints [Dubowsky]

1.2. System Level Approach

While feasible, a RACS does require some technical development. Table 1-2 lists the main technical challenges presented by the RACS project and the solution approach for the respective challenge.

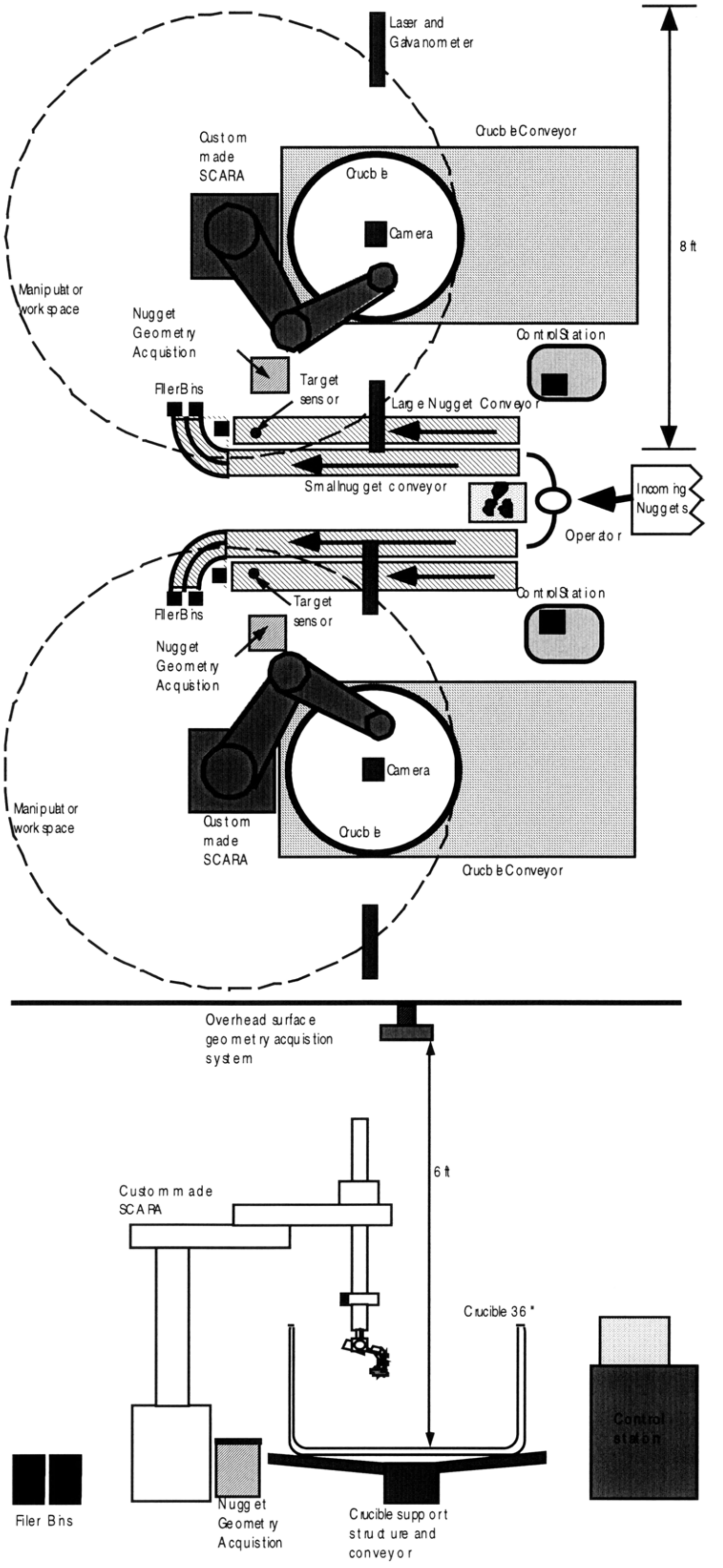

Figure 1-2 : General factory layout

The RACS system integrates either one or two charging subsystems and a nugget feeding station (see Figure 1-2). Each charging subsystem consists of a robot, a controller and 3-D-vision systems. Each crucible is charged by its own SCARA type robot with at least a 36'' reach and 24'' stroke. This allows for crucible sizes up to 36". The nugget geometry acquisition area and a crucible are placed within the robot's workspace. The nugget profile is acquired by first acquiring the nugget in a successful grasp [Leier] (See Figure 1-3) and then passing over the first 3-D-vision system. Centered above the crucible is the second 3-D-vision system that obtains the crucible topography. A novel packing algorithm based on the concept of Virtual Trial and Error has been created, which then optimizes the position of the nugget within the current crucible topography. A hybrid position and force control algorithm for the delicate manipulation of the rigid object in a rigid and fragile environment [Calzaretta] directly places the nugget within the crucible. With each layer of wall nuggets, a layer of bulk fill nuggets is then placed [Leier] (See Figure 1-3).

Table 1-2 : Key Technical Challenges

Key Areas	Requirements	Solution
Detailed geometry of nugget and crucible charge shapes.	1 mm spatial resolution of nugget surface and current crucible level	3-D vision systems that will scan the nuggets and the crucible surface
Grasping of highly irregular nugget shapes	Nugget sizes range from 10 cm^3 (500g) to pebbles.	Vacuum gripper and bulk bin.
Delicate robotic control of irregular nuggets	The nuggets must be precisely located and the crucible must not be damaged	Combining traditional control regimes with Base Torque / Force (BaST) control
Packing of highly irregular nuggets in crucible	Proper wall contact and high packing density	A packing algorithm determines the optimal nugget placement

The charging process is broken down into two main sections. First, the large and medium nuggets that are placed against the crucible wall and in the crown will be grasped by a set of triangulated suction cups at the end of a seven degree of freedom

SCARA manipulator. Second, the small nuggets will be placed within the crucible in bulk using a bulk-filling bin. Figure 1-3 illustrates the basic operation of the system [Leier].

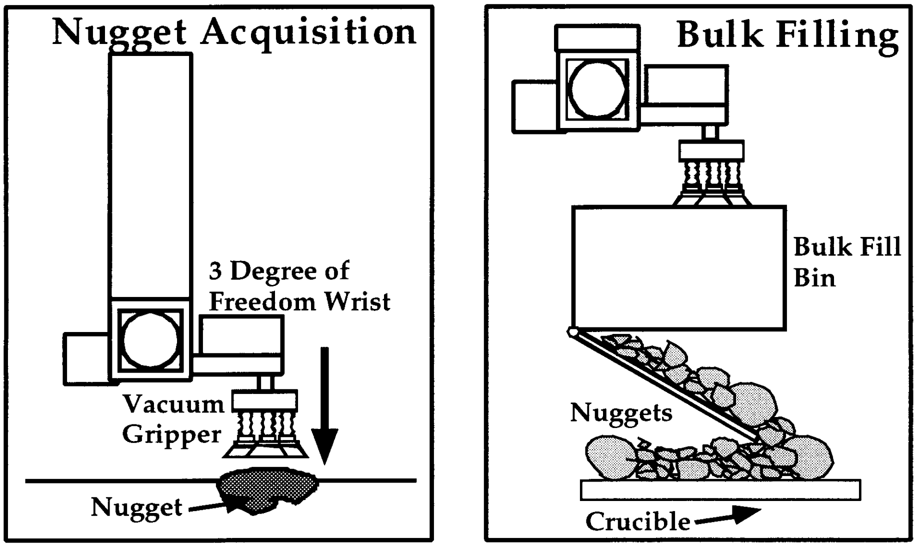

Figure 1-3 : Nugget grasping and bulk filling [Leier]

A RACS would go through the following procedure to charge a given crucible:

- The system initializes and nuggets are sorted by the operator.
- A bed layer is formed using smaller nuggets only in bulk fill.
- An overhead vision system scans the crucible surface geometry.
- A nugget scanning system scans each grasped nugget.
- The packing algorithm uses the geometries obtained to find an acceptable placement solution, used by the manipulator to delicately place the nugget [Calzaretta].
- After a wall layer is built, the center of the crucible is filled to the wall level. Nuggets are placed in batches, rather than individually [Leier].
- Alternating wall and fill levels are completed with visual scanning until the top of the crucible is reached.
- A crown of larger nuggets is made. Nuggets are placed individually as before.

1.3. Vision Systems - Literature Review

The field of 3-D machine vision is a well and extensively studied field. 3-D surface geometry acquisition is important for a wide variety of applications. Several classes of macroscopic problems, such as long distance landscape via radar, and earth surface elevation via satellite laser altimeters, are well solved. Technology for the accurate and rapid microscopic determination of surface geometry without contact is still at a moderately undeveloped stage [Hsueh]. Most of such systems either do not resolve less than 25 microns or have small stand off distances while maintaining the 25-micron resolution at slower speeds. More exotically, non-intrusive methods to obtain atomic resolution systems have been extensively developed, but suffer from slow speeds, extremely small stand off distances (nanometers) and short operating ranges due to limited ranges of motion of the piezoelectric actuators [Kleindiek]. Currently all methods to obtain 3-D non-intrusive visual data of an environment (both micro and macroscopic) can be broken down into active triangulation, holographic interferometry (phase shift measurement), radar (time of flight), lens focus and Moiré techniques [Besl; Antonsson; Hsueh]. A detailed review in which several of the above methods are discussed and compared has been published [Jarvis]. All methods suffer from drawbacks such as missing parts, computational complexity, time-consuming in improvement of signal/noise ratio, limited indoor applications, limited to highly textured or line structured scenes, limited surface orientation, and limited spatial resolution. The triangulation scheme is the most simple method, and could eliminate most of the above problems provided an intense enough energy source could be available. Capturing the third dimension through model free range finding is of great utility in 3-D scene analysis. This can resolve many of the ambiguities of interpretation arising from lack of correspondence between object boundaries and inhomogeneities of intensity, texture and color.

One of the first areas for concern in the evolution of a robot design is the need to provide the system with sufficient situational awareness to support intelligent movement. The first step towards this end consists of the acquisition of appropriate information regarding ranges and bearings to nearby objects, and the subsequent interpretation of that data. The industrial environment provides new constraints and limitations to the applicability of usual techniques such as difficult environment, cost and compactness. Active methods where a beam of light is superimposed to the naturally lighted scene greatly simplify the signal processing to be done to recover distance information [Antonsson]. Among the various methods described in the literature (as mentioned above and described in chapter 2), active triangulation has been selected as an attractive approach that has the potential to evolve towards a low-cost 3-D vision system [Rioux], with desired resolution, speed and field of view. Such a system consists of a light source (usually a laser), a scanning mechanism to project the light spot onto the object surface, and position sensor with a collecting lens looking off axis for the light spot.

1.4. Packing Algorithms- Literature Review

There has been substantial research in the area of design and analysis of algorithms for bin packing, which can be found in operations research, production engineering, systems engineering and automation, and machine vision literature. Several reviews on the current work done in this area have been performed [Coffman; Dowsland; Li; Whelan]. Such algorithms can be divided into either off-line processing [Berkey; Han; Hwang; Kenyon; Pargas; Sarkar; Whelan] or on-line processing [Azar; Chao;

Cheng; Coffman; Galambos; Geogis; Grove; Li; Portmann; Schiermeyer; Shor]. In the former case the objects to be packed are all presented together and the packing algorithm is applied to all objects simultaneously. In the latter case, each object is presented individually to the packing algorithm, without allowing for rearrangement or shifting. Optimum placement is hence achieved on a case-by-case method. Further, off-line and on-line bin packing research address one, two or three-dimensional problems for structured objects such as rectangles and parallelepipeds, or for unstructured objects with complex shapes.

Problems involved in the automated packing and nesting of irregular shapes are both of theoretical importance and considerable industrial importance. The ability to manipulate objects under visual control is one of the key tasks in the successful implementation of robotic, automated assembly and adaptive material handling systems [Whelan]. To automate this part of the manufacturing process an automated material handling systems that combines machine vision techniques and flexible packing strategies, needs to be developed.

For the RACS system, intelligent nugget placement planning is crucial since it directly determines the charging density and process cycle time. Since each nugget is dealt with on a case by case method, an on-line bin-packing algorithm would be required. Additionally, which considers the geometrical structure of the individual nuggets and the processing time constraints, an efficient, on-line, three-dimensional bin-packing algorithm for irregularly shaped objects is required.

A computationally efficient 2-D on-line packing algorithm for arbitrary shapes is described in [Whelan and Bachelor]. 3-D on-line packing is explored [Portmann], but is constrained by parallelepiped shaped boxes. An on-line algorithm with performance ratio of O(log 1/ε) is designed in [Azar and Epstein], but is limited to rectangles of minimum width ε. A multidimensional version of the bin-packing problem is demonstrated [Chang], limited to d-dimensional boxes, but runs in O(n) time where n is the number of objects packed. Further, an on-line algorithm with *lookahead*, also limited to the one-dimensional case where minimization of the number of bins is the optimization goal is presented [Grove]. The case of the constrained rectangle packing problem using simulated annealing have been studied [Geogis, Petrou and Kittler]. A similar algorithm where seven possible shapes of various sizes are considered [Pargas and Jain]. Although the method of simulated annealing is classically an off-line approach, it can be modified to perform in an on-line aspect. This proves to be computationally highly intensive. Reverse fit algorithms [Schiermeyer] for multidimensional packing require a sorted list of objects in terms of specified dimensions. Additionally, [Coffman] explores the results of shelf packing of regular objects (a modified version of the one-dimensional bin packing problem). Several researchers [Cheng] have explored the results of robot manipulation of irregular sized packages in the packing environment. These applications have been developed specifically for d-dimensional parallelepiped shapes and does not transfer to arbitrary shaped objects. A model based method for non-convex polygons is discussed by [Stoyal *et al.*], but is limited to two-dimensions and can be computationally intensive.

1.5. Thesis Purpose

This thesis describes the design and implementation of two of the four main technical challenges described in Table 1-2, namely the 3-D geometry acquisition system and the packing algorithm for the placement of irregular shaped nuggets in.

The vision system of a RACS gathers the data that is required by the packing algorithm. After being grasped, the nugget shape and orientation and the surface geometry of the crucible are measured and processed by the vision system. This data is processed by the packing algorithm to find an optimum location for nugget placement. This area is identified as one that requires detailed feasibility studies. Based on the system requirements laser triangulation is chosen as the vision system method [Besl]. The complete RACS vision system consists of two major subsystems:

- Nugget Geometry Acquisition (NGA) - 3-D surface geometry of a nugget and its orientation with respect to the manipulator is determined for processing by the packing algorithm
- Crucible Surface Geometry Acquisition (SGA) - The crucible and its internal surface structure are measured while the manipulator/robot is not intruding the Field Of View (FOV). The scan consists of two phases :

  (i) A crude scan with low resolution updated every 10 nugget cycles

  (ii) A high resolution scan every cycle in the area modified

Additionally, a novel on-line nugget placement planning strategy has been developed for placing nuggets in a crucible. The strategy utilizes only the raw range image data provided by the 3-D vision system, does not require feature extraction of range images and performs all computations in a virtual environment determined by the acquired data. The result is a computationally simple and effective solution to the nugget placement problem that can be applied to general d-dimensional problems. This work has contributed towards the design of intelligent handling systems, by creating an efficient multi-dimensional on-line model free bin packing solution for arbitrarily shaped objects. The algorithm is designed around the principles and combinations of next fit, first fit, lowest fit and minimum area fit. The effects of these variations are explored in order to determine the computational placement solution in O(n) time.

1.6. Thesis Outline

Chapter 1 describes the general system level approach for the automation of the charging process of crucibles in the classical CZ semiconductor wafer production system. A description of the main technical challenges involved are outlined. Two of the technical challenges are further defined and a literature survey is outlined.

Chapter 2 describes the purpose of the vision system required for the task and the range sensing methodologies for the 3-D profile acquisition of both the nugget and the internal surface of the crucible. Discussions on illumination methods, detectors and vision system characteristics are delineated.

Chapter 3 describes the design and implementation of the NGA and crucible SGA systems. Details on system calibration, image post-processing criteria and data extraction are described. Finally, the system data results are presented.

Chapter 4 describes the nugget placement algorithm. Simulation of the algorithm is done in both 2 and 3 dimensions. Working parameters and results of the simulations are presented. Lastly, the issue of nugget placement stability is addressed.

Chapter 5 describes the system integration for the factory level design and relation of coordinate frames between the crucible, the manipulator, the nugget geometry acquisition system and the crucible surface geometry acquisition system. Further, the communication between the manipulator control station and the vision/packing control station is addressed. Finally, future work on the system level design is discussed.

Chapter 2. Vision Systems

2.1. Introduction

Analyzing and understanding visual information is probably the most complex task that an intelligent machine can perform. Once analyzed and understood, visual information provides the most useful knowledge that an intelligent machine can possess about its environment. The science of machine vision can be reduced to three fundamental tasks: image transformation, image analysis and image understanding. Image transformation involves the conversion of light intensity images to electrical signals used by a computer. Image analysis of the electronic image involves extraction of such image information as object edges, regions, boundaries, colors and texture. Finally, once the image is analyzed, a vision system must interpret, or understand what the image represents in terms of knowledge of the environment.

Image-analysis technology can be broken down into several fundamental topics that are common to all such systems. These topics include edge detection and line finding (including tracking, model matching and template matching), region splitting, region growing, color definition and texture primitive identification. Similarly image understanding or machine perception can be exceedingly difficult and include issues such as interpretation of line drawings, understanding shadows and cracks, and formulating motion.

Range finding and navigation (a combination of image transformation, analysis and understanding) are particularly important to the field of robotics, such as in the case of industrial bin picking where locating objects in a parts bin, without prior knowledge of exact locations, is the objective. Many 2-D image-understanding problems are caused by the lack of range information. There are methods to infer depth from 2-D cues, which result in 2½-D images.

However, 2½-D analysis does not provide the range information required for most real-world operations. The third dimension involves determining the distance, or range, of all the points that define a scene, the result being a range map image that complements the 2-D image.

For the RACS, understanding the system requirements, the available technology and the consolidation of the two in the area of vision systems is critical to the performance of the factory system. This chapter brings together these system requirements (Section 2.2), describes the available technology from the perspective of imaging methods (Section 2.3), and illumination hardware (Section 2.4).

2.2. Performance Goals

The primary considerations for an industrial vision system are cost, speed, accuracy and reliability. To pay for itself, an industrial vision system must outperform the human labor it replaces in all these categories. In most cases, the vision system must perform a real-time analysis of the image to compete with humans. Table 2-1 lists the system requirements for the RACS vision system as determined by the factory and charge requirements [Dubowsky].

Table 2-1 : System Requirements

1. Data Resolution and Accuracy	Approximately 1mm (but system design dependent)
2. Data Acquisition and Processing Rate	Nugget Geometry Acquisition - 2.5 s Crucible Surface Geometry Acquisition - 4.5 s
3. Ease of System Interfacing	System interfacing must not require the development of non-existent hardware in order to perform the required task--Simplicity
4. Costs	Factory system vision costs ≤ $25000.
5. Size	Physical size constraints?

The vision system of a RACS gathers the environmental data that is required by the packing algorithm. After being grasped, the nugget shape and orientation, and the internal surface geometry of the crucible are measured and processed by the computer vision system. The packing algorithm utilizes the three-dimensional data or a range map of the profiles for the nugget and the internal crucible surface, in order to determine a satisfactory location for the nugget within the current crucible state (Chapter 4). System modularity and physical independence of the two vision modules is a desired secondary requirement, so as to facilitate possible individual modifications based on the higher level packing requirements.

2.3. Range Sensing

Range-imaging sensors collect three-dimensional coordinate data from visible surfaces in a scene and can be used in a wide variety of automation applications, including object shape acquisition, bin picking, robotic assembly, inspection, gauging, mobile robot navigation, automated cartography, and medical diagnosis (biostereometrics). The image data points explicitly represent scene surface geometry as sampled points. The inherent problems of interpreting 3-D structure in other types of imagery (where 3-D data is obtained based on 2-D cues) are not encountered in range imagery although most low level problems, such as filtering, segmentation, and edge detection, remain. Most optical techniques for obtaining range images are based on one of the following principles.

2.3.1. Active Triangulation

Probably, one of the most commonly seen methods for the acquisition of three-dimensional data, is the laser triangulation method. A structured light source, such as point, line or color-coding, is used to illuminate the object and either one or more cameras (possible for stereoscopic vision systems) detect the reflected light (see Figure 2-1). The location and orientation of the cameras (determined precisely with calibration) yields an equation that determines the 3-D location of the illuminated point. A line of illumination is consequently broken up into a series of discrete points. By scanning the entire object, a 3-D map of the object can be acquired.

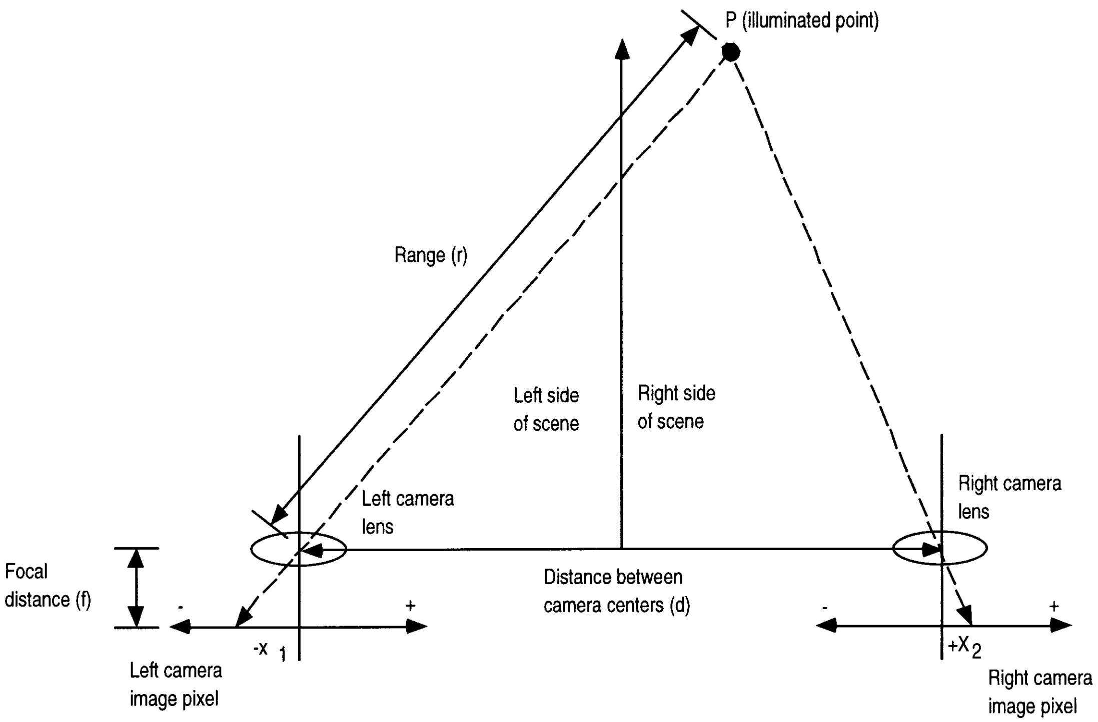

Figure 2-1 : General triangulation layout

2.3.1.1. Model I - Point wise Triangulation Using 2 Stereoscopic Cameras

Figure 2-2 is a plan view and Figure 2-3 is an orthographic view of the system.

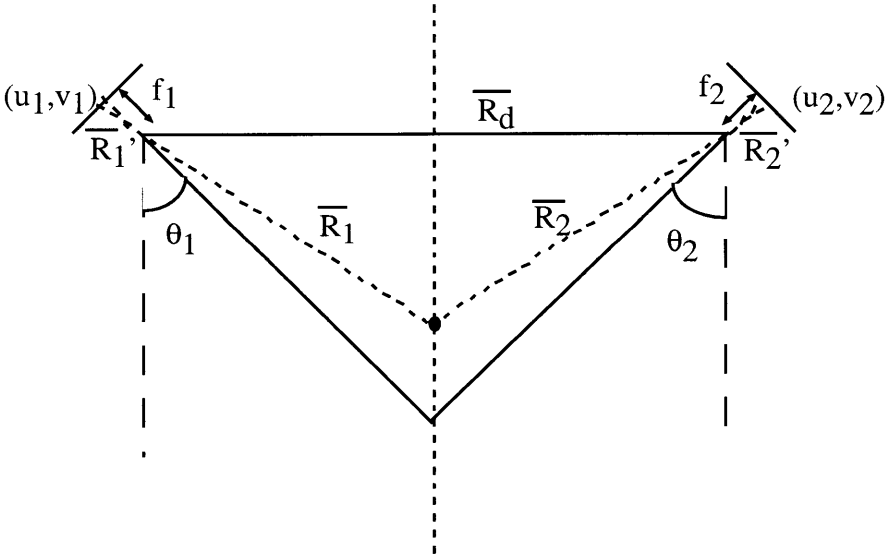

Figure 2-2 : Model I - Plan view

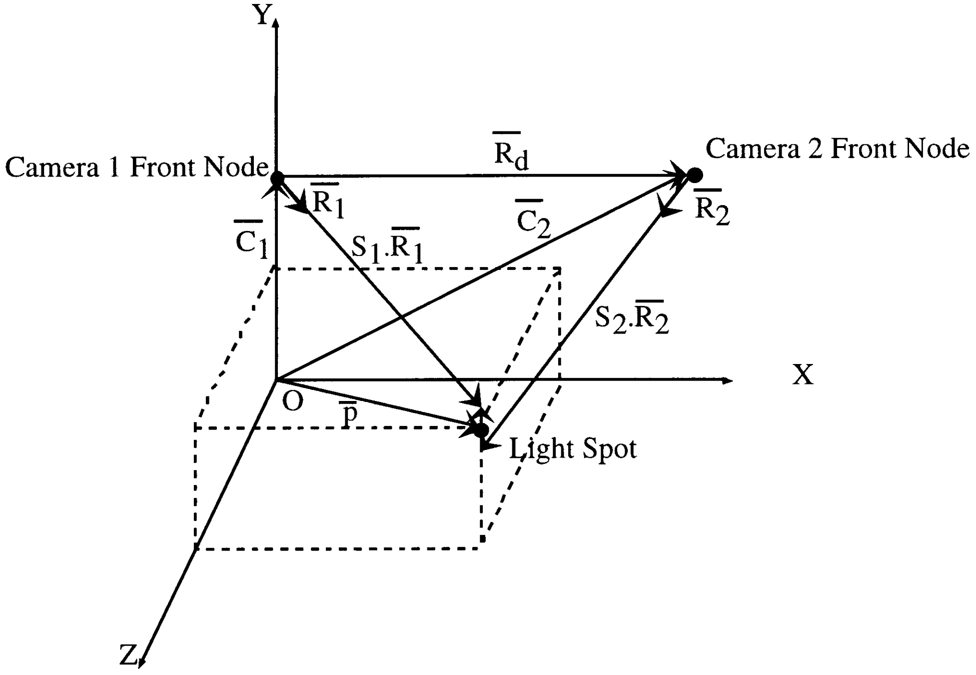

Figure 2-3 : Model I - Orthographic view

The origin of the world coordinate system is set at the front node of the lens of camera #1. The X-axis passes through the front node of the lens of camera #2. The Y-axis points out of the paper vertically. The Z-axis is positive in the direction of the laser beam, which originates between the two cameras. In this design, the position/orientation of the laser is not critical but provides for a simple solution to the stereo matching problem. This methodology is equally effective for passive triangulation systems. The v-axis of the detector (Figure 2-2) is assumed to be parallel to the world Y-axis (though this requirement can be mathematically relaxed). Optimization of the combined field of view requires that $\theta_2 = -\theta_1 = 45^{\circ}$. The distances between back nodes of the lenses and the detectors are the principal distances f_1 and f_2. The 2-D coordinates measured on the image planes are (u_1,v_1) and (u_2,v_2) in the detectors own coordinate systems. These can be transformed into vectors $\mathbf{R_1}$ and $\mathbf{R_2}$ in the world coordinate system with:

$$\overrightarrow{R_1} = M_1 \overrightarrow{R_1'} \qquad \overrightarrow{R_2} = M_2 \overrightarrow{R_2'} \qquad (2\text{-}1)$$

where

$$M_1 = \begin{bmatrix} \cos\theta_1 & 0 & -\sin\theta_1 \\ 0 & 1 & 0 \\ \sin\theta_1 & 0 & \cos\theta_1 \end{bmatrix} \qquad M_2 = \begin{bmatrix} \cos\theta_2 & 0 & -\sin\theta_2 \\ 0 & 1 & 0 \\ \sin\theta_2 & 0 & \cos\theta_2 \end{bmatrix} \tag{2-2}$$

And $\mathbf{R'_1}$ and $\mathbf{R'_2}$ are in the detector coordinate systems:

$$\vec{R_1'} = \begin{Bmatrix} u_1 \\ v_1 \\ f_1 \end{Bmatrix} \qquad \vec{R_2'} = \begin{Bmatrix} u_2 \\ v_2 \\ f_2 \end{Bmatrix} \tag{2-3}$$

In theory, extensions of $\mathbf{R_1}$ and $\mathbf{R_2}$ should intersect each other because they are directions of light rays that come from the same light source located at **p**. In practice, any misalignment or error in the system can result in skew. The vector **e** is defined to be the skew vector such that $|\mathbf{e}|$ is the shortest distance between the two lines (Figure 2-3). In order to find **e**, we define:

$$\mathbf{e}(S_1,S_2)=S_1\,\mathbf{R_1} - S_2\,\mathbf{R_2} - \mathbf{R_d} \tag{2-4}$$

Minimizing $|\,\mathbf{e}(S_1,S_2)|$ with respect to S_1 and S_2 gives (see Appendix A):

$$S_1 = \frac{(\vec{R_1}.\vec{R_d})(\vec{R_2}.\vec{R_2}) - (\vec{R_2}.\vec{R_d})(\vec{R_1}.\vec{R_2})}{(\vec{R_1}.\vec{R_1})(\vec{R_2}.\vec{R_2}) - (\vec{R_1}.\vec{R_2})(\vec{R_1}.\vec{R_2})} \qquad S_2 = \frac{(\vec{R_2}.\vec{R_d})(\vec{R_1}.\vec{R_1}) - (\vec{R_1}.\vec{R_d})(\vec{R_1}.\vec{R_2})}{(\vec{R_1}.\vec{R_2})(\vec{R_1}.\vec{R_2}) - (\vec{R_2}.\vec{R_2})(\vec{R_1}.\vec{R_1})} \tag{2-5}$$

e can thus be calculated. The coordinates of the spot **p** are defined to be at the center of **e** giving:

$$p = \tfrac{1}{2}\,(S_1 R_1 + S_2 R_2 + R_d) \tag{2-6}$$

Since the system can determine the 3-D coordinates of a point anywhere in the combined field of view (FOV), and measure points in any order, it is possible to analyze the data stream from the system during acquisition and adaptively scan the light spot in response, allowing for data oversampling and the collection of spatially dense data in regions of interest [Hsueh; Antonsson]. The resolution, based on the nominal viewing volume is found to be:

$$\frac{\vec{R_d}/2}{\mathit{Detector\ \ resolution}} \tag{2-7}$$

2.3.1.2. **Model II - Point wise Triangulation Using 1 Camera**

An alternative approach is shown in Figure 2-4 and Figure 2-5. A single camera is aligned along the Z-axis with the center of the front node of the lens located at (0,0,0). At a baseline distance b to the left of the camera (along the negative X-axis) is a light source (typically a laser) sending out a beam or plane of light at a variable angle α relative to the X-axis baseline. The point (x,y,z) is projected onto the digitized image at the pixel (u,v), controlled by the focal length of the lens, f. The measured quantities (u,v,α) are used to compute the 3-D coordinates of the illuminated point given by (see Appendix B):

$$[x \;\; y \;\; z] = \frac{b}{f \cdot \cot(\alpha) - u} [u \;\; v \;\; f] \qquad (2\text{-}8)$$

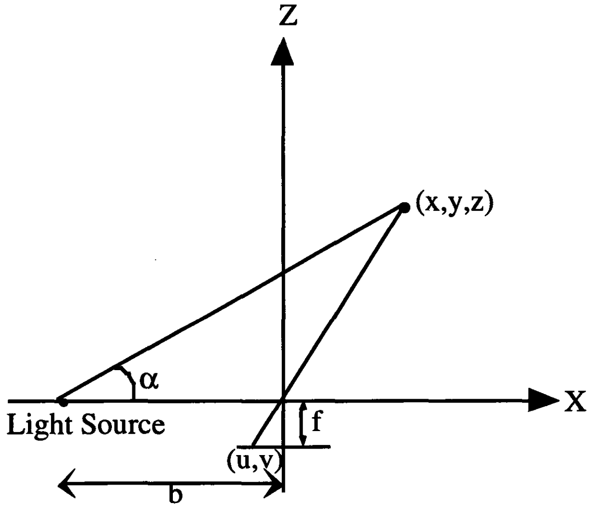

Figure 2-4 : Model II - Plan view

Note that for any given focal length, f, and baseline distance, b, the resolution of this triangulation system is only limited by the ability to accurately measure the angle α, the horizontal position u and the vertical position v.

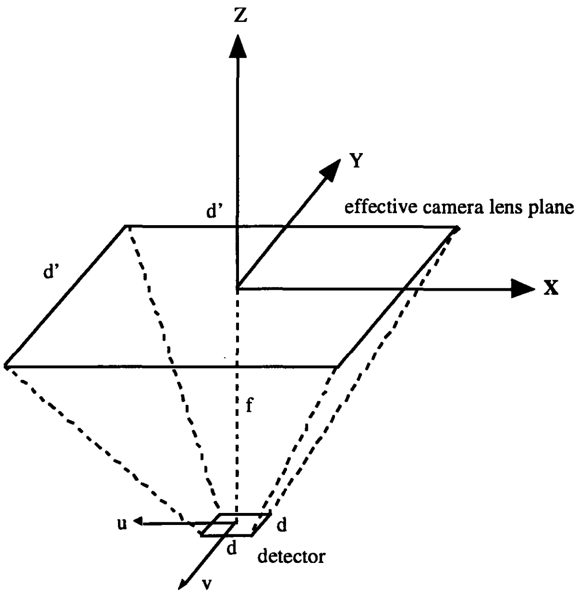

Figure 2-5 : Model II - Orthographic view

As before the X and Y system resolutions are given by:

$$\frac{R}{Detector\ \ resolution} \qquad (2\text{-}9)$$

Where R is the width of the projected image onto the detector. The vertical resolution, given an incident laser angle α, image width W, and n-pixel detector resolution is given by (Figure 2-6):

$$\delta Z = (W \tan \alpha) / n \qquad (2\text{-}10)$$

The value R and the value of the resolutions (δX, δY, δZ) may differ for the two image plane coordinates (u,v) as the number and size of each detector pixel is not equal in the two axes.

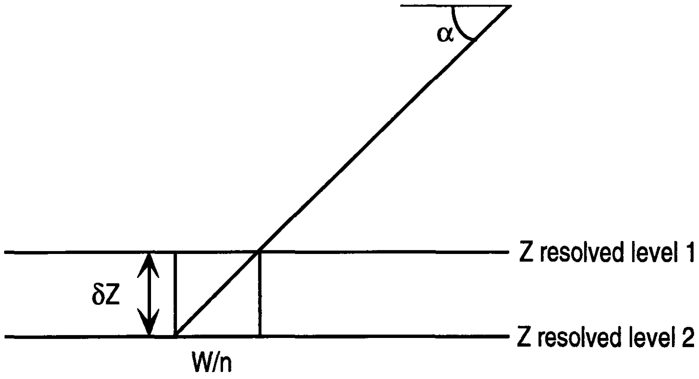

Figure 2-6 : Model II - Z resolution

2.3.1.3. **Model III - Point wise Triangulation with Reference Coordinates**

A third perspective on the method of active triangulation [Rioux] is outlined in Figure 2-7. A beam of light originates from position d along the X-axis, projects at an angle θ_0, and defines a reference point (d/2,l) that is used for calibration. At the origin, a lens of focal length f, focuses the light on a position sensor aligned parallel to the X-axis and in focus at -fl/(l-f) along the Z-axis. It is assumed that d, l, and f are known and are respectively the distance between the scanner axis of rotation and the principal point of the lens, the distance between the common axis of projection and detection (0,-d,0) and the reference point, and focal length of the lens. Under rotation of the scanner, the light beam rotates to another angular position $\theta_0 + \theta$ (θ is negative in Figure 2-7). The spot of light on the position sensor moves from df/(2l-2f) to location p due to the intersection of the projected light beam with the object surface at x,z. By trigonometry the relationship between the coordinates (x,z) and the parameters of the geometry is:

$$x = d \cdot p\left[p + \frac{f \cdot l(2l \cdot \tan\theta + d)}{(l-f)(d \cdot \tan\theta - 2l)}\right]^{-1} \qquad z = -d\left[\frac{p(l-f)}{f \cdot l} + \frac{2l \cdot \tan\theta + d}{d \cdot \tan\theta - 2l}\right]^{-1} \qquad (2\text{-}11)$$

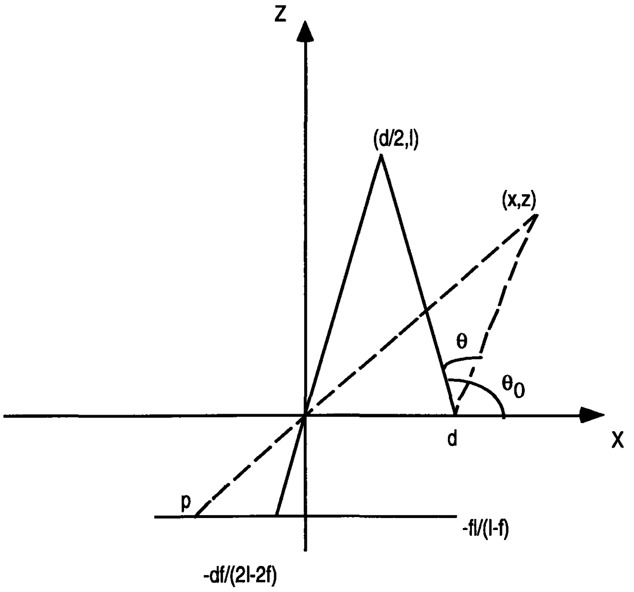

Figure 2-7 : Model III - Plan view

2.3.2. Holographic Interferometry

In this method, after precise calibration, the system can be used to measure object point distances by Michelson's Interferometry methods (see Appendix B). A beam of light (for illumination) is split and forced to travel via two separate routes to a detector. The number of fringes formed in the detector is related to the optical path difference in the two light rays. Compensators are placed to account for phase differences that may have arisen due to the optics in the system. The location of the point can then be determined to within a fraction of the illumination wavelength used [Hecht]. Holographic interferometry uses coherent light to produce interference patterns due to the optical frequency phase differences in different optical paths.

Phase Comparison is an alternative method still based on the principles of interferometry. Here a series of known frequencies are emitted and split as above, traveling via two paths to the detector (one of which reflects off the object and the other off a mirror). The phase difference between the two interfering beams determines the object distance to be n x wavelength + f, where f is the fraction due to the phase difference. By using a series of known frequencies to cover a large spectrum, n can then be determined.

2.3.3. Radar

This method is also known as pulse timing. Here a pulse of known frequency is emitted to the object. The Time Of Flight (TOF) is the time taken for the pulse to reach the object and reflect back, which determines the distance of the object or point. Unlike the above two this method is primarily feasible for large-scale range finding. This method is also used in Doppler Techniques of range finding for moving objects The basic time/range equation for radars is:

$$v.t=2r=\text{round trip distance} \tag{2-12}$$

where v is the speed of the signal propagation, r is the distance to a reflecting object, and t is the transit time of the signal travelling from the radar transmitter to the reflecting object and back to the radar receiver. For imaging laser radars, the unknown scene parameters are the range r, the surface reflection coefficient ρ, and the angle $\theta=\cos^{-1}(\mathbf{n}.\mathbf{l})$ between the visible surface normal, **n**, and the direction **l** of the radar beam. Ignoring atmospheric attenuation, all other relevant physical parameters can be lumped into a single function K(t) that depends only on the radar transceiver hardware. The received power P(t) is then given by:

$$P(t,\theta,\rho,r) = K(t-\tau)\rho \cos\theta / r^2 \qquad (2\text{-}13)$$

This laser radar equation indicates that if 10 bits of range resolution is required on surfaces that may tilt away from the sight line by as much as 60° and if surface reflection coefficients from 1 to 0.002 on the scene surfaces, then a radar transceiver with dynamic range of 90 dB is required.

Versions of the radar concept include amplitude modulation, where a laser beam can be amplitude modulated by varying the drive current at a frequency $f_{AM}=c/\lambda_{AM}$. A phase detector measures the phase difference between the transmitted and the reflected signal to get the range:

$$r(\Delta\phi) = \frac{c\Delta\phi}{4\pi f_{AM}} = \lambda_{AM}\frac{\Delta\phi}{4\pi} \qquad (2\text{-}14)$$

Since relative phase differences are only determined modulo 2π, the range to a point is only determined within a range ambiguity interval r_{ambig}. In the absence of any ambiguity-resolving mechanism, the depth of the field of an AM laser radar is the ambiguity interval:

$$L_r = r_{ambig} = \frac{c}{2f_{AM}} = \frac{\lambda_{AM}}{2} \qquad (2\text{-}15)$$

which is resolved into 2^N parts, for N bits of quantization at the output of the phase detector.

2.3.4. Lens Focus

Using the knowledge of the relations between focal distances and maintaining the focus of an object is another method for range finding. A feedback system determines the change required in inter-lens distances based on the distribution of light from a given object, in order to minimize the spread and maximize the peak of the function. This can then be interpreted to give the object range using the thin-lens equations or the lensmaker formula (Gaussian lens formula):

$$\frac{1}{s_o}+\frac{1}{s_i}=\frac{1}{f}=(n_l-1)(\frac{1}{R_1}-\frac{1}{R_2}) \qquad (2\text{-}16)$$

where s_o and s_i are the focal lengths of the outer and inner lens surfaces respectively, f is the effective focal length, R_i is the radius of curvature of the lens surface, and n_l is the index of refraction of the lens material.

2.3.5. Moiré Techniques

A Moiré pattern is a low spatial frequency interference pattern created when two gratings with regularly spaced patterns of higher spatial frequency are superimposed on one another. In Moiré range imaging sensors, surface depth information is encoded in and recovered from the phase differences. This method is only good for measuring relative distances to surface points on a smooth surface that do not exhibit depth discontinuities. Mathematically, a low spatial frequency interference pattern is created when two higher frequency gratings are superimposed:

$$A(x)=A_1\{1+m_1\cos[w_1x+\phi_1(x)]\}.A_2\{1+m_2\cos[w_2x+\phi_2(x)]\} \qquad (2\text{-}17)$$

where A_i is the wave amplitude, m_i is the modulation index, w_i is the spatial frequency, and ϕ_i is the spatial phases. When this signal is low-pass filtered (LPF) or blurred, only the difference frequency and constant terms are passed:

$$A'(x)=LPF[A(x)]=A_1A_2(1+m_1m_2\cos\{[w_1-w_2]x+\phi_1(x)-\phi_2(x)\}) \qquad (2\text{-}18)$$

For equal spatial frequencies, only the phase difference terms remain, from which surface depth information can be recovered. Under the constraints of bounded surface slope, and smooth surfaces that do not exhibit depth discontinuities, absolute range for an entire Moiré image can be determined if the distance to one reference image is known.

General Moiré Interferometry Methods :

(a) Projection Moiré - A precisely matched pair of gratings is required to be placed in front of the projector and the camera. The projector is located at an angle θ_l and the camera is located at an angle θ_v, relative to the z-axis. The projected light is spatially amplitude modulated by the pitch of the projector grating, creating a spatial carrier image. By viewing these reflected stripes through the camera grating, interference fringes are created at the camera. The camera grating demodulates the modulated carrier yielding a baseband image signal whose fringes carry information about surface shape. If p_o is the period of the projected fringes at the object surface, then the change in z between the centers of the interference fringes viewed by the camera is given by:

$$\Delta z = \frac{p_o}{\tan(\theta_l) + \tan(\theta_v)} \qquad (2\text{-}19)$$

The angular separation of the source and detector is critical to range measurement.

(b) Shadow Moiré - If a surface is relatively flat, shadow Moiré can be used. A single grating of large extent is positioned near the object surface. The surface is illuminated through the grating and viewed directly from another direction

(c) Single Frame Moiré with Reference - The projected grating on a surface can be imaged directly by a camera without a camera grating, digitized, and demodulated using software provided that a reference image of a flat plane is also digitized. Single frame systems of this type are able to resolve range proportional to about 1/20 of a fringe spacing.

(d) Multiple Frame Phase Shifted Moiré - (N-frame) phase shifted Moiré is similar to single-frame Moiré except that after the first frame of image data is acquired, the projector grating is precisely shifted laterally in front of the projector by a small distance increment that corresponds to a phase shift of 360/N degrees and subsequent image frames are acquired. This method resembles quasi-heterodyne holographic interferometry, allows for an order of magnitude increase in range accuracy compared to conventional methods.

2.3.6. Comparison

Table 2-2 list the main comparison features of the five methods described above.

Table 2-2 : Qualitative comparisons I of range sensing methodologies

	Active Triangulation	**Holographic Interferometry**	**Radar : TOF, AM, FM**	**Lens Focus**	**Moiré Techniques : Projection, Shadow, Single Frame + ref, Multiple Frame**
Resolution/Accuracy	>2.5 µm (with specific hardware)	>3µm (0.4nm theoretical)	>>100µm	>1mm	>11µm
Data Acquisition rate	<10M pixels/s	<1K points/s	<<100K pixels/s	<60K pixels/s	<100K pixels/s
Depth of Field	O(10 meters) -> O(mm)	O(100 meters) -> O(mm)	>>O(mm)	O(100mm) -> O(meter)	>O(100mm)
Limitations	Detector noise, data processing power	Alignment, system noise	High res. + data acq. Rate -> small depth of field	lens quality/ positioning/ measuring	only for smooth surfaces high resolution -> small d.o.f.

Table 2-3 qualitatively indicates how the methods compare with respect to active triangulation in terms of availability, interfacing, size, cost and safety. From Table 2-1, where the system requirements were outlined and from Table 2-2 and Table 2-3, the method of active triangulation is selected for the purpose of solving the requirements of a three-dimensional vision system.

Table 2-3 : Qualitative comparisons II of range sensing methodologies

	Active Triangulation	Holographic Interferometry	Radar	Lens Focus	Moiré Techniques
Interfacing	0	-	-	+	0
Availability	0	-	+	0	0
Size	0	-	-	0	-
Cost	0	-	-	-	0
Safety	0	0	+	+	0 (+)

2.4. Illumination Methods

In an optical laser (Light Amplification by Simulated Emission of Radiation), given a system of atoms, in their ground state, it is possible to quantum mechanically excite these states into specific energy states, by impinging it with photons of that specific energy level. The excited atom can then drop back into a lower energy state while emitting another photon, which is in phase with, and has the same polarization of, and propagates in the same direction as, the simulating radiation. When a substantial percentage of the atoms are excited into an upper state, leaving the lower states empty (population inversion), an incident photon of the proper frequency could then trigger an avalanche of stimulated photons-all in phase. The initial wave would build up, so long as there were no dominant competitive processes (like scattering) and that the population inversion could be maintained. In effect, energy could be pumped in to sustain the inversion, and a beam of light would be extracted after sweeping across the active medium. This is the basic governing principal behind the operation of a laser. Further analysis of this phenomenon is beyond the scope of this thesis but considerable literature exists on the above [Hecht].

In order to decide what form of illumination is required for the purpose of active triangulation one must consider the two available alternatives--Laser and White light. Although other non-coherent monochromatic sources of light exist, such as chemical vapor lamps, white light is used to denote all essential non-coherent light sources. Table 2-4 displays a list of comparisons between the two fundamental forms of illumination.

Table 2-4 : Laser and White Light source comparison

Laser	White Light
Large spatial and temporal coherence lengths	Very short coherence lengths
Light is collimated	Light needs collimating
CCD camera can be tuned to selectively pick the laser frequency, leading to the use of multiple lasers	Only brightest spot/line can be picked up by CCD camera
System can be designed around ambient light	System susceptible to ambient light
Relatively easy to maintain object focus	Relatively hard to maintain object focus
Relatively easy to obtain and maintain high intensity	Relatively difficult to obtain and maintain high intensity
Intensity is fairly stable after warm up	Intensity is not stable for the task
Relatively expensive source	Relatively cheap source
Few commercially available and cheap options of frequencies	Relatively easy to select approximate frequency (although harder to reduce the bandwidth to that found in lasers)

In general video cameras do not have the ability to view variations in illumination as well as the human eye. The result is over-saturation, under-saturation or both within a given scene. The results of improper illumination can be rather severe, yielding poor resolution and contrast.

Table 2-5 lists a variety of common ways for illumination setups along with the pros and cons for each methodology. Illumination must be specified considering not only the optics used but also the kind of inspection being performed. Macro lenses and other large optics often gather sufficient light from their environment such that only supplementary light sources are needed. Low power and long working distance optics generally require more structured , higher intensity illumination. Additionally, objects under inspection may exhibit high reflectance, absorption, and specular reflectance. They may also be smooth, rough or vertically textured.

Table 2-5 : Illumination setups

Light Source	Pros	Cons	Type
Diffuse Front Lighting	Minimizes shadows and specular reflections	Surface features less distinct	Fluorescent linears and rings
Bilateral/Angular Diffuse Lighting	Strong relatively even illumination	Dual shadows and glare	Fibreoptic light guides, halogen lamps
Front Ring Guide Illumination	Reduces shadows and relatively even illumination	Circular glare pattern from highly reflective surfaces and can be difficult to mount	Fibreoptic ring light guides
Diffuse Axial/Lateral Illumination	Shadow free, even illumination and little glare	Lower intensity through beam-splitter	Axial illuminators, fibreoptic driven axial adapters
Single Directional, Glancing Incidence	Shows surface defects/topology	Hot spots and severe shadowing	Fibreoptic light guides and halogen lamps
Line Generating Laser	Surface feature extraction	Extremely intense source and absorbed by same colors	Line generating laser diodes

Based on the system requirements, laser light sources are selected in order to successfully perform active triangulation, under variation of environmental parameters. Based on its absorption coefficient, bulk silicon has a bandgap energy at approximately 1.1eV (1μm). This indicates that it absorbs photons with energies equal to or greater than its bandgap energy. Silicon tends to absorb significant amounts of incident light in the visible and ultra violet ranges. Consequently infrared and near infrared illumination sources work within the given tolerances.

Chapter 3. Surface Geometry Acquisition

3.1. Introduction

As outlined in Chapter 1, the RACS system has two main visual problems to solve:

1. Polycrystalline silicon Nugget Geometry and Orientation Acquisition
2. Crucible Surface Geometry Acquisition

The vision system is integrated as a link between the robot manipulator, the nuggets and the crucible. The nugget shape and orientation after being grasped and the surface geometry of the crucible is computed and processed by the vision computer system. The data acquired is processed by the packing algorithm to find a feasible location for nugget placement. Further the system requirements for such a system are outlined in Table 2-1. Based on the range sensing methodologies, illuminations techniques and the detector types (from Chapter 2), two modular 3-D vision systems have been designed and implemented using model II laser triangulation with CCD cameras. The first system is for the internal crucible surface geometry acquisition (SGA) and the second for the nugget geometry acquisition (NGA). Specifications on the hardware used in these two sub-systems are given in Appendix C.

This chapter explores the SGA and NGA designs in greater detail, provides several design options in the conception of the SGA and NGA (Section 3.2) and explains the details behind the scanner and scanner interface technology used for panning the laser, system calibration including intrinsic, extrinsic and timing calibration in order to bring the entire RACS into a single coordinate reference frame (Section 3.3), image extraction (Section 3.4) and presents the results obtained from the systems (Section 3.5).

3.2. System Design Concepts

3.2.1. Surface Geometry Acquisition (SGA)

The selected laboratory design general layout is shown in Figure 3- 1. Design options are shown in Appendix D. Specifications on the design are outlined in Appendix E. It is assumed that the crucible is scanned while the manipulator/robot is not intruding the Field Of View (FOV). The scanning consists of two phases, (i) a crude scan with low resolution that is updated every 10 nugget placement cycles [Tata] and (ii) a high resolution scan every nugget placement cycle in the area that was manipulated (see Figure 3- 2). The high-resolution scans are then patched together to give a larger high resolution map of the entire crucible. Table 3- 1, lists the major SGA components and challenges associated with those components in the system integration.

Table 3- 1 : SGA vision system components

COMPONENTS	DESCRIPTION	FEATURE/CHALLENGE
1. One central overhead camera per crucible	Area of view of camera covers the entire crucible and is mounted directly overhead from an overhead structure	CCD camera requires constant area of view in order to maintain XY (flat plane) resolution
2. Laser light source	Structured laser light projecting a line across the entire crucible is scanned across the crucible	Angle of the beam with respect to the surface being scanned determines the vertical (Z) resolution available
3. Z gantry or FOV adjusting system per camera (vertical compensation)	Vertical positioning system or FOV adjusting optics for the overhead vision system in order to maintained desired area of view	Interfacing challenges include determining current FOV and adjusting accordingly
4. Laser light panning mirrored scanner per laser	Mechanical servo mechanism to position mirror at desired angle in order to facilitate the panning of the laser light across crucible	Angular position can limit vertical (Z) resolution available

Resolution for the vertically uncompensated setup is based on (Eqn 2-8). For the laboratory system design given that the desired, resolution is 1mm in all the x, y and z coordinates, it is now required to determine the design parameters.

- The SGA must be mounted so as to not interfere with the manipulator or infringe on the manipulator work space i.e. at least over 4' high.

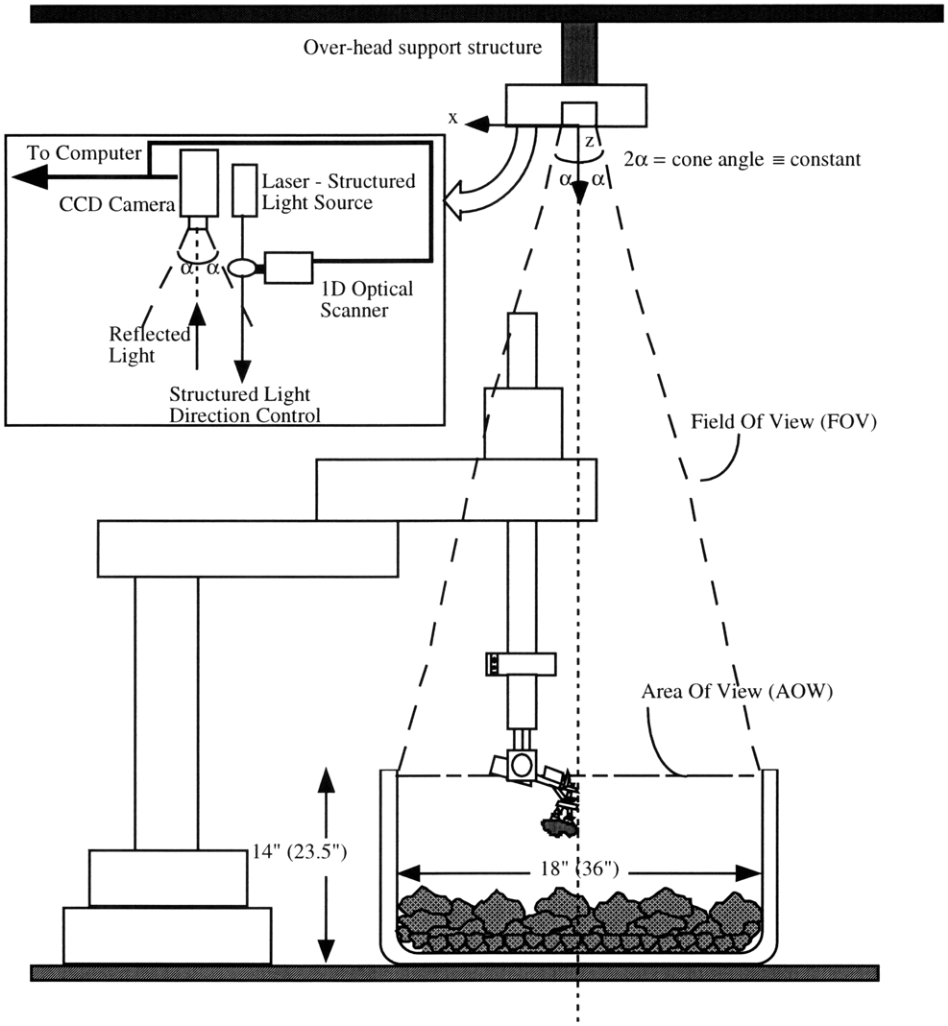

Figure 3- 1 : Overhead SGA vision system layout

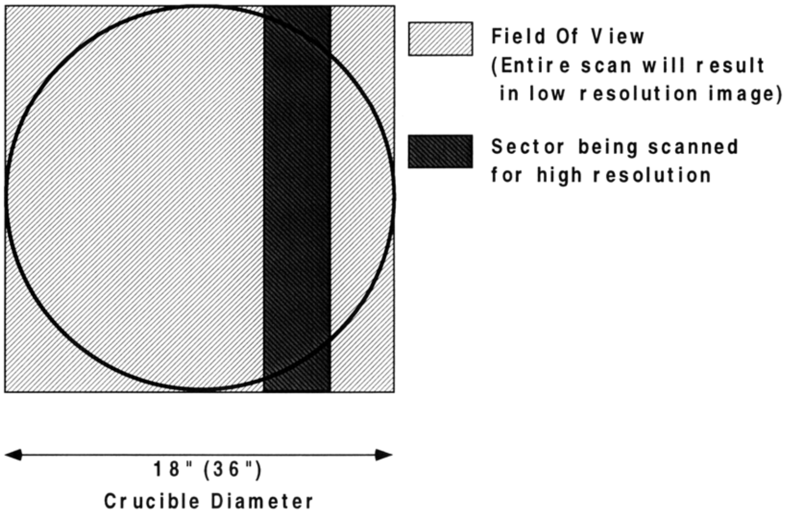

Figure 3- 2 : High and Low resolution scanning

- In order to obtain x,y resolution of 1mm over the entire crucible, the SGA needs to receive collimated or parallel image rays *i.e.* mounted at infinity. However, the converging lens forces an image cone projection onto the CCD plane, resulting in a change of viewing area (see Figure 3- 3). Found simply by trial and error and from accessibility issues, the SGA mounted at 72" above the base of the crucible provides tolerable x,y resolutions of 0.9mm and 1.2mm (based on a CCD with a 500 x 500 pixel grid--see Appendix C) at the top and at the bottom of the crucible respectively.
- With the SGA CCD camera at 72" above the crucible ground, it is found that an effective solution involves using two laser sources and scanners, each scanning half of a crucible (see Appendix E). This method introduces the issue of viewability, as part of the crucible would be in a laser blind zone (due to the crucible walls) for any incident angle greater than 63.4° (determined by the geometry where the incident beam just glances the a top corner of the full crucible and is targeted at the crucible ground center). This beam extends back to a point of intersection on the extended camera lens front nodal plane, 36" away from the camera lens front node.
- Given that the desired z resolution is 1mm, and that the CCD has a 500 x 500 pixel grid, the maximum angle of the incident laser beam, α (where α is defined in Figure 2-4 and Eqn 2-10) for an 18" viewing cross section is 47.5° . This leads to the question of blind spots discussed in section 2.6.3. *i.e.* any surface that has a slope greater than 47.5°, with respect to the camera, cannot be mapped. Further, in order to obtain 1mm z-resolution, a minimum angle of 40.7° is required for the ground plane of the crucible, as the CCD field of view would have increased from 18" to 22.91" (see Figure 3- 3). Additionally, this would force the source to be placed about 83"

away from the camera lens front node along the front nodal plane, causing additional problems of obfuscation by the wall.

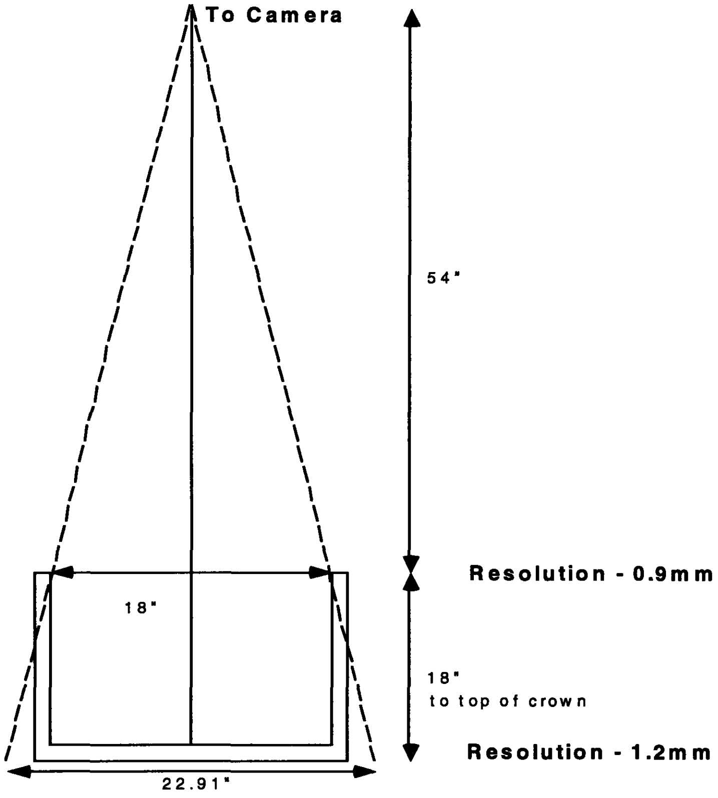

Figure 3- 3 : SGA resolution without vertical compensation

- On the other extreme, laser blind zones can be eliminated by increasing the maximum angle of the incident beam, but the resolution soon blows up (note that the z-resolution is a function of the tan(α) in (Eqn 2-10)).
- In order to compensate for blind spots due to limited angular excursion or poor resolution due to high incident angles, a system level trade off is made. The final system parameters for both the laboratory design and the factory design are listed in Appendix E. Note the improvement by increasing the CCD pixelation.

- A crude / low resolution global scan is anticipated to give a XY resolution of 1.5 cm and will take one second to process for a 18" crucible. Optimally, a factor of two improvement in performance can be expected. Further resolution improvement is achieved by allowing longer scan times. A higher resolution local scan (6" wide band--see Figure 3- 2) is anticipated to give a XY resolution of 1mm and will take 4.5 seconds to process. All times are based on standard video frame rate of 30 frames/s.
- The SGA module is mounted on a custom built 3"x1"x40" basebar, that is cantilevered over the crucible by mounting it on the top flange of a 3" steel pipe, mounted vertically to the floor. The design includes a rotational table (rotab) and a 2-axis gimbal tilt table to give three precision d.o.f. for mechanical extrinsic calibration (to remove image plane yaw, pitch and roll with respect to the manipulator coordinate frame) which is further discussed in section 3.3. The CCD camera and the laser are mounted on precision sliders along the axis of the basebar in order to control the inter camera-laser distance. The moving magnet galvanometer servo is also precision mounted at the laser end allowing the effective inter camera-light source distance to vary from 33" to 39". See Figure 3- 4.

Scanner

The optical scanner used in the SGA is a moving-magnet actuator, i.e. the rotor or working part of the scanner is a magnet. A moving magnet motor has no saturation torque limit and very little electrical inductance. Thus extremely high torque can be generated very rapidly, an essential feature for systems requiring short step response times. However, the peak torque is limited by the mechanical failure limit of the rotor assembly due to stator current in excess of the peak current specification. The rms torque is limited by the maximum power (I^2R losses in the stator coil) the scanner can conduct away. When the maximum rms current has been reached (with adequate heat sinking) the stator has reached its maximum temperature, and thus the motor has reached maximum rms torque level. Since both the torque limit and maximum power that the stator coil can dissipate are very high, extremely high performance can be achieved.

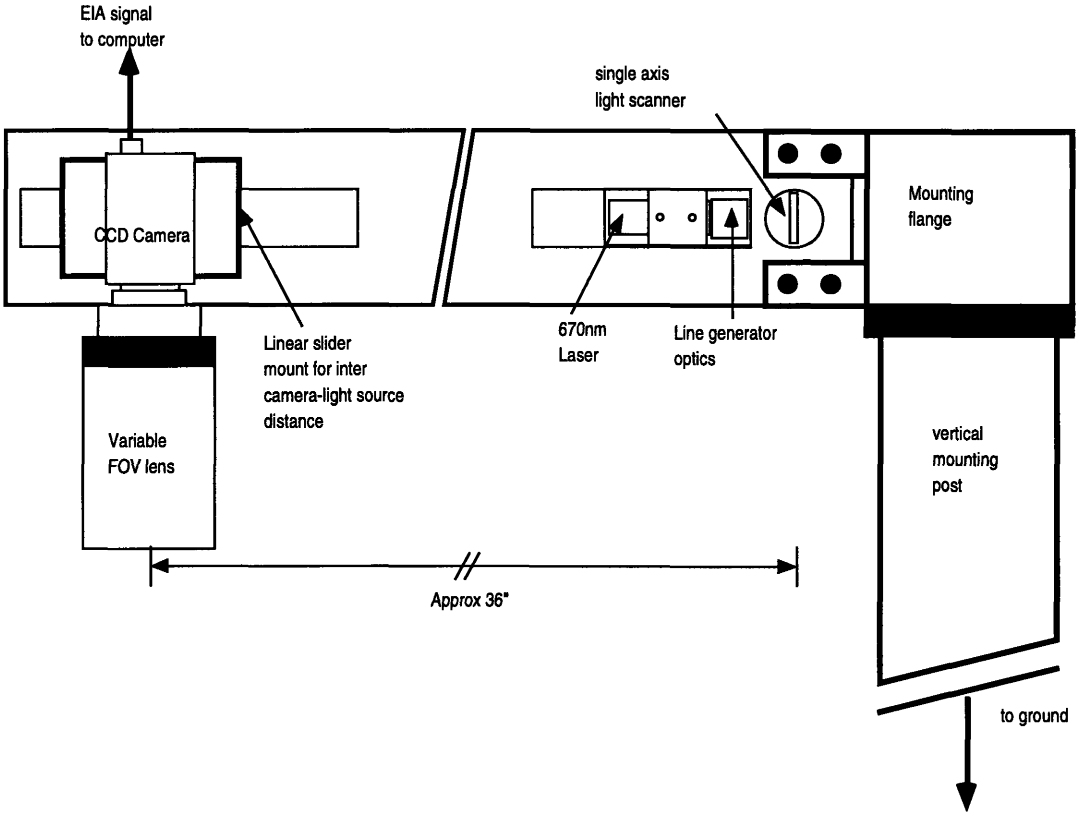

Figure 3- 4 : SGA Mounting Overview

The interface of the scanner is done using a servo amplifier card tuned for an inertial load of 10 g-cm^2 of the mirror. A differential current signal, used by the controller board for position control, is obtained from the capacitive position detector within the scanner. The system accepts analog (-10 to 10V) and digital (0 to 2^{16}) inputs corresponding to an angular excursion of -20 to 20 mechanical degrees. Computer interface is accomplished via the parallel port. As the sample update is limited to 30Hz by the bandwidth of the CCD and framegrabber, scanner performance level due to parallel port interface is not a system bottleneck. However, parallel port signals are of the 8 bit variety, whereas the scanner can perform to a resolution of 16 bits (or an angular resolution of 10 μrad). Based on the resolution requirements of 1mm in X-Y, and scanner to ground center distance (described earlier), on an 18" or 457mm crucible 457 discrete scanner steps are needed or at least 9 bits of resolution, selected to give an angular resolution of 489 μrad over the 18".

To obtain either 9 bits or the entire set of 16 scanner bits of control, a latching digital circuit is designed and implemented. The 8 bit parallel port signal is broken into a 4 bit data and 3 bit address signal, that provides the four sets of 4 bits of data to four quad D-flops, each uniquely enabled by the address bits. In order to avoid four discrete steps at the scanner level, these four quad D-flops outputs were then routed through two octal D-flops that were triggered together by another unique address dumping the final position to the scanner. For every scanner position this requires four output signals to the parallel port of the computer. Once again this does not prove to be a system bottleneck as the CCD, framegrabber and image processing is still the limiting factor at 30Hz. A schematic of the interfacing 8-16 bit converter electronics is given in Appendix F.

3.2.2. Nugget Geometry Acquisition (NGA)

The selected laboratory design general layout is shown in Figure 3- 5. Design options are given in Appendix D. The manipulator is used as the linear translator of the object and passes over the vision system. The object is scanned in real time as it is being moved across the camera; no panning of the laser beam is required of the vision system in order to scan the object. However, issues such as speed must be addressed as the manipulator arm needs to move at a predetermined speed lower than the desired system resolution for continuous motion or will have to move in steps equal to the system resolution for discrete motion. Table 3- 2 lists the major NGA components and challenges associated with those components in the system integration.

Table 3- 2 : NGA vision system components

COMPONENTS	DESCRIPTION	FEATURE/CHALLENGE
1. Central base camera per robot manipulator	Single fixed CCD base camera with constant AOV	Robot manipulator controls both vertical position and horizontal scanning of nugget with respect to camera
2. One laser light source per camera	Structured laser light projecting a line across the entire nugget will be scanned across the nugget	Angle of the beam with respect to the nugget being scanned determines the vertical (Z) resolution available and the maximum measurable slope of the nugget

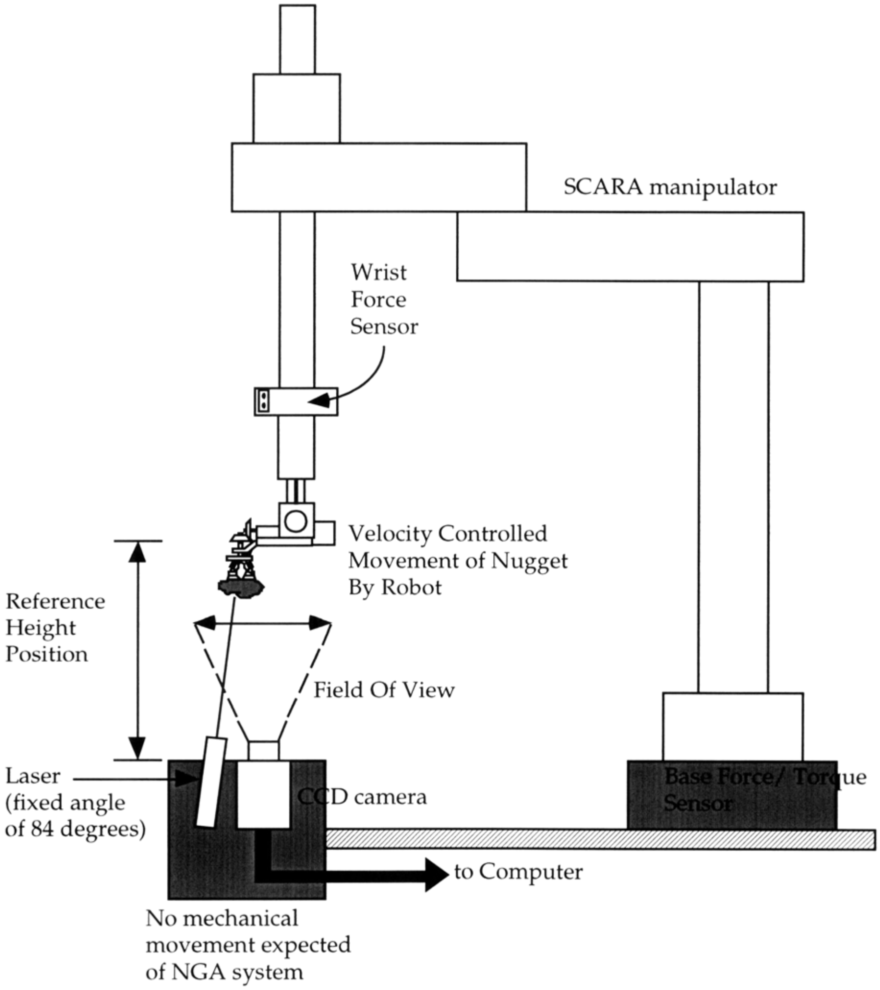

Figure 3- 5 : NGA System Layout

- Based on a known index mark scanning is initiated while the manipulator maintains a constant linear velocity of the nugget across the camera FOV. This velocity is 3 cm/s based on a 1mm XY resolution, nominal nugget size of 3”x3", 2.5 second scan time, and 30 frames/s video rate.
- In order to obtain the desired vertical resolution of 1mm, the incident angle of the laser light with respect to the horizontal, is 81.3° for a 3"x3" area of view (Eqn 2-10), giving a standoff distance of 4", and inter camera-laser distance of 0.6" (b, defined in section 2.3.1) with a 42° view cone. Benefiting from more detailed knowledge (steeper blind zone) of the nugget profile over the lesser known crucible surface geometry is not clearly understood at this time. Consequently more tractable distances can be obtained by using a smaller view cone or decreasing the incident angle. The laboratory system currently uses a 73.1° incident angle for a 6"x6" area to give a standoff distance of 7.8", inter camera-laser distance of 2.4" and 1mm z resolution.

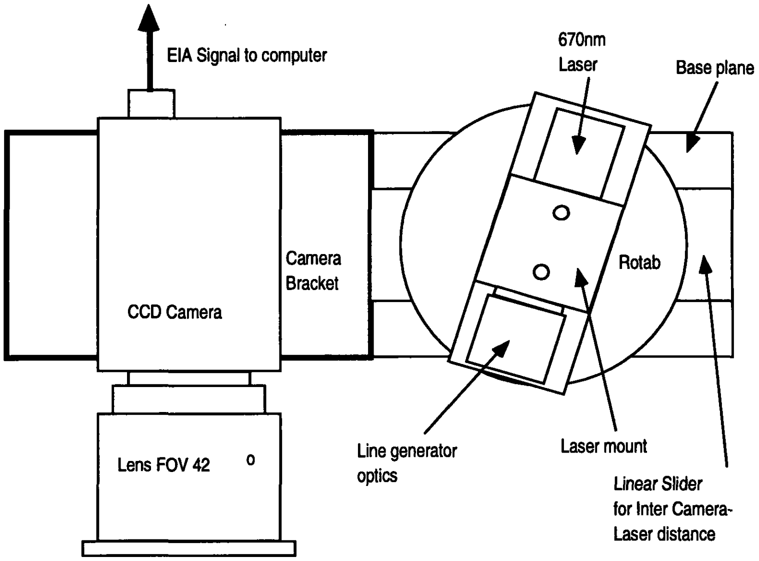

Figure 3- 6 : NGA Mounting Overview

- The NGA module is mounted on a custom-built 2"x1"x6" baseplate that is positioned with respect to the manipulator with the help of vertical upright shafts. The CCD camera is precision mounted with respect to the baseplate that is used as the reference, using a custom fabricated bracket. The angular position of the laser is determined by precision mounting the laser onto an optical rotational table. The inter camera-laser distance is maintained as a degree of freedom by mounting the laser rotab onto a precision slider, orthogonal to the camera image plane, than can be fixed in place with a set of locking bolts. Figure 3- 6 shows an overview of the setup.

3.3. Calibration

3.3.1. Intrinsic Calibration

A perfect lens and a linear detector produces trigonometric relationship between the angle of an incoming light ray and the image plane coordinates (u,v) of the light source (see Figure 3- 7). In practice imperfections in either of the above elements can result in distortion. The purpose of camera intrinsic calibration is to find and map errors of image plane coordinates (u,v) generated by the non-linearities in lenses, detectors and electronics. These errors are then subtracted from the measured values in order to produce accuracy equal to the resolution of the system. In Figure 3- 7, given a known incoming angle γ between the light ray and the principal axis, and a known principal distance f, an "expected" image plane coordinate u can be calculated. Subtracting the u actually measured from the "expected" u, the error in the u direction, E_u, can be found. The error in the v-direction, E_v, can be found similarly, where angle γ is called β.

$$u_{expected} = f\,.\,\tan\gamma, \quad v_{expected} = f\,.\,\tan\beta \tag{3-1}$$

$$E_u = u_{expected} - u_{measured} = f\,.\,\tan\gamma - u_{measured}\ , \tag{3-2}$$

$$E_u = v_{expected} - v_{measured} = f \cdot \tan\beta - v_{measured} \tag{3-3}$$

This scheme assumes that E_u at $\gamma=0$ and E_v at $\beta=0$ are 0. For non-ideal lenses the focal length, f, would have to be mapped as an average given by [Hsueh]:

$$f \approx \bar{f} = \frac{1}{n}\sum_{n}\left|\frac{u_{measured}}{\tan\gamma}\right| \tag{3-4}$$

Using this method, an error map/table can be generated for the detector plane. For every (u,v) pair read in, using binary interpolation, an E_u and E_v can be looked up and compensations can be made. This error becomes critical at and below the sub millimeter and micron levels. The RACS system does not generated such maps due to the lower resolution requirements, but may have to if system parameters and requirements change.

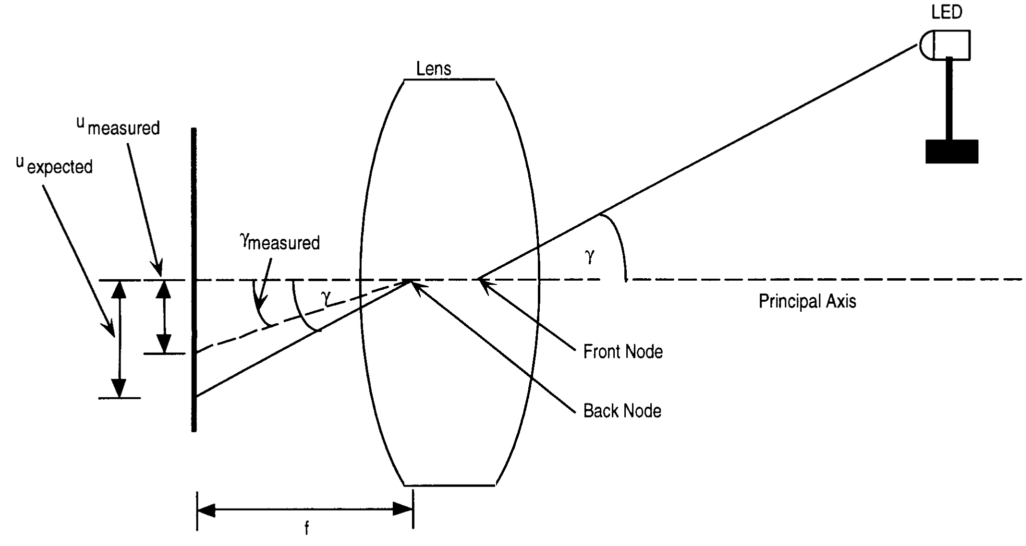

Figure 3- 7 : Relationship of error and angles

3.3.2. Extrinsic Calibration

Based on the triangulation method chosen (model II section 2.3.1) the extrinsic variables in the system which have to be predetermined for (Eqn 2-8) are the focal length, f, and the inter-camera laser distance, b. Using a calibration device consisting of a precision machined (to within 0.001" or 0.025mm) Delrin (very good diffuse reflection of incident 670nm laser light) block with a 1mm step profile and an aluminum guide to position the block (see Appendix G), the NGA is setup on an optical platform to scan the Delrin block. The focal length, f, is solved first, based on the specifications of the optical lens used. The focal length specified by the lens must be compensated to account for bending of the light rays due to the lens. An effective focal length, f, can be trigonometrically computed based on the knowledge of the image size and the half angle of the view cone, both obtained from the lens specifications. This is the focal length of the equivalent pinhole camera used in the mathematical model of the system. Finding the value of b (the inter camera-laser distance measured along the camera lens frontal nodal plane) is done by scanning a "slice" of the calibration object, at a known incident angle β, obtaining image coordinate u from the scan, and applying Eqn 2-8 given f (in number of pixels rather than mm). This scan is done as close to the center of the image plane as possible to eliminate lens distortion at extremities.

Table 3- 3 : Laboratory NGA extrinsic calibrated parameter values

Optical image size (diameter)	6.477mm
Half angle of view cone	20.6°
Effective focal length	8.616mm

If a variable focus lens is used then in general it would not be possible to "read off" the lens focal length value. For a general extrinsic calibration, the following method described for calibrating the SGA would prove to be adequate. Once again, focal length compensation based on (3- 4, needs to be performed for higher resolution systems.

Calibrating the SGA system can prove to be more complex. Given an unknown lens focal length and inter camera-laser distance b, with no certainty in mounting orthogonality with respect to the ground, it is desired to be able to solve for the unknowns. The first intuitive method measures three sets of data points, given the incident laser angle. The z-component of Eqn 2-8, gives two difference equations:

$$z_3 - z_2 = \frac{fb}{f\tan\theta_3 - u_3} - \frac{fb}{f\tan\theta_2 - u_2} \qquad (3\text{-}5)$$

$$z_2 - z_1 = \frac{fb}{f\tan\theta_2 - u_2} - \frac{fb}{f\tan\theta_1 - u_1}$$

and solving for the two unknowns f and b, proves ineffective, giving inconsistent results. This can be primarily an artifact of using a relatively small difference in heights. However, using larger objects yield either focussing problems or parallax problems (differentiating height based on pixel intensities may not possess sufficient resolution).

The second method provides satisfactory results. From Figure 3- 8, we get:

$$l = \frac{g}{\sin\alpha} \qquad (3\text{-}6)$$

$$b = z \cdot \cot\alpha \qquad (3\text{-}7)$$

$$b = b' - l \cdot \cos\alpha \qquad (3\text{-}8)$$

$$z^2 + b^2 = r^2 \qquad (3\text{-}9)$$

$$\frac{\sin(\beta - \alpha)}{\partial h} = \frac{\sin(\pi/2 - \beta)}{r + l} \qquad (3\text{-}10)$$

$$\frac{\sin(\pi - \beta)}{l} = \frac{\sin(\beta - \alpha)}{x} \qquad (3\text{-}11)$$

Where g (measurable), α, β (set to position by scanner) and δh (object height) are known. x is defined as the distance between the intersection points of the two incident rays, at angles α and β, with the extended camera lens front nodal plane. This gives six equations in six unknowns that are not redundant and hence can be solved uniquely.

Table 3- 4 : Laboratory SGA extrinsic calibrated parameter values

Effective focal length, f	15.8 mm
Inter camera-laser distance, b	890 mm
Front node to mounting center, g	153.03 mm
Object height	101.6 mm (4")
Angle α, β	41.2°, 44.5°

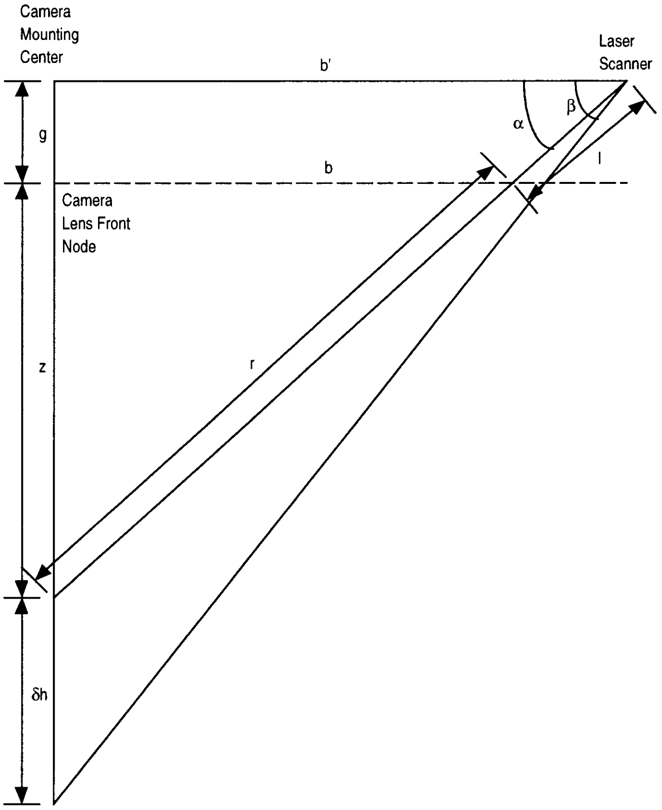

Figure 3- 8 : SGA Extrinsic Calibration Geometry (image not to scale)

Alternatively, using one incident angle to get five equations in five unknowns:

$$b = b' - g \cdot \cot\alpha \tag{3- 12}$$

$$b' = (z + g)\cot\alpha \tag{3- 13}$$

$$(z + g)^2 + b'^2 = (r + l)^2 \tag{3- 14}$$

$$z^2 + b^2 = r^2 \tag{3- 15}$$

$$l = \frac{g}{\sin\alpha} \tag{3- 16}$$

The system of equations is redundant and simplifies to four equations in five unknowns and cannot be solved uniquely.

In the above descriptions it is assumed that the incident angles were known. For the NGA system, this can be read off the rotab that positions the laser and possesses the only rotational degree of freedom (with a bias error of 2.6 milliradians or 0.15 degrees that transfers to a maximum error of 0.5mm) of the system.

For a more general setup, such as the SGA, a galvanometer or reflecting mirror mount needs to be aligned. A calibration rod is used at a distance of 20" from the center of the galvanometer, mounted orthogonal to the base bar (section 3.2.1). The calibration rod consists of 0.025" markings. At a distance of 20" this trigonometrically translates to an angular error of 1.25 mrad, which produces a maximum error of 2.5mm at the crucible ground center for a 72" high and 36" cantilever scanner position (Appendix E). To bring this error down to 0.5mm, higher resolution (0.005") markings are needed on the calibration rod or/and a larger displacement for measurement, and the corresponding ability to read the laser reflection more accurately. Adding a photometer for improved accuracy and higher precision in readings is recommended.

3.3.3. Timing Calibration

The final considerations in calibration are timing for the NGA-manipulator interface. At a frame rate of 30 Hz, and a resolution of 1mm, the manipulator is required to travel at 3 cm/s with a maximum allowable error of 0.5mm/s for a scan time of 2.5s. Uncertainties in the video processing rates can lead to larger errors in the position estimation. This can be solved in three ways outlined in Table 3- 5.

Table 3- 5 : Timing calibration methods

Method	**Description**	**Challenges**
NGA-manipulator coupling	Manipulator driven by ISR provided by the NGA system, reducing problem to position based control scheme	System slowing down and interfacing challenges due to communication link between NGA and manipulator
Off-line NGA timing	Measure the true processing rate of the NGA off-line and then apply the manipulator speed to this frame rate to obtain position	Probably the simplest solution but cannot account for variations of time during the scan process if any
On-line NGA timing	Measures the time between individual frames during scan and applies the manipulator speed to this time to obtain position	Will account for variations in time during the scan process, but will add processing time to the scan

Both Off-line and On-line methods have been tested for suitability, and the On-line method has been implemented.

3.4. Image Extraction

The process of image extraction involves selecting the nugget mapped image from the image mapped by the NGA, selecting the crucible surface map from the image mapped by the SGA and relating the two to a common reference frame for packing.

3.4.1. Nugget Selection and Surface Selection

Nugget Selection

The process of nugget selection from the mapped image requires two primary considerations (a) differentiating the nugget from the parts of the manipulator mapped and (b) differentiating the nugget from any over hanging gripper parts[Leier]. Consideration (a) is accomplished by setting the lowest visible part of the manipulator at a predefined reference height, z', with which data comparisons can be made and nugget selection can be accomplished. The second task of nugget differentiation with respect to overhanging suction cups can be more involved. The deformable shape of the cups excludes feature extraction which are also computationally intensive for 3-D imaging. The assumption that the gripper will always be obscured in the field of view of the NGA is not a valid generalization, but true for a large fraction of the packable nuggets that have dimensions greater than that of the gripper (see Appendix H for nugget size distribution). Differentiating the non-nugget features based on reflection intensity properties can be misleading as the cups can get coated with a silicon dust layer. Color mapping and differentiating proves to be the most viable but expensive solution.

Crucible surface selection

The process of crucible surface selection is done by initializing the system before individual nugget fill commences, but after the bed layer has been placed. This maps the crucible as a ring, with the aid of stand off markers on the crucible positioning frame, that mounts the crucible vertically (to within system resolution) with respect to the SGA detector. This reference ring is then used during the system level packing process to differentiate the surface used for packing with its environment.

3.4.2. Coordinate Frames

The entire RACS packing process is based on three coordinate frames (a) the NGA coordinate frame, (b) the SGA coordinate frame and (c) the manipulator coordinate frame. In order to successfully operate this system these three coordinate frames (and images) must be related to a common reference frame, chosen as the manipulator coordinate frame. In order to perform this "calibration", two essential steps are necessary:

NGA to Manipulator Reference Frame

Given the NGA and the manipulator coordinate frames, in order to remove any rotational transformations between the two coordinate frames, a dial indicator (with a resolution of 0.0005" or 0.013 mm) is mounted on the end effector. Under the assumption of rigid member kinematics for the manipulator, the dial indicator is positioned on the base plane of the NGA system and measurements are made in the three orthogonal axes of the manipulator. With the help of a screw-type adjustment system, small changes can be made to the position of the NGA on the upright mounting posts, till no deflections are seen on the dial indicator in the three coordinates. This is limited by

(a) inaccuracies and deflections in the manipulator, (b) machining and surface errors in the mounting of the NGA back plane and (c) resolution of adjustment mechanism. This helps rotationally align the NGA and manipulator coordinate frames to sub-millimeter accuracy based on the above limitations. Further rotational misalignment can be ignored as negligible. For translational calibration a single known point on the manipulator end effector is mapped by the NGA. If this point is at a vector $\mathbf{x_{robot}}$ in the manipulator frame and is at $\mathbf{x_{camera}}$ in the NGA frame then the NGA frame can be located with respect to the manipulator frame by vector triangulation given by $\mathbf{x_{camera}}$ - $\mathbf{x_{robot}}$. The transformation matrix simplifies to:

$$\begin{bmatrix} [R_{xyz}] & T_{xyz} \\ \vec{0} & 1 \end{bmatrix} = \begin{bmatrix} 1 & 0 & 0 & x_{camera} - x_{robot} \\ 0 & 1 & 0 & y_{camera} - y_{robot} \\ 0 & 0 & 1 & z_{camera} - z_{robot} \\ 0 & 0 & 0 & 1 \end{bmatrix} \qquad (3\text{-}17)$$

SGA to Manipulator Reference Frame

Given the SGA and the manipulator coordinate frames, the approach is again to simplify the problem from that of six unknowns (three position (T_X , T_Y , T_Z) and three rotational (α, β, γ)) to that of three unknowns in position only. For the SGA coordinate frame in some arbitrary position and orientation with respect to the manipulator coordinate frame, the general transformation matrix between the two coordinate frames given by:

$$\begin{bmatrix} [R_{xyz}] & T_{xyz} \\ \vec{0} & 1 \end{bmatrix} = \begin{bmatrix} \cos\beta\cos\alpha & -\sin\gamma\sin\beta\cos\alpha - \cos\gamma\sin\alpha & \sin\gamma\sin\alpha - \cos\gamma\sin\beta\cos\alpha & T_x \\ \cos\beta\sin\alpha & \cos\gamma\cos\alpha - \sin\gamma\sin\beta\sin\alpha & -\sin\gamma\cos\alpha - \cos\gamma\sin\beta\sin\alpha & T_y \\ \sin\beta & \sin\gamma\cos\beta & \cos\gamma\cos\beta & T_z \\ 0 & 0 & 0 & 1 \end{bmatrix}$$

In order to solve for these six variables, the system needs to plot two given positions of a point on the manipulator. If these points are known in the two coordinate frames then by applying:

$$\begin{bmatrix} x_{camera} \\ y_{camera} \\ z_{camera} \\ 1 \end{bmatrix} = \begin{bmatrix} [R_{xyz}] & T_{xyz} \\ \vec{0} & 1 \end{bmatrix} \cdot \begin{bmatrix} x_{robot} \\ y_{robot} \\ z_{robot} \\ 1 \end{bmatrix} \qquad \textbf{(3- 18)}$$

to the two sets of point coordinates, the six unknowns can be solved. Although possible, in practice solving transcendental equations are not generally simple and require numerical methods. To simplify the problem as in the case of the NGA, the SGA flange mounting is modified to fit a three rotational degree of freedom adjustment mechanism, consisting of a rotab and a two axis gimbal plate, that then allows for roll, pitch and yaw. Mapping three points, indicated by the manipulator that form a plane parallel to the ground plane, in the camera frame can be used as indicators to adjust the gimbal-rotab mounting to eliminate three (rotational) of the six unknowns. The problem simplifies as before to that of two position vectors given by vector $\mathbf{x}_{\mathbf{robot}}$ in the manipulator frame and is at $\mathbf{x}_{\mathbf{camera}}$ in the SGA frame. Once again vector triangulation given by $\mathbf{x}_{\mathbf{camera}} - \mathbf{x}_{\mathbf{robot}}$ solves for the position of the SGA coordinate frame with respect to the manipulator frame to give (3- 17.

3.5. Results

3.5.1. NGA Results:

For the NGA proof of concept two sets of data are shown. The first (Figure 3- 9, and Figure 3- 10) indicate the results obtained by scanning a single line across the step profile of the Delrin calibration object (see Appendix G). Comparing the mapped step results with those of the original object (shown from the side perspective only), qualitatively a series of the seven distinct steps (plus noisy points) can be seen in Figure 3- 10, with average correlation within submillimeter accuracy to those shown in Figure 3- 9 and Appendix G. The average error seen is 0.34mm with a σ of 0.12mm. Random error points seen are possibly reflective artifacts due to surface machining and system errors. The second (Figure 3- 11, Figure 3- 12 and Figure 3- 13) indicate the results obtained by scanning an entire nugget and comparing a single representative slice of the mapped nugget with that measured by a CMM (Coordinate Measuring Machine). The average error seen is 0.4mm with a σ of 0.2mm. The maximum error seen here is approximately 1mm, which could be partly an artifact of mismatching of the reference data on the mapped profile.

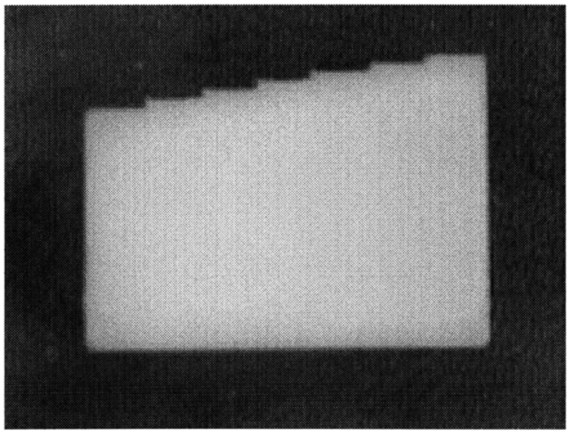

Figure 3- 9 : Calibration object image

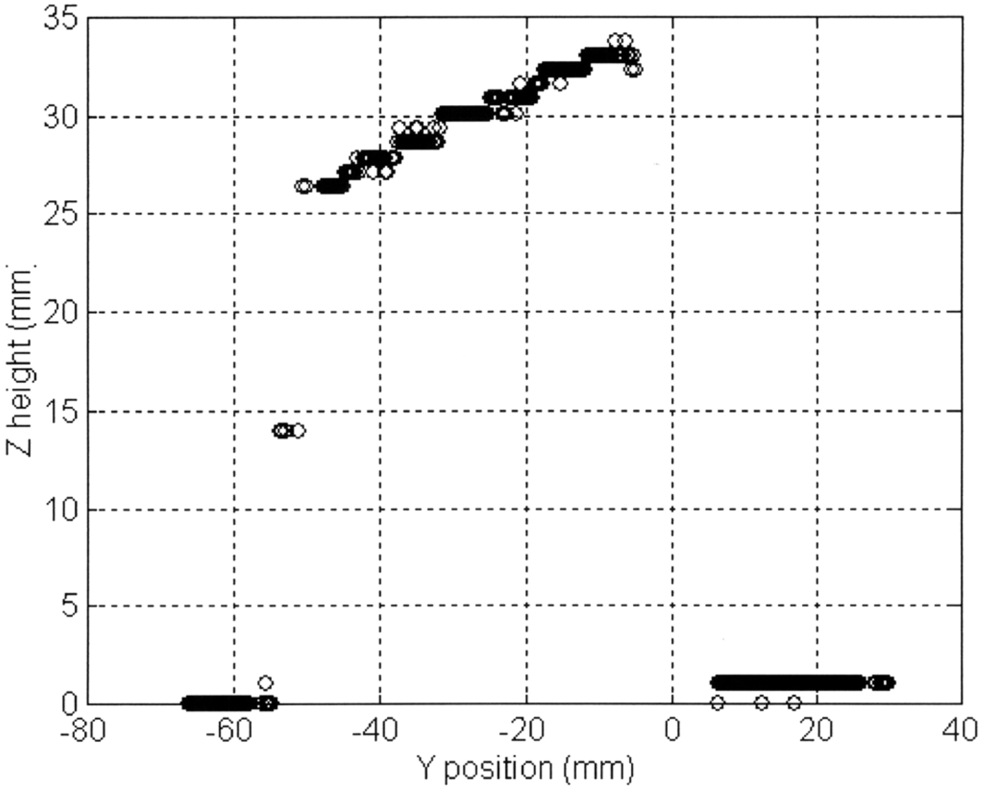

Figure 3- 10 : NGA calibration object section map

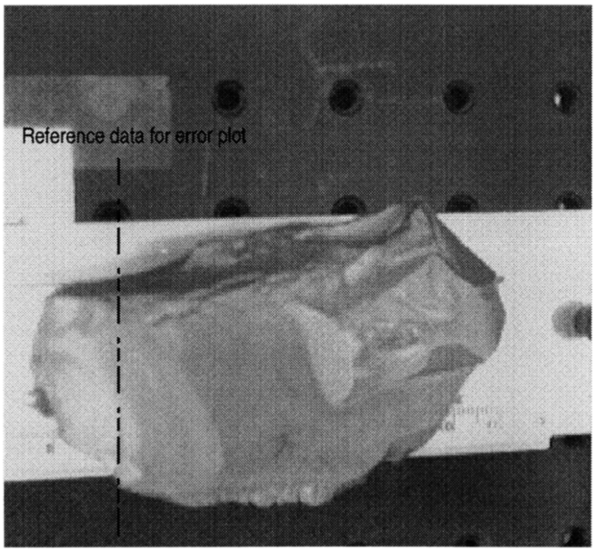

Figure 3- 11 : Nugget image

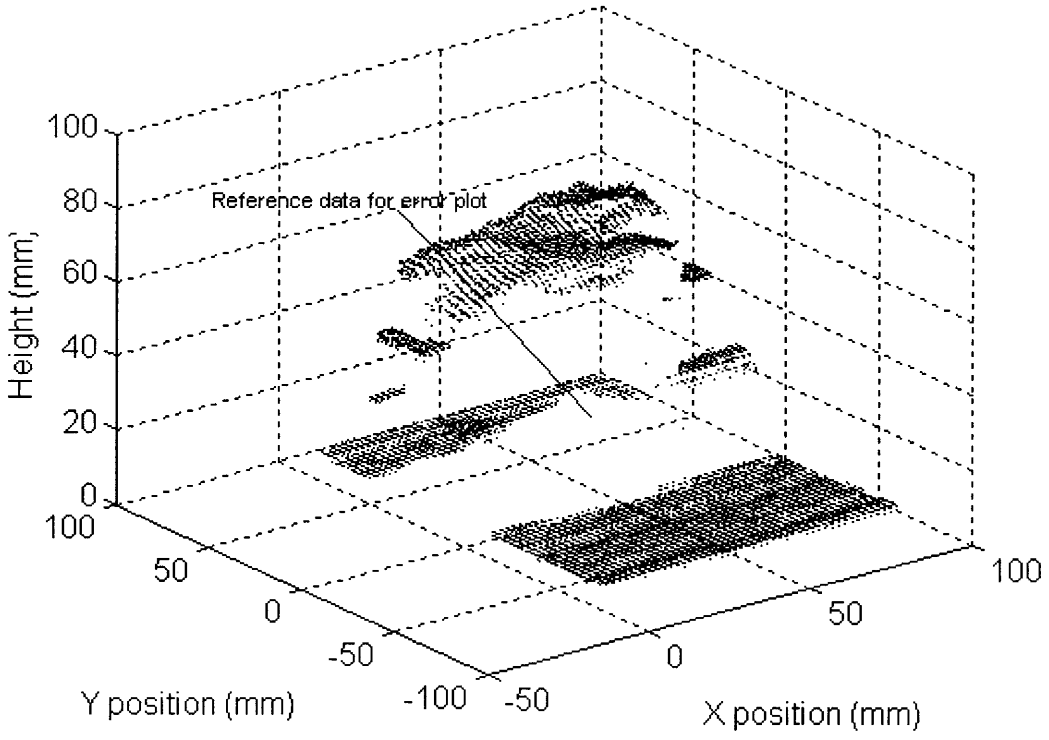

Figure 3- 12 : NGA nugget mapped profile

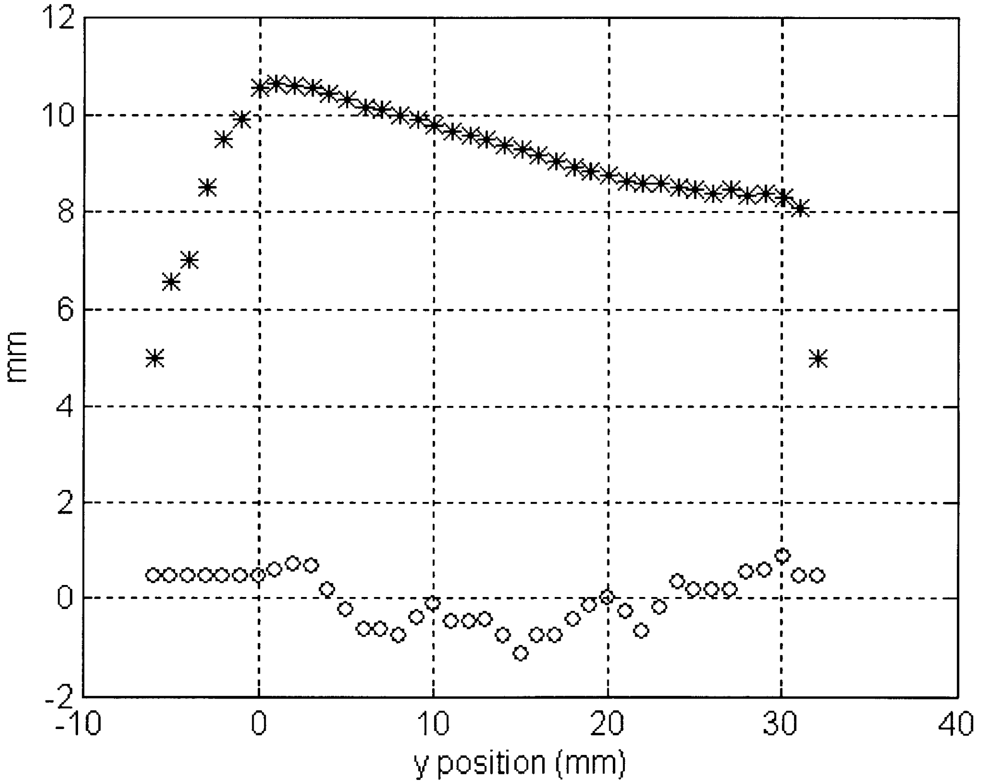

Figure 3- 13 : Reference data profile and error plot

3.5.2. SGA results

For the SGA, profile quantitative comparison for error is more difficult and inaccurate to perform. Once again two sets of sampled data sets are shown. The first (Figure 3- 14 and Figure 3- 15) indicate a nugget field mapped.

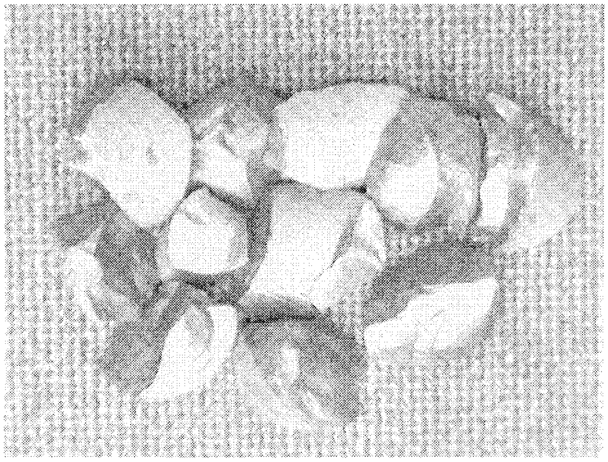

Figure 3- 14 : Nugget field image

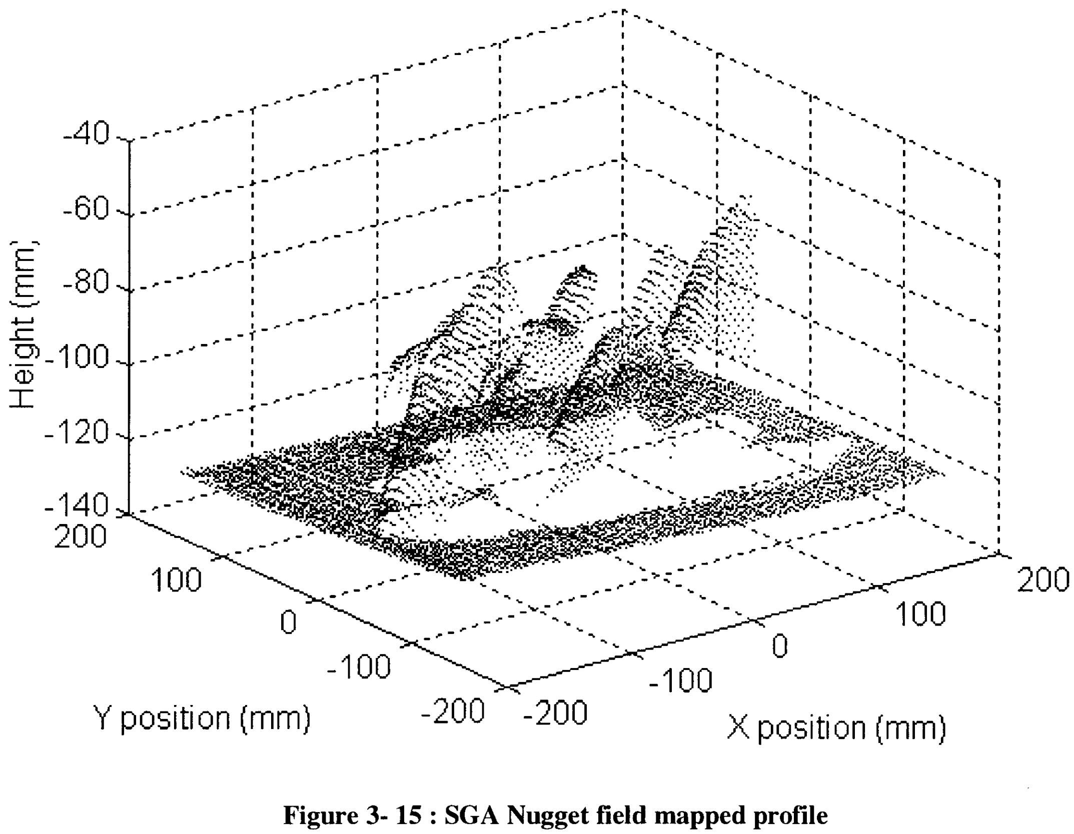

Figure 3- 15 : SGA Nugget field mapped profile

The second (Figure 3- 16, Figure 3- 17 and Figure 3- 18) indicates a laboratory test-bed of a Mars platform consisting of 20 mapped images (each approximately 1' x 1' of physical space, each mapped by 100x500 points with X Y resolution of 3.04mm and 0.61mm respectively) put together for a macroscopic comparison. Further use of this data was made by [Farritor] for purposes of a simulation study.

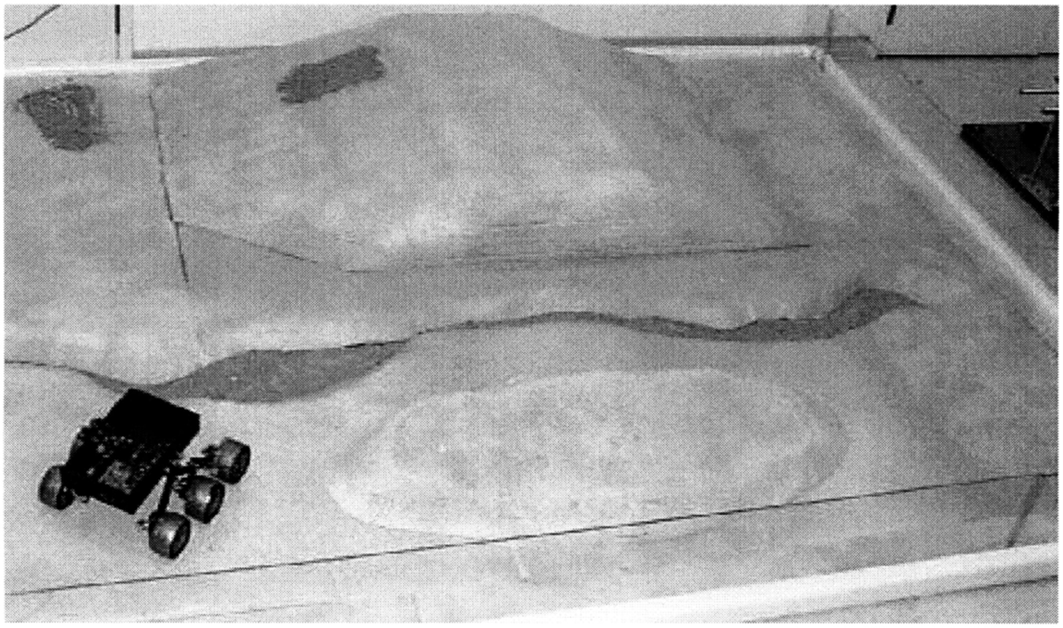

Figure 3- 16 : Original Mars laboratory test-bed [Farritor]

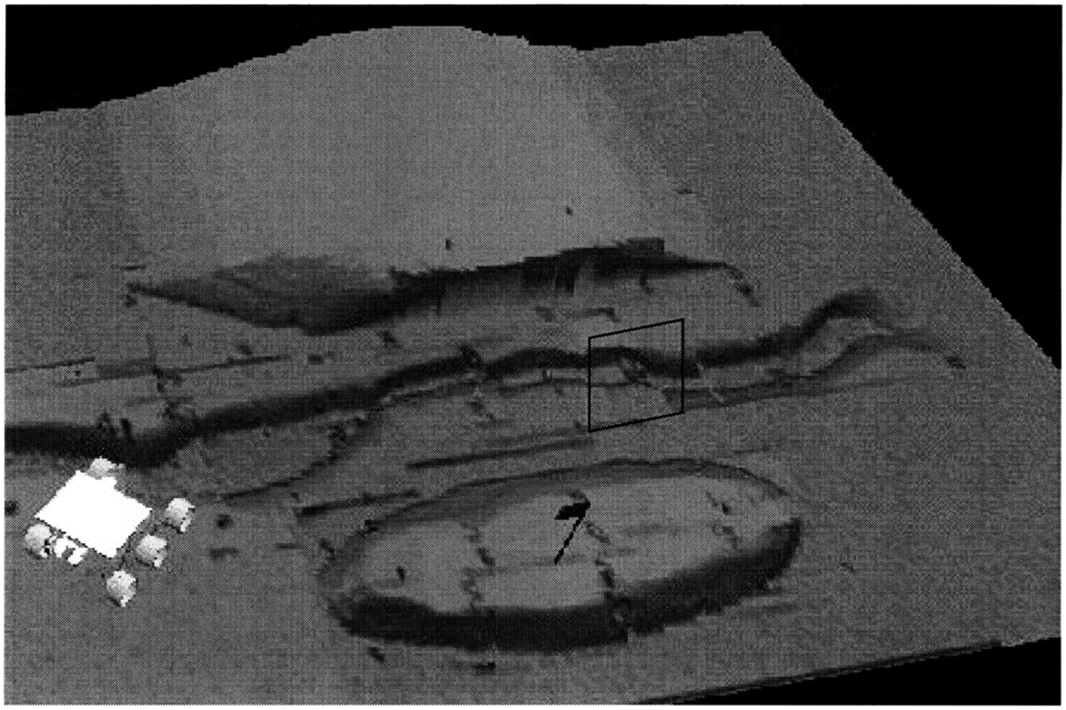

Figure 3- 17 : SGA mapped profile of Figure 3- 16, using 20 mapped profiles of 1'x1' physical dimensions, each with 500x100 points [Farritor]

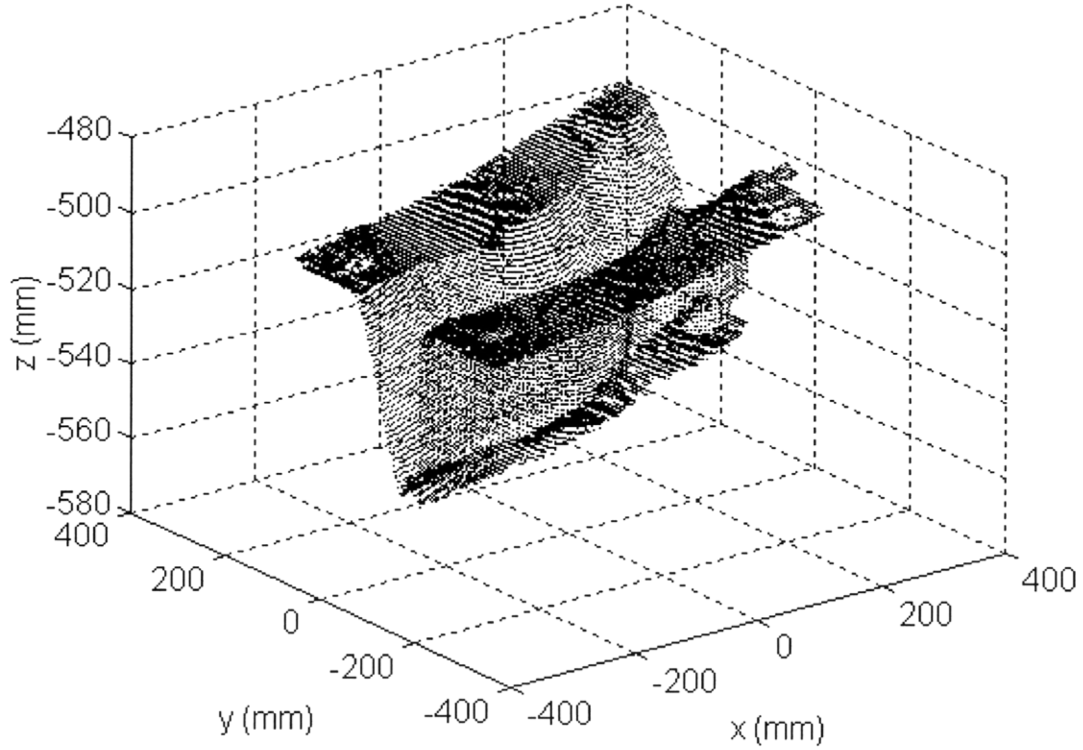

Figure 3- 18 : Section marked in Figure 3- 17 blown up

Chapter 4. Virtual Trial and Error Approximate Packing

4.1. Introduction

As described in section 1.4, a significant amount of research has been done in the area of bin packing. Such algorithms can be divided into either off-line processing or on-line processing. In the first case, the objects to be packed and the bin(s) are all presented together and the packing algorithm is applied to all objects simultaneously to find an "optimum" packing structure. In the second case, each packing object is presented individually to the packing algorithm, without allowing for rearrangement or shifting of previously packed objects. Acceptable placement is achieved on a case-by-case basis. Further, off-line and on-line bin packing research address one, two or three-dimensional problems for structured objects such as rectangles and parallelepipeds, or for unstructured objects with more complex shapes.

The bin packing problem is a classical combinatorial optimization problem that belong to the class of NP-hard problems, and therefore the processing time that is required to find an optimal solution is most likely exponential with the number of packing items. Algorithmic strategies like dynamic programming, branch and bound, and heuristic search techniques which can produce the optimal solutions to these problems are at best pseudo-exhaustive in nature and are often unusable in practice. But approximation algorithms, such as First-fit decreasing and Harmonic packing, with well-studied average-case and worst-case behavior studies, can produce acceptable solutions in reasonable time. Several problem-specific approximation algorithms are available to solve these problems, but the results obtained by them are not found to be satisfactory and seldom can be applied with success elsewhere under modified constraints. There is no general technique known which can bridge the gap between a near-optimal solution and the optimal solution by systematically improving the cost of the solution provided by an approximation algorithm [Sarkar *et. al.*].

For the RACS, nugget placement planning is crucial as it directly determines the charging (packing) density and affects the process cycle time. Since each nugget is dealt with sequentially, an on-line bin-packing algorithm is required. Several solutions to the offline and online problem with significant analysis on the upper and lower bound performances have been proposed in the literature. However, as mentioned above, most of the solutions are problem-specific and are limited by constraints such as object structure and size, dimensionality, and amount of knowledge of object structure and size.

Dimensionality can be described as follows. In one dimensional bin packing, given a finite set of X objects, with associated normalized sizes, it is desired to partition the X objects into k disjoint subsets, such that the sum of the sizes of the objects in each partition is less than unity and k is minimized. Two dimensional bin packing is defined as packing a finite number of 2-D objects with associated sizes, into a 2-D bin of given length and infinite height, to be minimized when packed. Three dimensional bin packing is an extension of the above into a given third dimensional width, with the same objective of minimizing the packed height. Object structure and size correspond to the shape of the object and its structural dimensions. Very few people have approached the problem of irregular shaped object packing [Whelan and Batchelor]. Further, the amount of the knowledge possessed by the processor of the object structure and its structural dimensions can be critical in determining an acceptable packing algorithm.

Based on the design of the RACS, the geometric structure of the individual nuggets and the processing time constraints, an efficient, on-line, 3-D bin-packing algorithm for irregularly shaped objects is developed given only the exposed surface geometries of the object (nugget) and bin (crucible). The strategy utilizes only the raw range image data provided by the 3-D vision system (from Chapters 2 and 3), does not require feature extraction of range images (model free) and performs all computations in a virtual environment simulated by the acquired data in the manipulator coordinate frame. The result is a computationally simple and effective solution to the nugget placement problem that can be extended to solve a n-dimensional packing problem.

This chapter explores the Virtual Trial and Error Approximate Packing algorithm (VTEAP) in greater detail. Section 4.2 describes the requirements/goals of such an algorithm. Section 4.3 outlines the approach to solve the packing problem and presents the two dimensional perspective, with simulated results and a direct comparison metric with other online packing strategies. Section 4.4 extends the two dimensional version of the VTEAP into the third dimension and provides simulated results of the algorithm.

4.2. Performance Goals

As previously mentioned, the packing algorithm requires to produce a methodology for manipulating and placing each individual nugget obtained by the gripper [Leier], into a rigid, fragile environment created by the crucible at a packing rate and charge competitive with that of humans. Based on this, the system requirements have been defined and are outlined in Table 4- 1.

Given the triangulated data provided by the vision systems, the packing algorithm, must transfer these into a common reference frame defined by the crucible

(Chapter 3), and then mesh the data sets together till an acceptable location is found. The system provides a solution that is computed internally by the computer, and transfers the data via a series of protocols to the manipulator control station in the manipulator coordinates (Chapter 5). In the factory system, these protocols will not be required, as the four major system components (Table 1-2) are operated by a common workstation.

Table 4- 1 : System Requirements

1. Search space data resolution	1mm
2. Processing Rate for Nugget Placement	1 s Also defined by O(n)
3. Search space size	One nugget ring around crucible wall, with a 30 degree nugget manipulation cone for each test zone
4. Data provided	On-line : One nugget at a time Image : Camera/laser exposed triangulated profile only
5. Nugget rejection	Minimize nugget rejection

4.3. Bin Packing

Various methods have been studied for on-line multidimensional packing for irregular shaped objects. Based on the extreme open-endedness of this problem, very few generalized solutions exist. It is the objective of this section to define, explore and understand fitting procedures based on cost functions defined with combinations of best fit, first fit, lowest fit and modified contact fit. In the literature more exotic processes such as model based fitting and simulated annealing [Georgis et. al.] have been proposed. (In simulated annealing the physical process of annealing which involves raising the temperature of a solid to the melt temperature and the careful decreasing of the temperature until the particles arrange themselves in the ground state of the solid, thus minimizing the system energy is simulated. It has been suggested that good results to combinatorial optimization problems can be achieved by simulating the process of annealing. A solution corresponds to a state of the physical system with the energy defining the cost function. Optimality is defined as the ground state.) These processes are computationally intensive and do not work well for the RACS system requirements. Hence a novel packing algorithm has been constructed and described in the following.

4.3.1. General Algorithm

The main algorithm computational steps are described in Table 4- 2.

Table 4- 2 : Virtual Trial and Error Algorithm Design

COMPUTATION STEP	DESCRIPTION
1. Data Extraction	▪ SGA and NGA provide data appearing as a 2-D matrix of points ▪ Matrix defined by object's largest dimensions ▪ the region of interest defined(Figure 4- 1(a)). ▪ Compensation by algorithm if zero values obtained in image matrix (corresponding to non-existent areas)
2. Nugget Approach	▪ Data for both surfaces are in the same coordinate frame ▪ 2-D matrix of heights are manipulated in the z direction till single point contact is obtained (Figure 4- 1 (b))
3. Stability Search	▪ Body coordinate transformation of the virtual nugget till three point contact is achieved. ▪ center of mass calculations for stability are approximate due to knowledge of only the visible half of the nugget ▪ Search space for placement is a one-nugget annulus around crucible wall.
4. Excess Volume Minimization	▪ Integration of excess height differences over projected contact area for every stable position found.
5. Cost Function	▪ Cost function is formulated to determine packing structure ▪ Accounting for vertical placement position of nugget w.r.t. to the ground profile, the number of points in contact between the surfaces, excess volume and distribution of contact points against crucible.
6. Crown Building	▪ Positional delimiters describe a virtual crown surface preventing nugget excursions ▪ limits to bridge formations (where nuggets form a statically stable bridge across the crucible if packed tightly enough) by forcing a lower charge density with increasing height at the crown levels. Further, for the 36" crucible, dynamic analysis show that it is unlikely that bridging could occur.
7. Center Fill Vs Wall Pack	▪ Cost function prevents the buildup of excessively high walls by limiting the fill function ▪ Cost function can be modified to adapt to packing strategies involving placing larger nuggets in the fill areas

The above description applies for each nugget scanned which is then to be placed within the crucible. Computational speeds have been satisfactorily demonstrated to be within 1 second per nugget as the search path is small and limited to a one-nugget annulus of wall. Additionally due to the computational simplicity of the algorithm, changes to the packing style can be made by appropriate changes in the cost function without taxing the processing speed of the system in a significant way. Further, object shape and geometry are not influencing factors in the performance of the algorithm which is clearly O(n) (based on n nuggets to be packed) as each nugget takes O(c) time where c is a constant. A closer bound on the nugget placement time is determined by the search space, the dimensionality of the problem and the specific cost function used. Figure 4- 2 demonstrates the sequence of approach to a stable configuration in a two dimensional version of the problem with a virtual nugget and a virtual crucible ground profile. Only the lower half of the nugget is used based on the data obtained from the NGA system.

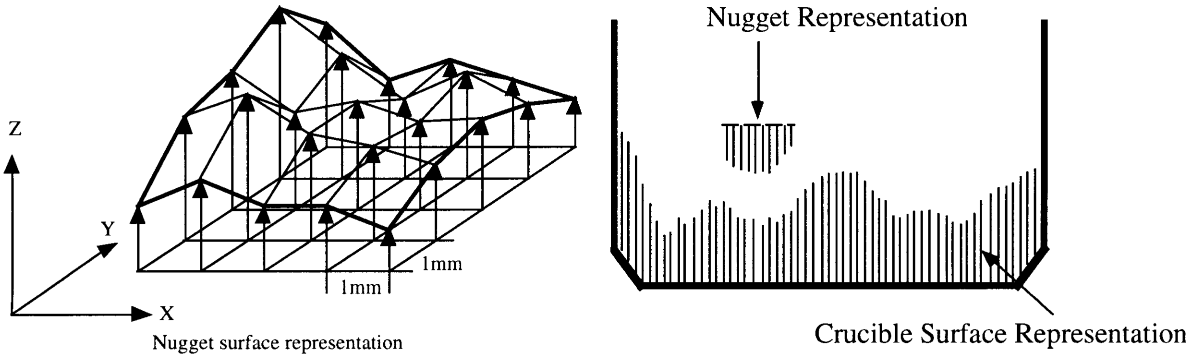

Nugget surface and data Extraction

(a)

Nugget approach to crucible surface for one point contact

(b)

Figure 4- 1

4.3.2. Cost functions

In order to better understand the choice of cost function involved in the packing procedure the following base definitions are now introduced :

Table 4- 3 : Cost function base definitions

Lowest fit	Packing of object to the lowest position possible
Minimum Volume/Area fit	Packing of object to the location minimizing the excess volume/area left under the placed object
First fit	Packing of object to the first location providing an excess volume/area less than a predefined value
Contact fit	Packing of object to location providing the most number of environment to object contact points

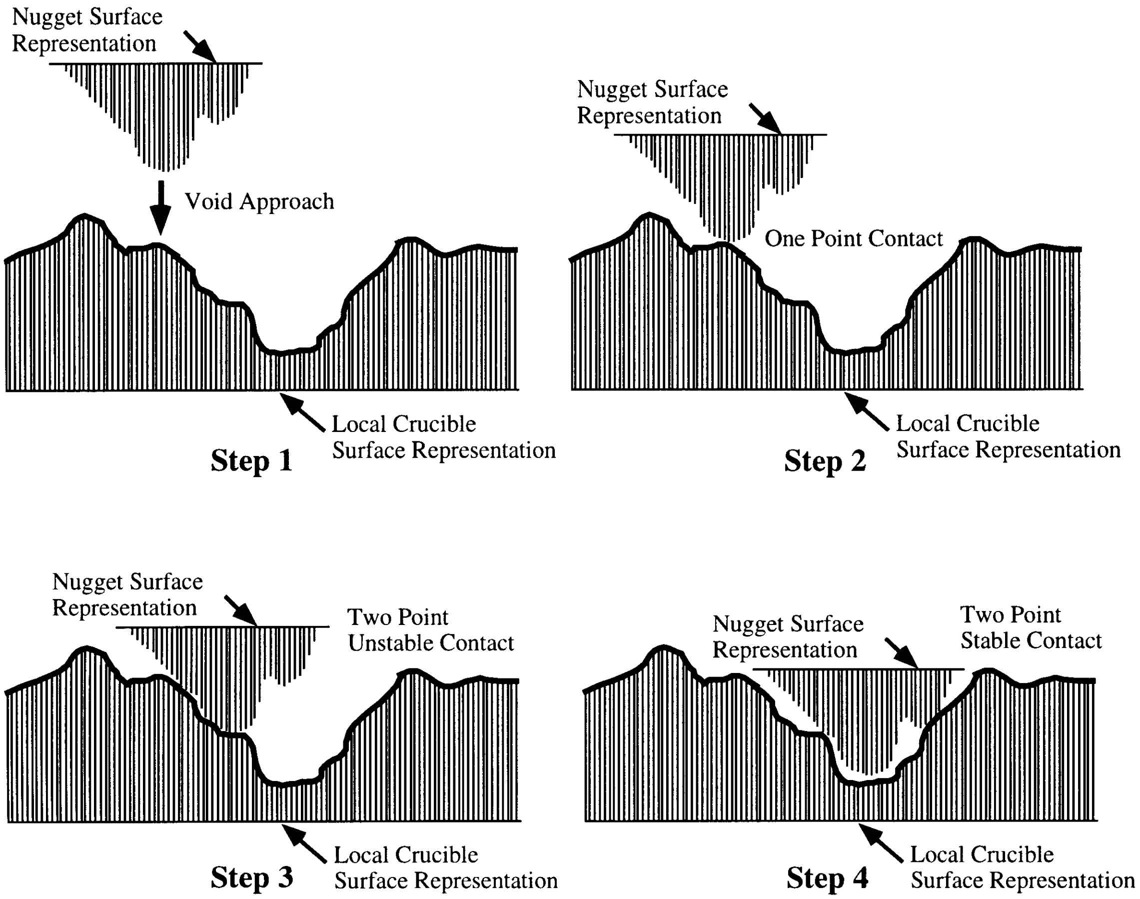

Figure 4- 2 : Stable configuration approach

To be able to determine the suitability of a cost function, a series of simulated tests have been performed using the base definitions and combinations of the base definitions. The performance index is a modified version of the packing density. A weighting factor, known as the count ratio, is applied. The count ratio is defined as the ratio of the total number of objects packed to the number of objects presented to the scene. The performance index is defined as the stability parameter (defined in section 4.3.4) divided by the product of the packing density and the count ratio. Nuggets rejected are currently assumed to be placed into the bulk center of the fill. From Table 4- 3, the following cost functions were generated and tested for suitability in 2-D:

- ☐ Lowest fit
- ☐ Lowest fit with area (volume) minimization

- ☐ First fit
- ☐ First fit with lowest fit
- ☐ Area(volume) minimization with stability limiting parameter dh
- ☐ Area(volume) scaling with lowest and contact fit minimization

In order to form a comparison metric with other packing schemes in the literature, studies using rectangular objects for the 2-D case have been performed, and the results presented. As mentioned above, the algorithm extends between dimensions and hence it can be argued that the performance metric of a given scheme will extrapolate between dimensions as well. Hence, exhaustive studies have only been carried out in the 2-D case, limited primarily by processing time in order to establish clear simulated behaviors.

4.3.3. Working Parameters

The algorithm has several working system parameters outlined in the following.

- Stability limiting parameter dh - defined as the maximum height above the lowest sector on the current crucible ground profile to which the current nugget can be placed. Sector size is defined based on the dimensions of the smallest packable nugget. The lowest sector is defined by the lowest part of the ground profile that can accommodate the smallest packable nugget. By controlling dh intelligently, one can prevent the growth of columnar packing in which unstable and undesirable nugget placement is obtained. dh=1 is considered as the packing resolution (simulated as 2mm). Packable nugget characteristic sizes range from 19mm to 76mm.
- Contact points - are the intersecting points between the nugget profile and the surface profile that determine physical contact of the object with its environment. Two-point contact in 2-D and three-point contact in 3-D is desirable for a static stability. Defining a statically stable configuration can be difficult as neither the entire

geometry nor the location of the center of mass of the nugget is known. The total number of contact points for a given configuration is used to weigh the cost function.

- Manipulation degrees of freedom - are the rotational degrees of freedom in determining the nugget placement. The end effector is defined by a 3 d.o.f. wrist [Leier; Calzaretta], and can completely locate a given nugget within a specified solid cone (of a 30 degree solid angle). The effects of this additional nugget placement parameter has also been simulated and studied in both two and three dimensions.
- Search space - In the RACS individual nugget packing is carried out only as a nugget annulus in the crucible. In the 2-D simulation, this is represented as a planar projection. The search space is hence limited and can be further constrained by performing a coarse search with fine refinement in the zone of preference.

4.3.4. 2-D Bin Packing Results

The results can be divided into two general sections: (a) simulated random selection of object sizes and (b) simulated distributed selection of object sizes based on the known sample distribution set provided by SEH (see Appendix H). The results of (a) are presented below. The results of (b) prove to give approximately 1% improvement in all the cases shown. Nugget shapes are approximated by non-convex random polygons.

Random Object Size Selection:

☐ Lowest fit

- Approximately 3% charge improvement seen with a 2-D single d.o.f. wrist with ±15° with 5° angle step
- Average object rejection <1%
- Is typically unaffected by dh (unless dh is small which may increase object rejection)

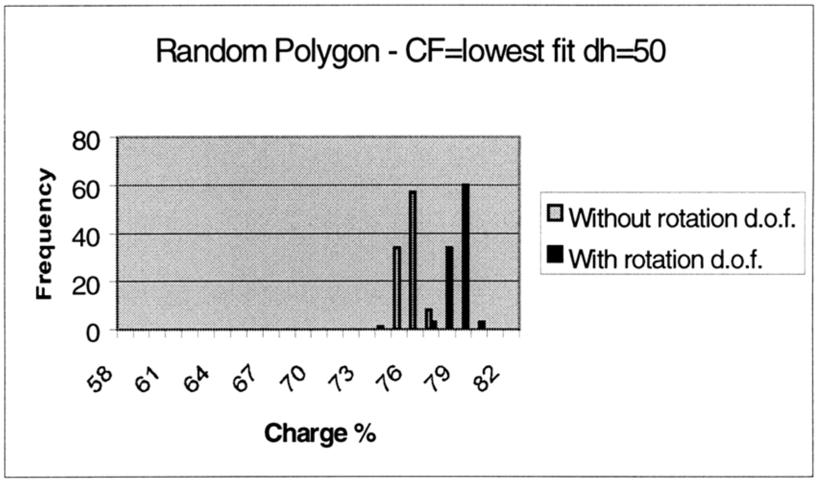

Figure 4- 3 : Polygonal lowest fit 2-D packing results

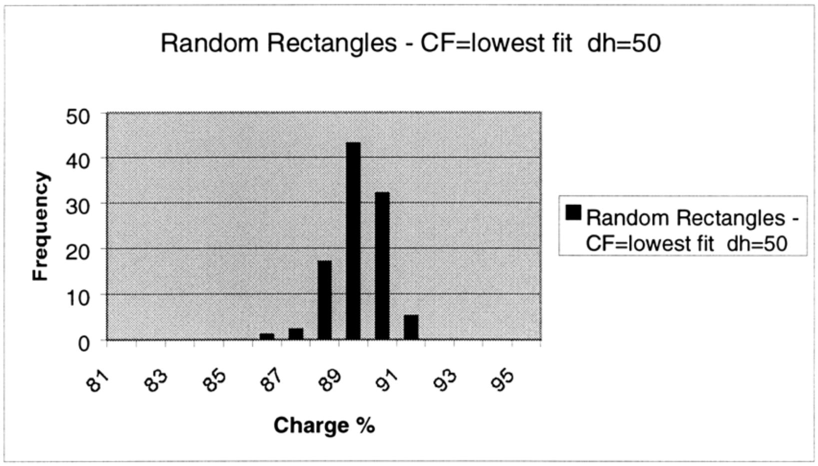

Figure 4- 4 : Rectangle lowest fit 2-D packing results

- Lowest fit with area (volume) minimization

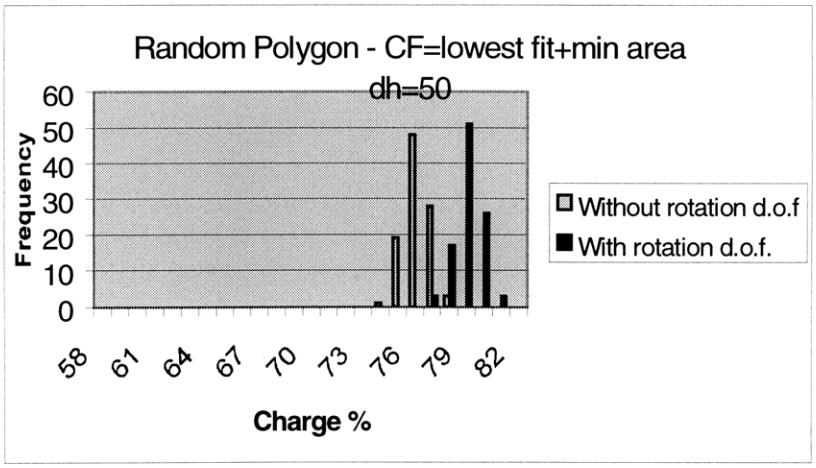

Figure 4- 5 : Polygonal lowest fit + area minimization 2-D packing results

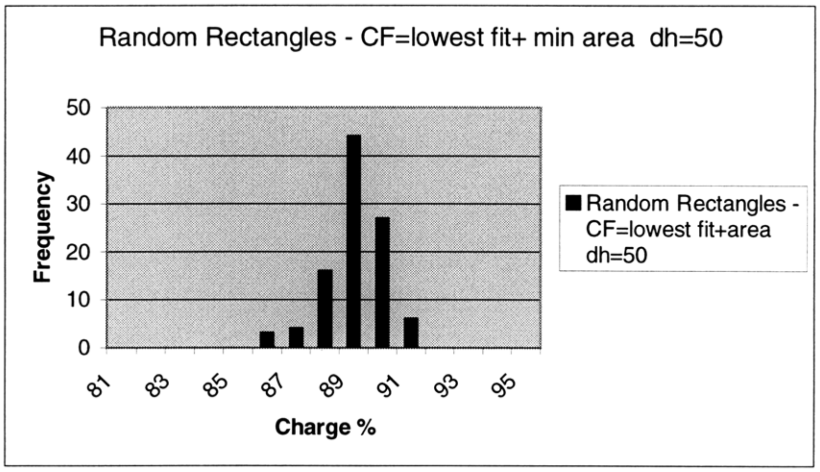

Figure 4- 6 : Rectangle lowest fit + area minimization 2-D packing results

- Similar properties as that seen in the case of lowest fit

❑ First fit

- Approximately 3% charge improvement seen with a 2-D single d.o.f. wrist with ±15° with 5° angle step
- High average object rejection percentage ≈ 22%
- Relative decline in charge density for the polygonal case which is not seen in the rectangle case

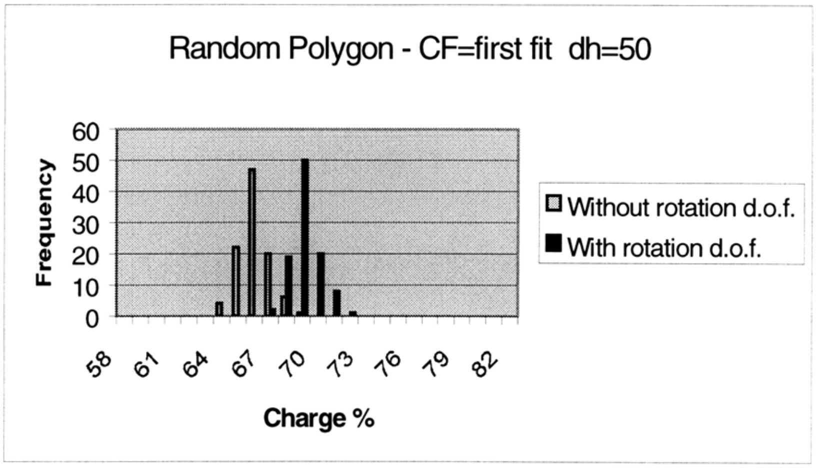

Figure 4- 7 : Polygonal first fit 2-D packing results

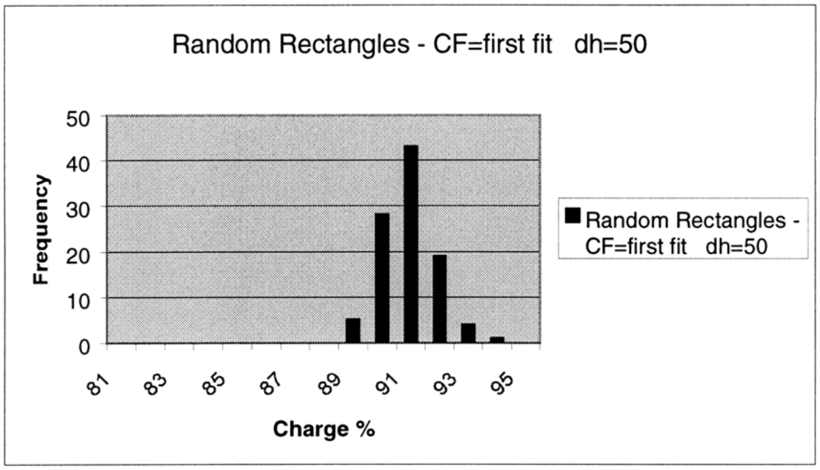

Figure 4- 8 : Polygonal and Rectangle first fit 2-D packing results

- First fit with lowest fit (descent)

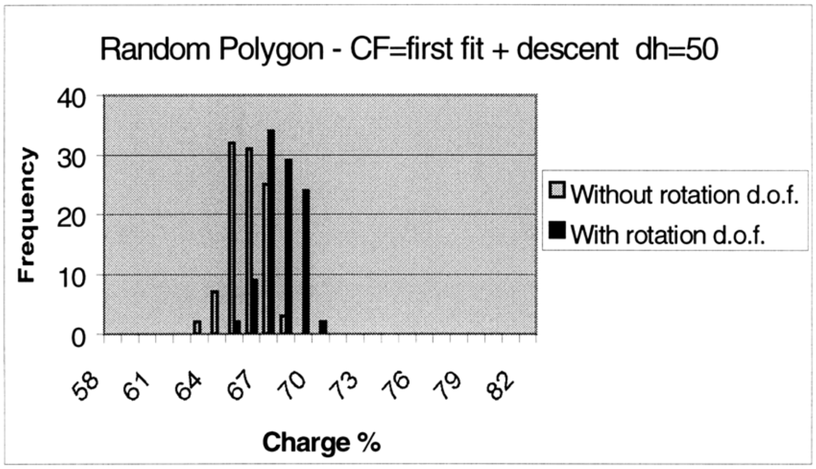

Figure 4- 9 : Polygonal first fit + descent 2-D packing results

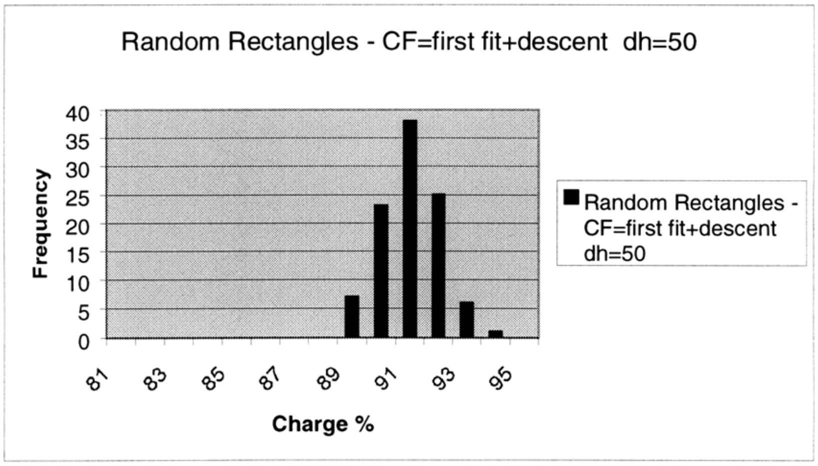

Figure 4- 10 : Rectangle first fit + descent 2-D packing results

- Similar properties as that seen in the case of lowest fit
- High average object rejection percentage ≈ 28%

- Area(volume) minimization with stability limiting parameter dh

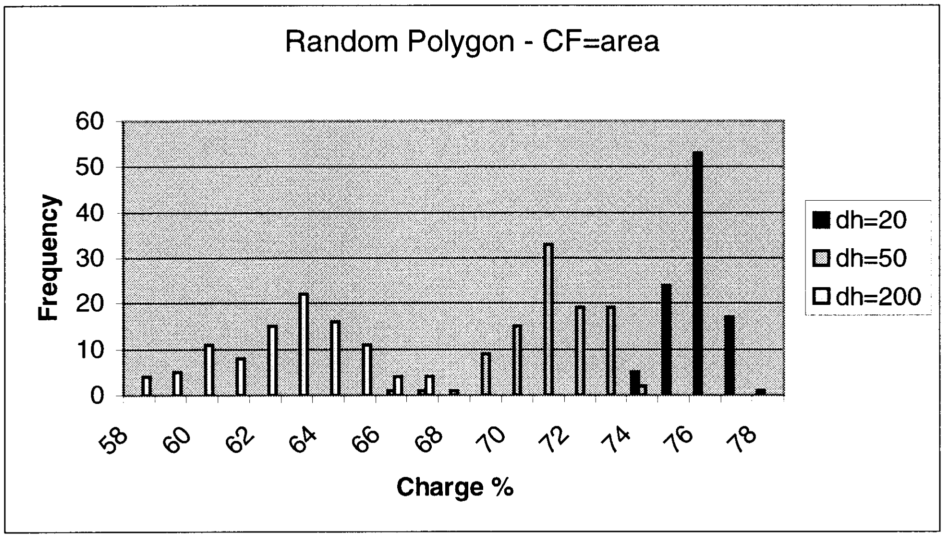

Figure 4- 11 : Polygonal area minimization 2-D packing results

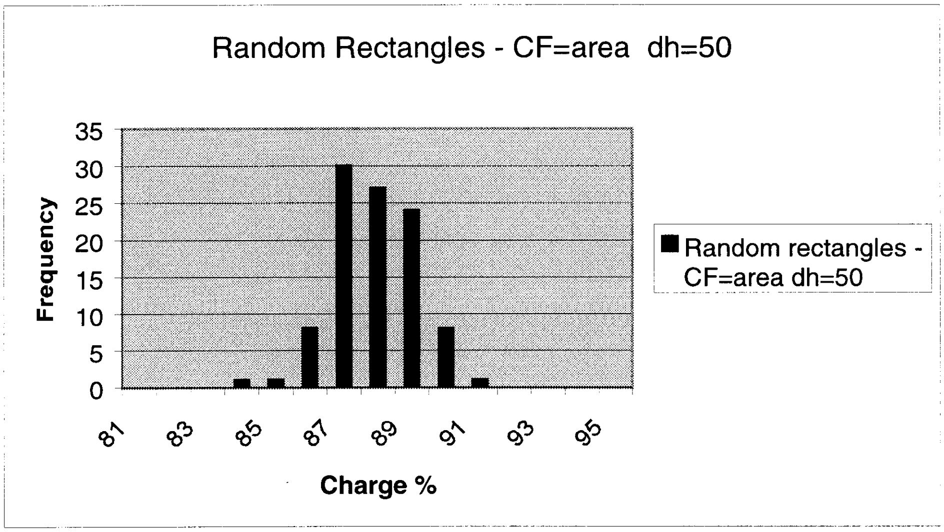

Figure 4- 12 : Rectangle area minimization 2-D packing results

- General decline in performance for both cases compared to lowest fit case
- Polygonal data shows severe decline in performance with increasing dh
- Increasing dh results in unstable columnar build up of objects

- Average object rejection percentage ≈ 12%

☐ Area(volume) scaling with lowest fit with modified contact fit minimization

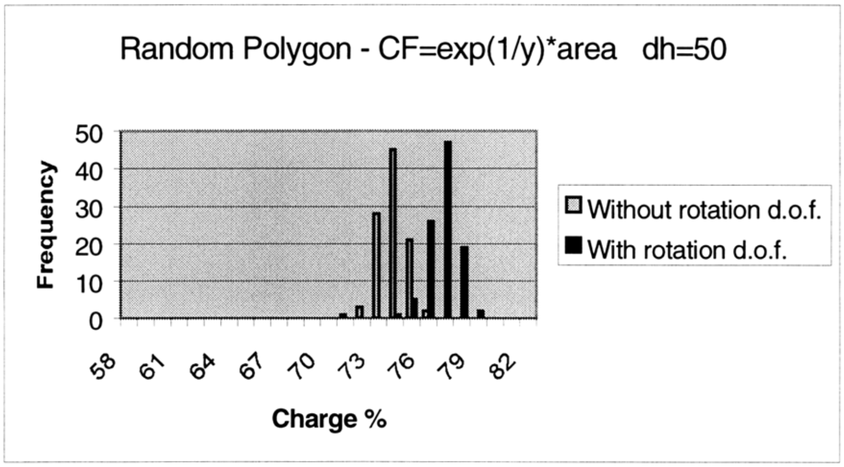

Figure 4- 13 : Polygonal area scaling and minimization 2-D packing results

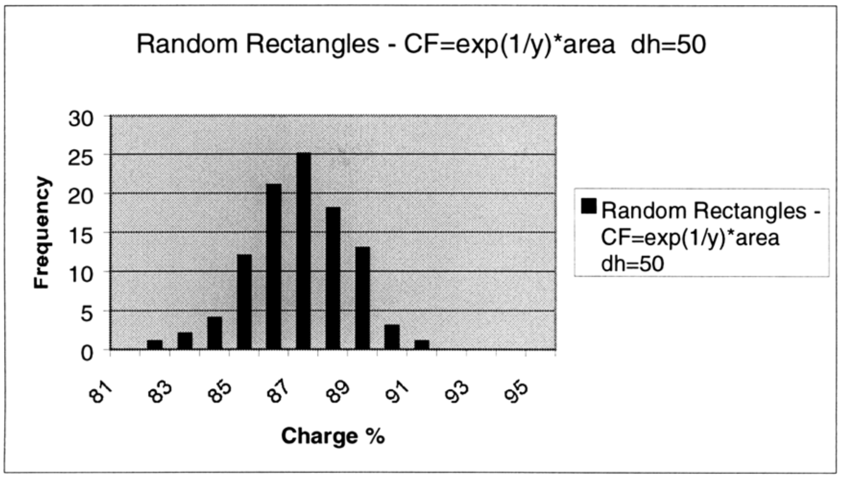

Figure 4- 14 : Rectangle area scaling and minimization 2-D packing results

- Area is scaled by an exponential of height and compensated with number of contact points
- Approximately 3% charge improvement seen with a 2-D single d.o.f. wrist with ±15° with 5° angle step
- Performance decreases with increasing dh (as in the case of unmodified area

minimization)

- Performance level of dh=50 is equivalent to that obtained with unmodified area minimization with dh=20
- Average object rejection percentage ≈ 12%

Stability

Next, the stability of each of the cases presented above is examined. Since the position of the center of mass of the each individual object is considered to be unknown, stability is a qualitative measure of how the algorithm performs at an arbitrary point in the fill process. The center of the fill bin is selected as the reference and a histogram of point distributions in distance variations around that reference is presented below in Figure 4- 15 and Figure 4- 16. From Figure 4- 15 and Figure 4- 16, it can be seen that the case of lowest fit packing philosophy proves to be the most "stable" in both the case of the polygonal object packing and rectangular object packing. Stability of the pack is measured in this case by the packing philosophy that produces the narrowest distribution around the zero mark (crucible level center) of the packing process. Note that the process of first fit and first fit with descent works well relative to the other four packing philosophies in the case of rectangular object packing when comparing both charge densities as well as stability. However, there is a severe decline in performance in both charge density and stability when applied to polygonal packing. A more quantitative performance measure is outlined in Table 4- 4 where the performance index is defined as the stability parameter divided by the product of charge density and the count ratio (where the stability parameter is the standard deviation about the reference). Based on this definition, the lower the performance index of a given packing scheme, the better the scheme is considered to perform.

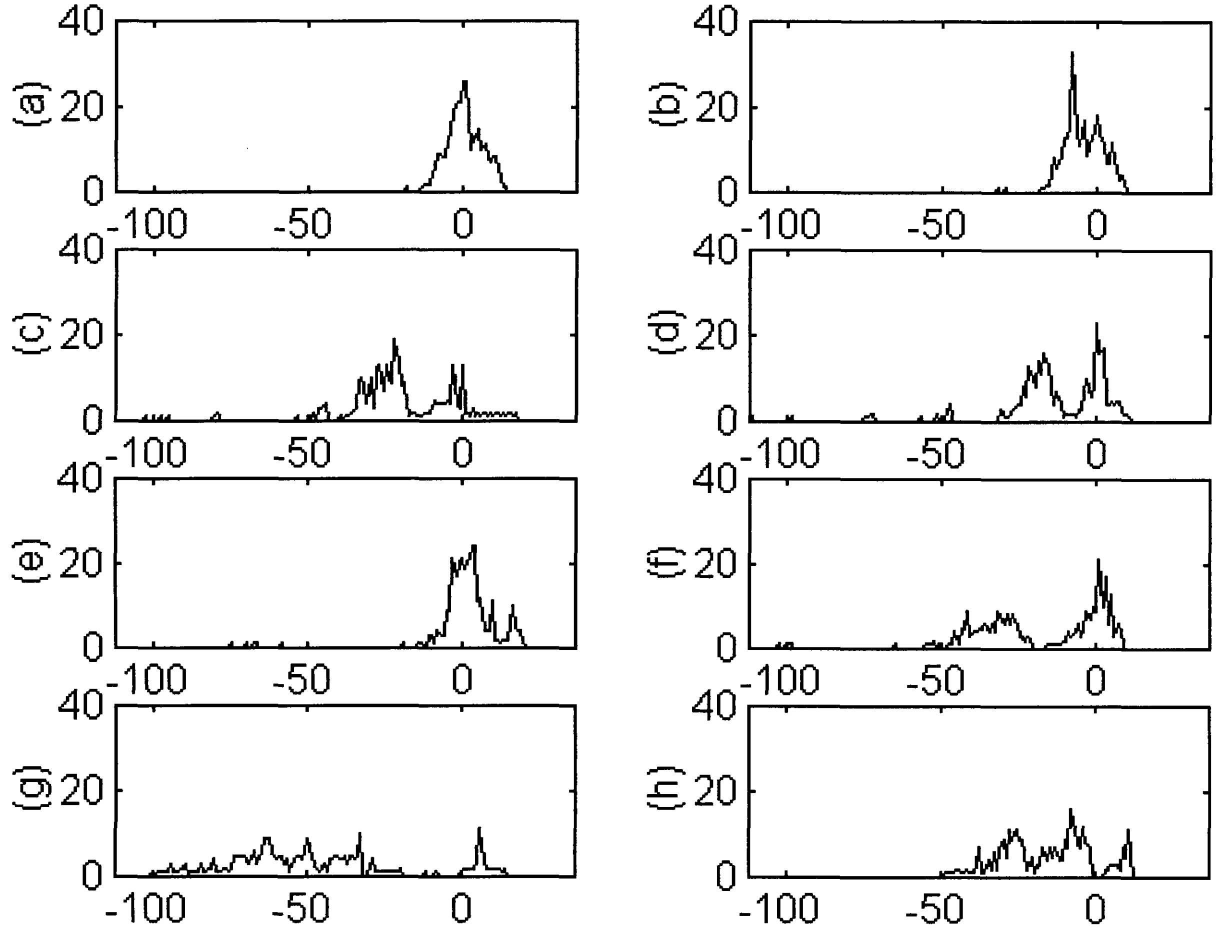

Figure 4- 15 : Plots of Number of occurrences vs height variation about 0 (given in dh units) for the case of random sized polygonal packing (a) lowest fit (σ=5.663); (b) lowest fit w/ area minimization (σ=6.4583); (c) first fit (σ=18.0159); (d) first fit w/ descent (σ=16.7); (e) minimized area fit dh=20 (σ=11.3769); (f) minimized area fit dh=50 (σ=20.8872); (g) minimized area fit dh=200 (σ=28.1290); (h) minimized scaled area fit (σ=14.6023).

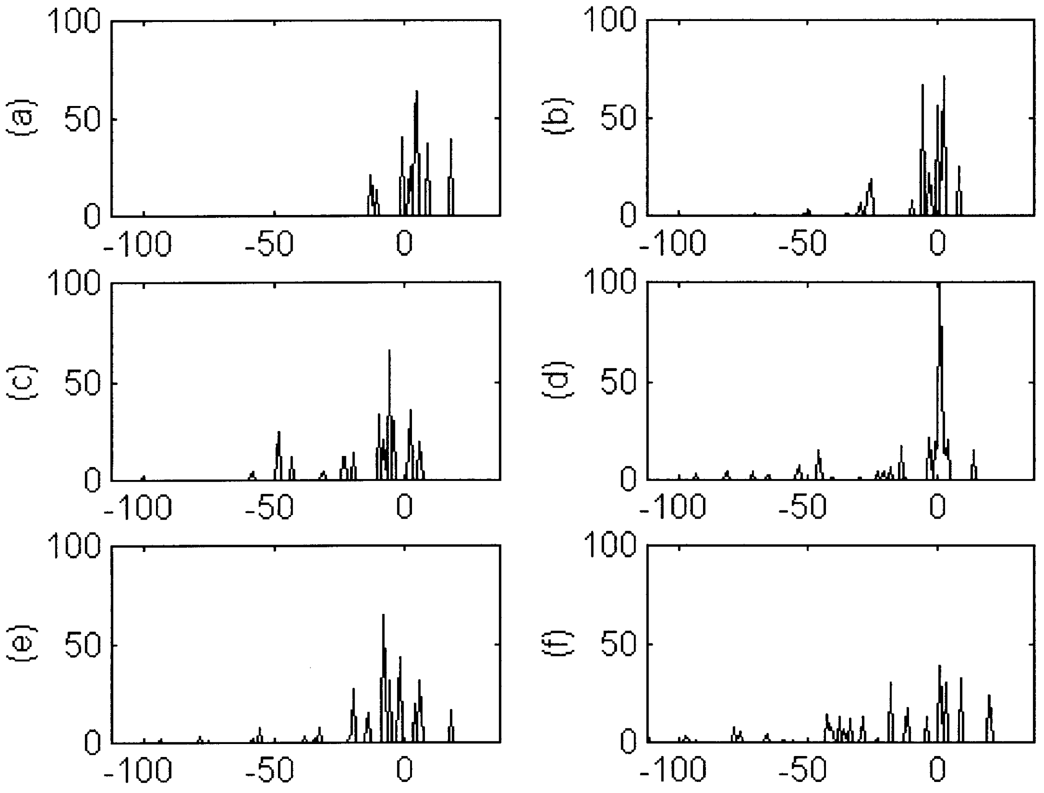

Figure 4- 16 : Plots of Number of occurrences vs height variation about 0 (given in dh units) for the case of random sized rectangle packing (a) lowest fit (σ=8.0010); **(b) lowest fit w/ area minimization** (σ=11.7151); **(c) first fit** (σ=17.3375); **(d) first fit w/ descent** (σ=22.0667); **(e) minimized area fit dh=50** (σ=18.0051); **(f) minimized scaled area fit** (σ=28.6165).

From the above and Table 4- 4, it can be concluded that the performance of the lowest fit packing scheme, does indeed out-perform all the other packing methodologies, in both packing polygonal as well as rectangular shaped objects. This method, unlike the other methods, does not require the explicit use of the stability limiting parameter dh, as the function implicitly causes uniform stratified packing. This helps reduce the percentage of rejected objects and provides for a more "natural" packing structure. Further quantitative studies would be required to establish the fundamental influencing parameters for each of the above packing schemes.

Table 4- 4 : Packing algorithm performance description

Packing Scheme	Mean Charge % w/o rotation (w/ rotation)	Number of objects presented	Number of objects packed	Stability: Standard deviation about reference (units dh)	Performance Index
	d	N_1	N_2	σ	$\sigma/(d\bullet N_2/N_1)$
Random Polygons					
Lowest fit	75.72 (79.22)	206	204	5.663	0.0755
Lowest fit w/ area minimization	75.37 (78.93)	207	203	6.4583	0.0874
First fit	66.05 (69.25)	225	175	18.0159	0.3507
First fit w/ descent	65.78 (68.9)	241	173	16.7	0.3537
Area minimization dh=20	75.83 (79.26)	232	204	11.3769	0.1706
Area minimization dh=50	71.18 (74.45)	220	192	20.8872	0.3362
Area minimization dh=200	62.62 (65.57)	195	169	28.1290	0.5183
Area(volume) scaling with lowest fit with modified contact fit minimization	73.88 (76.91)	228	200	14.6023	0.2253
Random Rectangles					
Lowest fit	89.51	131	130	8.0010	0.0901
Lowest fit w/ area minimization	89.18	131	130	11.7151	0.1324
First fit	90.93	168	132	17.3375	0.2427
First fit w/ descent	90.46	180	131	22.0667	0.3352
Area minimization dh=50	87.91	130	117	18.0051	0.2276
Area(volume) scaling with lowest fit with modified contact fit minimization	86.9	140	125	28.6165	0.3688

4.4. 3-D bin Packing

It is possible to directly extend to the third dimension where all packing rules and philosophies for the 2-D case hold true. Based on the rather large search space (the entire crucible), analogous 3-D studies (as those described in section 4.3.4 for the 2-D case) have not been performed. For the RACS process, this search space is modified to an annulus of characteristic packable nugget width and the center is bulk filled with a bulk filler [Leier] designed to be controlled independent of active vision feedback. Hence, the task is substantially reduced and can be processed in the desired time (1s), accommodated by modifying the search space equation.

For the 3-D simulation, a virtual cylinder is used to emulate the 3-D bin (crucible) and the nuggets are generated as before, but now consisting of a matrix of height values, similar to that seen in Figure 4- 1. The general shape used is that of a random polyhedron, with characteristic dimensions limited by the sample nugget set provided by SEH. In order to allow for non-rectangular projected shapes, the square nugget image matrix is allowed to contain zero values in the visible upper and lower image matrices. The simulation treats this virtual image as the real image, described in Chapter 3. In locating a feasible position, the simulation cost function does account for these zero values. In the physical case, this can be determined only by the NGA mapped lower-nugget-half image matrix, as a zero value in the bottom imaged half, would physically force a zero value in the corresponding unmapped upper-nugget-half.

This 3-D simulation is directly applied to the physical RACS system, by replacing the virtual image matrix, with images obtained from the SGA and the NGA. These images are compensated in two ways. First, image resolution changes based on the height of the object mapped (as can be seen for the crucible in Appendix E). In order to be able to make a justifiable comparison, both the nugget image and the crucible image must be brought to a common resolution. Bilinear interpolation techniques are used to approximate the images to an evenly spaced matrix with 1mm resolution. Future tests may reduce this resolution to 2mm or larger. Second, the simulations assume complete knowledge of the nugget geometry on the visible side. In the physical system, this is limited to the angle of the incident light as described in Chapters 2 and 3. Any surface feature that has a slope greater than the incident laser light angle, cannot be mapped. Additionally, the incident angle helps define and is limited by the system resolution where a vertical or 90° incident angle reduces the resolution to infinity. In order to resolve this blind spot, the packing algorithm extrapolates the image assuming worst case behavior, defining the blind spot as a region with a slope equal to that of the incident laser angle. The other extreme, is to extrapolate the blind spot to a region with vertical or 90° slope. In both cases the blind region slope is extended to the level of the next visible section. The primary concern, with the two extremes is compliance in placement and nugget shifting. Due to the clear errors in these extrapolation extremes, nugget placement is likely to yield a physically overlapping solution that will need to be resolved with manipulator compliance [Calzaretta]. These two extremes can be qualified, by a more sophisticated imaging system, as described in Chapter 3 and Appendix D.

Simulation results for the generalized packing of a 36" diameter crucible, where full crucible packing is done, yields an average charge density of 53.6% (and 57.5% with a 3 d.o.f. wrist for 6 d.o.f. nugget placement) using the lowest fit packing algorithm. This charge holds true for all crucible sizes, as no specifics were applied. By forcing the packable region to be limited to an outer nugget annulus, and higher charge density bulk fill to be placed in the center, the net charge is expected to increase to above 60% for the 36" diameter crucible. The expected charge by SEH for the 36" diameter crucible is 59.7% and for the 18" diameter crucible is 49.8% [Dubowsky]. Based on this, it can be seen that the lowest fit packing algorithm does indeed provide results comparable to those done by humans and maintains the feasibility of the RACS.

Chapter 5. Conclusions

5.1. System Integration--Manipulator Communication and Scheduling

In order to achieve successful operation of the RACS system, it is necessary to integrate the vision system with the packing algorithm and the manipulator. The packing procedure will need to be implemented playing a supervisory role, governing the activities of the four major subsystem outlined in Chapter 1 and Table 1-2. This packing procedure will help coordinate and schedule the activities of the subsystems in order to provide for successful manipulator-vision-packing interaction. Scanning of the crucible is only required during the process of individual nugget packing and can be performed only when the manipulator is outside the field of view. Likewise, the NGA scans the nugget surface only when a packable nugget is grasped and presented to the NGA. These maps must be brought into a common crucible and manipulator coordinate frame for the packing algorithm to resolve an acceptable placement solution. Further, the algorithm must provide an indicator of bulk fill initiation. This is expected to be carried out when nugget rejection is triggered. In the lowest fit algorithm, nugget rejection is only possible if an explicit nugget stability parameter dh is applied (as described in Chapter 4). This parameter controls the maximum relative vertical placement position of the nugget with respect to the ground profile and can be used to determine the activation of bulk fill.

Bulk fill [Leier] will be carried out in a series of n^2 discrete stages, where n is an integer. The bulk fill region is divided into n x n regions, each partially overlapping its neighbors and being packed individually with bulk fill [Leier; Tata]. Timing of these events will be required by the scheduling procedure, mentioned above. Bulk fill is carried out independent of the vision system, and is designed to provide a consistent packing procedure, with the flexibility required for ease of operation change.

In order to provide for accurate scheduling, the governing system needs to communicate with the four major subsystems, either across computers or across programs. It is recommended that the factory level system be operated by a central workstation in order to maintain simplicity. For inter-computer communication, a series of asynchronous handshaking protocols have been developed, that read and write signals in order to communicate information. The following communication signals are required for the vision system and the packing algorithm with the manipulator to correctly coordinate their activities:

- Initiate NGA module for nugget scan using on-line timing
- Initiate SGA model for crucible surface profiling
- Initiate packing algorithm for image extraction and placement
- Transfer of command with nugget position and orientation placement coordinates

Each of the above four signals can be implemented as software asynchronous handshaking protocols. Additionally, the first two signals can also be obtained using a hardware trigger. The flexibility of the system allows for multiple options in further design of the factory level RACS system. From the vision and packing perspective, the task then reduces to scanning when a command signal is received and providing a corresponding placement solution to the manipulator.

5.2. Future Work

- Currently the process of image extraction is limited to segregating the data of consideration based on a reference plane. This can exclude the wrist and manipulator from the image as known rigid objects. The process of eliminating overhanging suction cups used by the gripper is still partially undefined. Reflection characteristics are being studied, but are limited, as the cups eventually get coated with a fine layer of silicon dust, thus changing surface reflection characteristics. Feature extraction, is not entirely a feasible option due to added computational complexity and deformable shape of the cups. An additional option, though involving a moderate computational complexity, would be to use a color NGA camera and acquire a 2-D image of the grasped nugget and project the 3-D map onto this image. Thus a color differentiation process could eliminate overhanging non-nugget features.
- Crucible inner ring image extraction can provide additional complexities that need to be addressed. The crucible is made from fused silica (see Appendix H properties), and has two reflective layers (one with diffuse characteristics and the other with specular characteristics). This makes it a little more difficult to analyze due to spurious reflections. In this single case, it would be required to fit the crucible outline with a circle of corresponding radius in order to be able to extract the crucible image. However, no compensation would suffice if the crucible is mounted at an angle resulting in a blind region and an exposed wall layer. Ideally, the wall would not be visible by the camera (especially while using a telecentric video lens), thus eliminating these considerations. However, if mounting misalignments occur that are

greater than the system resolution, then the visual data acquired and the packing algorithm will be compromised. Hence, mounting schemes need to be explored.

- As described in Chapter 3, in order to simplify the coordinate transformation between the SGA and the manipulator, the SGA would be oriented in order to remove the 3 rotational unknowns. This will be accomplished using a rotab and a 2 axis gimbal platform, that can be adjusted till all resolvable angular discrepancies are eliminated.
- Compensating for blind spots will require further study in order to understand the manipulator's responses to the rigid yet fragile environment. The two extremes that are possible in interpreting blind spots (as described in section 4.4) will be modified based on the manipulator's compliance and the reaction of the environment based on this compliance. In the first extreme, the blind spot can be interpreted as a spatial region with slope equal to that of the incident light, and in the second extreme, as a spatial region with slope of 90°.
- Further analysis on bilinear interpolation will be required in order to see the effects on packing density if the resolution drops down from 1mm to 2mm, or even lower. This can be studied in both the virtual and physical environments. In the physical environment the manipulator's compliance, once again, may prove to be a limiting factor, due to the existence of sub millimeter nugget features that may interact at the macroscopic level with non-trivial forces.
- In order to reduce unfeasible solutions that result in nugget bridging (where a nugget layer can statically self support itself due to high contact forces, which can be detrimental during the melting process), a modified packing algorithm may be required, that forces a decrease in charge density as a function of height, thus

reducing the probability of bridging. Additionally, it has been speculated that this will not be an issue of contention in the packing of the larger 36" diameter crucibles. It would be efficacious to understand this phenomenon in greater detail, and thus determine the crucial dimensions, features etc.

5.3. Summary

In the automation of the crucible packing process of the CZ semiconductor wafer production procedure, which involves the delicate manipulation and placement of polycrystalline silicon nuggets into a stiff and fragile fused silica crucible, a Robot Assisted Crucible charging System (RACS) has been proposed. Key elements in this design involve a non-intrusive nugget and crucible surface geometry acquisition module, a nugget placement and packing algorithm, a manipulator with sufficient compliance and accuracy in the delicate positioning of the nugget, and a universal gripper mechanism that can successfully acquire nuggets of arbitrary shape and orientation.

A non-contact 3-D surface geometry measuring system has been developed based on the principal of optoelectronic active laser triangulation after a thorough investigation of all non-intrusive range sensing methodologies. This system measures both the nugget geometry profile and the internal crucible geometry profile, with a resolution of 1mm and scanning times of 2.5s and 4.5s respectively. Several optional designs have been presented for both cases, in order to improve resolution and reduce blind regions.

Additionally, a novel on-line, multidimensional, flexible packing algorithm has been developed based on the principal of Virtual Trial and Error and extensively tested by simulation for cost function optimization. Four general cost function principals were tested in six critical combinations in a two dimensional version of the packing algorithm.

The final choice of lowest fit is shown to have the best performance index (defined as the stability parameter divided by the product of charge density and the count ratio). For random non-convex polygonal shaped objects, this algorithm produced an average packing charge of 75.72% (with an improvement of over 3% with an added rotational degree of freedom for nugget placement) and a stability parameter of 5.663, with a final performance index of 0.0755 (in dh or stability limiting parameter units). For comparison, the algorithm with all six packing schemes, has been applied to random sized rectangular objects, where the lowest fit cost function is found to give an average packing charge of 89.5%. Although the performance index of the lowest fit scheme did prove to excel in both the polygonal shapes and rectangular shapes, it is found that the first fit scheme outperformed (in terms of charge density) the lowest fit in the case of rectangular object packing.

This final packing algorithm scheme has been applied to the 3-D case and a charge density of 57.5% (with three rotational degrees of freedom) for the entire crucible is obtained. This number is expected to increase to about 60% when allowances for central high charge density bulk fill are made. This compares well with the expected performance of human packing of 36" diameter crucibles yielding 59.7% charge density, and exceeds the performance of human packing of 18" crucibles yielding 49.8%.

Further work in system integration, image extraction and blind spot compensation needs to be performed in order to solve the RACS requirements of a vision system and nugget placement packing algorithm. However, the key technology and requirements have been successfully demonstrated to provide for a feasible solution, for the automation of the crucible charging process in the CZ semiconductor wafer production procedure.

References

1. Antonsson, E.K. *A Three-Dimensional Kinematic Acquisition and Intersegmental Dynamic Analysis System for Human Motion.* PhD. Thesis, Massachusetts Institute of Technology, Cambridge, MA 02139, June 1982. Dept. of Mechanical Engineering.

2. Antonsson, E.K. *3-D surface geometry measurement and analysis.* Engineering Design Research Laboratory Report EDRL-TR 90b, California Institute of Technology, Pasadena, CA 91125, 1990.

3. Antonsson, E.K. *Apparatus for measuring three-dimensional surface geometries.* Application filed January, 1989. Patent number 4,957,369, September 1990.

4. Antonsson, E.K. and R.W. Mann. *Automatic 6-D.O.F. kinematic trajectory acquisition and analysis.* ASME Journal of Dynamic Systems, Measurement and Control, 111(1): 31-39, March 1989.

5. Azar, Y. and L. Epstein. *On Two Dimensional Packing.* Journal of Algorithms, 25, 290-310 (1997).

6. Berkey, J.O. and P.Y. Wang. *A Systolic-Based Parallel Bin Packing Algorithm.* IEEE Transactions on Parallel and Distributed Systems, Vol. 5, No. 7, July, 1994. 769-772.

7. Besl, P.J. *Active, Optical Range Imaging Sensors.* Machine Vision and Applications, 1(2):127-152, March 1989.

8. Bossiuex, T.A. *Integration of Vision and Robotic Workcell.* Ford Motor Company, 1993. American Institute of Aeronautics and Astronautics Publication. AIAA-94-1186-CP

9. Calzaretta, J. *Delicate manipulation of rigid irregular objects in a stiff fragile environment.* Masters of Science thesis, Massachusetts Institute of Technology, Cambridge, MA 02139, June 1998. Dept. of Mechanical Engineering.

10. Chang, E-C., W. Wang and M.S. Kankanhalli. *Multidimensional on-line bin packing: An algorithm and its average-case analysis.* Information Processing Letters 48 (1993) 121-125.

11. Cheng, H.H. and R. Penkar. *Stacking Irregular-Sized Packages by a Robot Manipulator.* IEEE Robotics and Automation Magazine. December 1995. 12-20.

12. Chao, H-Y., M.P.Harper and R.W. Quong. *A tight lower bound for optimal bin packing.* Operations Research Letters 18 (1995) 133-138.

13. Coffman, E.G. and P.W. Shor. *Packing in Two Dimensional Asymptotic Average-Case Analysis of Algorithms.* Algorithmica (1993) 9:253-277.

14. Dowsland, K.A. and W.B. Dowsland. *Packing Problems.* European Journal of Operational Research 56, 2-14.

15. Dubowsky, S. *Robot Assisted Crucible Charging System - Year II Progress Report.* Shin-Etsu Handotai, Co. Ltd., Japan. December 4, 1997.

16. Everett, H.R. *Sensors for Mobile Robots Theory and Applications.* A.K. Peters. Ltd. 1995.

17. Farritor, S. *On modular design and planning for field robotic systems.* PhD. thesis, Massachusetts Institute of Technology, Cambridge, MA 02139, June 1998. Dept. of Mechanical engineering.

18. Galambos, G. *A 1.6 lower-bound for the two-dimensional on-line rectangle bin-packing.* Acta Cybernetica, Tom. 10, Fasc 1-2, Szeged, 1991. 21-24

19. Galambos, G. , H. Kellerer and G. Woninger. *A Lower Bound for On-Line Vector-Packing Algorithms.* Acta Cybernetica, Vol 11, No. 1-2, Szeged, 1993. 23-34.

20. Georgis, N., M. Petrou and J. Kittler. *A New Algorithm for The Constrained Rectangle Packing Problem.* International Conference on Automation, Robotics and Computer Vision (ICARCV) 16-18 September, 1992.

21. Grove, E. *Online Bin Packing with Lookahead.* Proceedings of the 6th annual ACM-SIAM Symposium on Discrete Algorithms. 1995. 430-6

22. Han, B.T., G. Diehr and J.S. Cook. *Multiple-type, two-dimensional bin packing problems:Applications and algorithms.* Annals of Operations Research 50 (1994) 239-261.

23. Hecht, E. *Optics.* 2nd edition, Addison Wesley, May 1990.

24. Holmes, R. and C. Cummings. *How to choose the proper illumination source.* Techspec--Photonics news and information. Edmund Scientific. Issue 3, Vol 2, Winter 1997-98.

25. Hsueh, W.J. *High Resolution Optoelectronic and Photogrammetric 3-D Surface Geometry Acquisition and Analysis.* PhD. Thesis, California Institute of Technology, Pasadena, CA 91125, June 1993. Dept. of Mechanical Engineering.

26. Hsueh, W.J. and E.K. Antonsson. *An optoelectronic and photogrammetric 3-D surface geometry acquisition system.* ASME Winter Annual Meeting on

Instrumentation and Components for Mechanical Systems. ASME, November 1992. EDRL-TR 92a.

27. Hwang, S-M., C-Y.Kao, and J-T.Horng. *On Solving Rectangle Bin Packing Problems Using Genetic Algorithms.* IEEE International Conference on system, Man, and Cybernetics. Humans, Information and Technology. 1994. Vol 2 1583-90.

28. Jarvis, R.A. *A perspective on range finding techniques for computer vision.* IEEE Trans. Pattern analysis and Machine Intelligence. PAMI-5(2):122-139, March 1983.

29. Kanade, T., H. Kano, S.Kimura, A.Yoshida, and K.Oda. *Developemnt of a Video-Rate Stereo Machine.* Proceedings of International Robotics and Systems Conference (IROS '95). August 5-9, 1995, Pittsburg, PA.

30. Kanade, T. and H. Asada. *Non-contact visual three dimensional ranging devices.* SPIE 3-D Machine Perception. 283:48-53, 1981.

31. Kleindiek, S. and K.H.Herrmann. *A miniaturized scanning tunneling microscope with large operation range.* Rev. Sci. Instrum. 64 (3), March 1993. American Institute of Physics.

32. Leier, A. *Grasping and manipulation of irregular shaped objects with application to the semiconductor industry.* Masters of Science thesis, Massachusetts Institute of Technology, Cambridge, MA 02139, June 1998. Dept. of Mechanical Engineering.

33. Li, K. and K.H. Cheng. *Heuristic Algorithms for On-Line Packing in Three Dimensions.* Journal of Algorithms, 13, 589-605 (1992).

34. Luo, R.C. and R.S.Scherp. *3D Object Recognition Using a Mobile Laser Range Finder.* IEEE International Workshop on Intelligent Robots and Systems. IROS '90:673-677.

35. Pargas, R.P. and R. Jain. *A Parallel Stochastic Optimization Algorithm for Solving 2D Bin Packing Problems.* Proceedings of the 9th conference on Artificial Intelligence for Applications. 1993. 18-25.

36. Portmann, M-C. *An Efficient Algorithm for Container Loading.* Methods of Operations Research. 1991. 563-72

37. Rosandich, R.G. *Intelligent Visual Inspection.* Chapman and Hall, London. First edition, 1997

38. Rioux, M. *Laser range finder based on synchronized scanners.* Applied Optics 23(21):3837-3844. November 1, 1984.

39. Sarkar, U.K., P.P.Chakrabarti, S. Ghose, and S.C. DeSarkar. *Improving Greedy Algorithms by Lookahead-Search.* Journal of Algorithms, 16, 1-23 (1994).

40. Schiermeyer, I. *Reverse-Fit: A 2-Optimal Algorithm for Packing Rectangles.* Algorithms - ESA '94. Second Annual European Symposium Proceedings. 1994. 290-9.

41. Series 650X Mirror Positioning System--Instruction Manual. Revision 8, January 27, 1993. Cambridge Technology Inc. Cambridge, MA 02138.

42. Shor, P.W. *The Average Case Analysis of Some On-Line Algorithms for Bin Packing.* 25th Annual Symposium on Foundations of Computer Science. P xii+518, 193-200. 1984.

43. Stoyan, Y.G., M.V. Novozhilova, and A.V. Kartashov. *Mathematical model and method of searching for a local extremum for the non-convex oriented polygons allocation problem.* European Journal of Operational Research 92 (1996) 193-210.

44. Tata, M. *Personal communications.* Massachusetts Institute of Technology, Cambridge, MA 02139. Dept of Mechanical Engineering. 1997-1998

45. Whelan, P.F. and B.G.Batchelor. *Automated packing systems : Review of industrial implementations.* SPIE Vol 2064: 358-368

46. Whelan, P.F. and B.G.Batchelor. *Development of a vision system for the flexible packing of random shapes.* SPIE Vol. 1823 (1992)/223-230.

47. Whelan, P.F. and B.G. Batchelor. *Flexible packing of arbitrary two-dimensional shapes.* Optical Engineering. December 1993/ Vol. 32 No 12. 3278-3287.

48. Whelan, P.F. and B.G.Batchelor. *Automated Packing Systems - A Systems Engineering Approach.* IEEE Transactions of Systems, Man and Cybernetics--Part A: Systems and Humans, Vol. 26, No. 5 September, 1996. 533-543.

49. Yang, W. *Circuit integration pushes image sensor performance.* Laser Focus World, Feb 1997, Vol 33, No. 2, 129-139.

Appendix A

Minimization of e(S₁,S₂) w.r.t. S₁ and S₂

Let:

$e(S_1,S_2)=S_1\,\mathbf{R_1} - S_2\,\mathbf{R_2} - \mathbf{R_d}$

$\mathbf{R_1} = [x_1,y_1,z_1]^T$

$\mathbf{R_2} = [x_2,y_2,z_2]^T$

$\mathbf{R_d} = [x,0,0]^T$

$$\vec{e}\cdot\vec{e}=\begin{bmatrix} S_1x_1-S_2x_2-x \\ S_1y_1-S_2y_2-0 \\ S_1z_1-S_2z_2-0 \end{bmatrix}\cdot\begin{bmatrix} S_1x_1-S_2x_2-x \\ S_1y_1-S_2y_2-0 \\ S_1z_1-S_2z_2-0 \end{bmatrix}$$

Which gives:

$(S_1\,x_1 - S_2\,x_2 - x)^2 + (S_1\,y_1 - S_2\,y_2)^2 + (S_1\,z_1 - S_2\,z_2)^2$

Minimizing with respect to S_1 and S_2 gives:

$$\frac{\partial(\vec{e}\cdot\vec{e})}{\partial S_1}=S_1(\overrightarrow{R_1}\cdot\overrightarrow{R_1})-S_2(\overrightarrow{R_1}\cdot\overrightarrow{R_2})-(\overrightarrow{R_1}\cdot\overrightarrow{R_d})=0$$

$$\frac{\partial(\vec{e}\cdot\vec{e})}{\partial S_1}=S_2(\overrightarrow{R_2}\cdot\overrightarrow{R_2})-S_1(\overrightarrow{R_1}\cdot\overrightarrow{R_2})+(\overrightarrow{R_2}\cdot\overrightarrow{R_d})=0$$

Now solving these two equations for S_1 and S_2 gives:

$$S_1=\frac{(\overrightarrow{R_1}.\overrightarrow{R_d})(\overrightarrow{R_2}.\overrightarrow{R_2})-(\overrightarrow{R_2}.\overrightarrow{R_d})(\overrightarrow{R_1}.\overrightarrow{R_2})}{(\overrightarrow{R_1}.\overrightarrow{R_1})(\overrightarrow{R_2}.\overrightarrow{R_2})-(\overrightarrow{R_1}.\overrightarrow{R_2})(\overrightarrow{R_1}.\overrightarrow{R_2})} \qquad S_2=\frac{(\overrightarrow{R_2}.\overrightarrow{R_d})(\overrightarrow{R_1}.\overrightarrow{R_1})-(\overrightarrow{R_1}.\overrightarrow{R_d})(\overrightarrow{R_1}.\overrightarrow{R_2})}{(\overrightarrow{R_1}.\overrightarrow{R_2})(\overrightarrow{R_1}.\overrightarrow{R_2})-(\overrightarrow{R_2}.\overrightarrow{R_2})(\overrightarrow{R_1}.\overrightarrow{R_1})}$$

Appendix B

Triangulation Model II

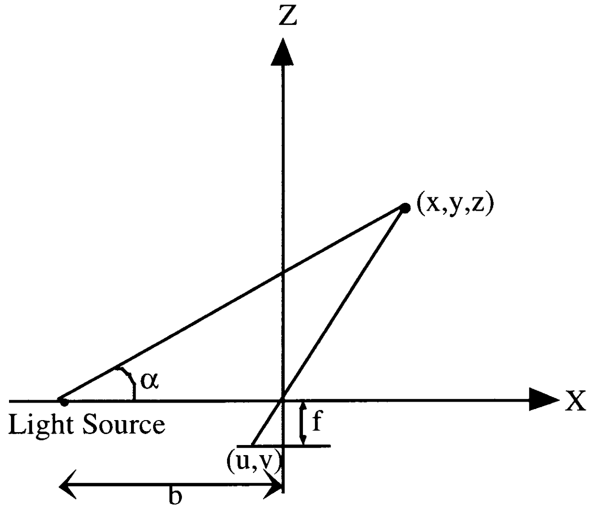

Figure B-1 : Model II Plan view

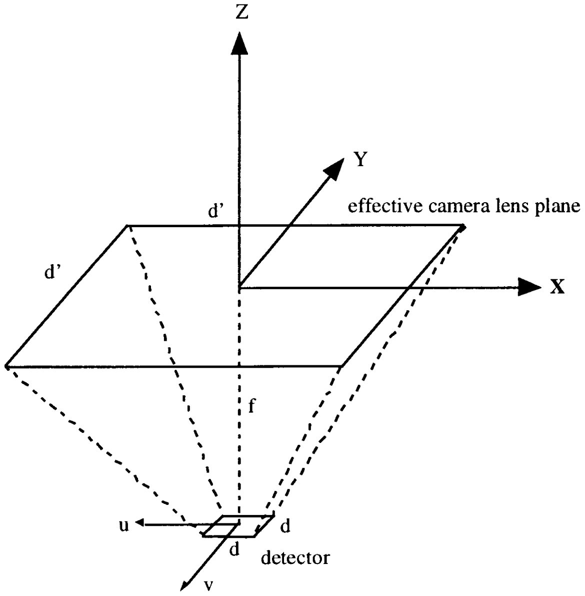

Figure B-2 : Model II orthographic view

$$\tan\alpha = \frac{z}{x+b} \qquad \frac{u}{f} = \frac{x}{z} \qquad \frac{v}{f} = \frac{y}{z}$$ *by similar triangles*

Note that the units of u, v, f are in terms of number of pixels. The dimensions of x, y, and z are hence only dependent of the units of b.

$$\tan\alpha = \frac{fx/u}{x+b}$$

Solving for x we get:

$$x = \frac{b}{f/u\,\cot\alpha - 1} = \frac{ub}{f\cot\alpha - u}$$

Then solving for z we get:

$$z = \frac{fx}{u} = \frac{f}{u}\cdot\frac{ub}{f\cot\alpha - u} = \frac{fb}{f\cot\alpha - u}$$

And finally solving for y we get:

$$\tan\alpha = \frac{fy/v}{x+b}$$

$$y = \frac{v\cdot\tan\alpha\cdot(x+b)}{f} = \frac{v\cdot\tan\alpha\cdot(ub/f\cot\alpha - u + b)}{f} = \frac{vb}{f\cot\alpha - u}$$

As a confirmation check we try solving for z in the other direction:

$$z = \frac{fy}{v} = \frac{fb}{f\cot\alpha - u}$$

Holographic Interferometry

With the compensator in place, C (Figure B-3), any optical path difference arises from the actual path difference. Due to the dispersion of the beam-splitter, the optical path is a function of λ. To understand how the fringes work, Figure B-4 provides an equivalent optical rearrangement. S_1 and S_2 are coherent point sources. The optical path difference for these rays is nearly 2-D cosθ, which represents a phase difference of $k_0$2-D cosθ. An additional phase term arises from the wave traversing the arm OM_2 which is internally reflected in the beam-splitter, whereas the OM_1-wave is externally reflected at O. If the beam splitter is simply an uncoated glass plate, the relative phase shift resulting from the two reflections is π radians. Destructive interference results when:

$$2d\cos 6_m = m\lambda_o$$

where m is an integer for the m^{th} fringe. If this is satisfied for the point S, then it will be well fulfilled for any point on Σ that lies on the circle of radius O'S, where O' is located on the axis of the detector. Hence the p^{th} ring, is determined by:

$$2d(1-\cos\theta_p) = p\lambda_o$$

Since $\theta_m = \theta_p$, both are just the half angle subtended at the detector, by the particular ring. As the movable mirror is displaced by $\lambda_0/2$, each fringe moves to the position previously occupied by an adjacent fringe. The number of fringes, N, that have moved past a reference point determine the distance traveled by the mirror Δd, given by:

$$\Delta d = N(\lambda_0/2)$$

Holographic interferometry uses coherent light to produce interference patterns due to the optical frequency phase differences in different optical paths. If two laser beams (same polarization) meet at a surface point **x**, then the electrical fields add to create the net electrical field:

$$E(x,t) = E_1 \cos(\omega_1 t - \mathbf{k_1}.\ \mathbf{x} + \phi_1(x)) + E_2 \cos(\omega_2 t - \mathbf{k_2}.\ \mathbf{x} + \phi_2(x))$$

where $\mathbf{k_i}$ are 3-D wave vectors pointing in the propagation directions with magnitude $|\mathbf{k_i}|=2\pi/\lambda_i$, the $\omega_t=|\mathbf{k_i}|c$ are the radial optical frequencies, and $\phi_t(\mathbf{x})$ are the optical phases. Since photodetectors respond to the square of the electric field, the detectable irradiance (intensity) is $I(\mathbf{x},t) = E^2(\mathbf{x},t)$. Photodetectors themselves act as low-pass filters of the irradiance function I to yield the detectable interference signal $I'(\mathbf{x},t) = LPF[I(\mathbf{x},t)]$ or:

$$I'(x,t) = E_a\{1 + E_b \cos[\Delta\omega t + \Delta\mathbf{k}.\mathbf{x} + \Delta\phi(x)]\}$$

where

$$E_a = E_1^2 + {E_2^2}/{2} \qquad \text{and} \qquad E_b = \frac{2E_1E_2}{(E_1^2 + E_2^2)}$$

$$\Delta\varpi = \varpi_1 - \varpi_2 \quad \text{is the difference frequency}$$

$$\Delta\vec{k} = \vec{k_2} - \vec{k_1} \quad \text{is the difference wave vector}$$

$$\Delta\phi(\vec{x}) = \phi_1 - \phi_2 \quad \text{is the phase difference}$$

Since holographic interferometry is based on the principals of the Michelson's interferometer, fraction of wavelength distances can be measured. For equal optical frequencies and equal wave vector spatial frequencies, only the phase difference term remains from which surface depth information is recovered. The z-depth spacing of holographic fringes is proportional to the wavelength of light. Measured object surfaces must be very flat and smooth.

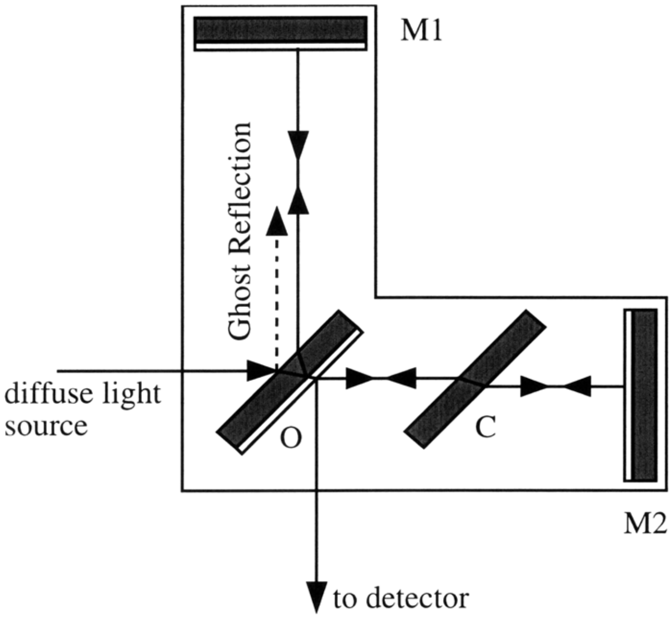

Figure B-3 : Interferometry True Setup

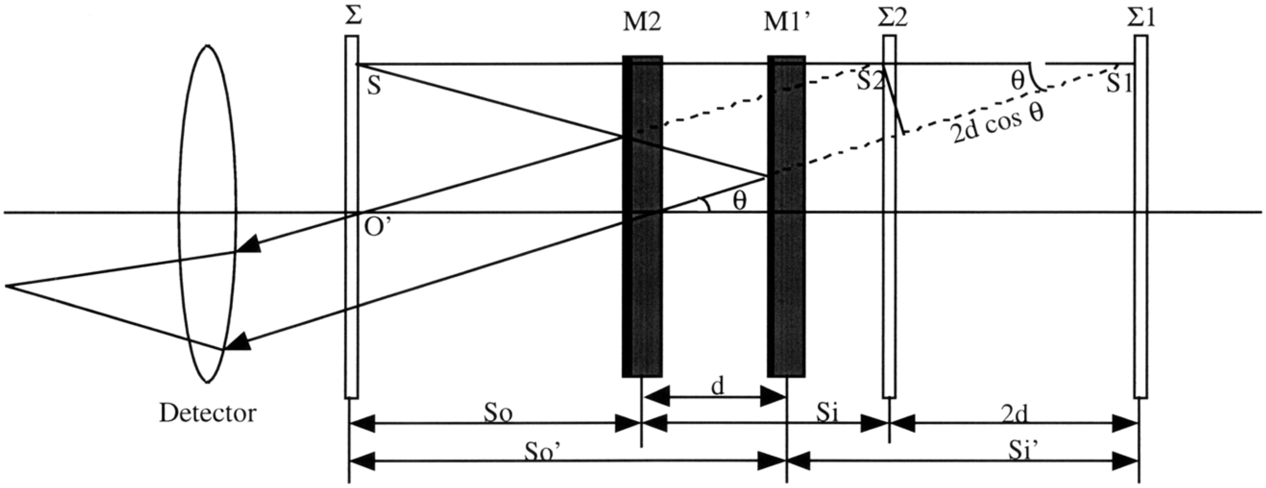

Figure B-4 : Interferometry Equivalent Conceptual Rearrangement

Appendix C

Laboratory Vision System Hardware Specifications

Laser Diode Modules

Edmund Scientific, Barrington, NJ 08007-1380

Wavelength	670nm +/- 10nm
Output	Class IIIa , 3mW
Beam Diameter	2mm
Optics	Line generator optics
Focussing range	20mm to infinity
Beam Size at Nearest Focus	<100µm
Beam Divergence	<0.5mrad
Power supply	4-6VDC; 40-120 mA
Stability	+/- 10% over voltage range
Operating temperature	-10 to 40 °C
Storage Temperature	-20 to 65 °C

CCD Camera

Monochrome Camera P39,244 from Edmund Scientific, Barrington, NJ 08007-1380.

Imaging Device	½" interline transfer CCD
Pixels	510H x 492V
Pixel Size	12.7 x 9.8µm
Horizontal Resolution	>350 TV lines
Sensing Area	6.4 x 4.8 mm
Signal Format	EIA (RS-170);
Video Output	1V p-p, 75W; RCA connector
Lens Mount	C-mount
Flange Back Length	12.5 mm
Sync System	Internal
Min. Sensitivity	0.2 lux
S/N Ratio	>46 dB
Electronic Shutter Speed	N/A
Gamma	0.45
Auto Gain Control	27 dB
Power requirement	12V DC; 200mA max.
Storage/Operating Temp.	-30 to 70°C/-20 to 55°C
Dimensions	30.5 x 30.5 x 61 mm
Mounting	¼-20 TPI tapped
Weight	120g

Scanner

6860 moving-magnet galvanometer from Cambridge technology, Cambridge, MA 01238.

Mechanical Specifications	
Angular Excursion	40 degrees
Rotor Inertia	0.6 g cm^2,+/- 10%
Torque Constant	9.3 x 10^4 dyne-cm/amp, +/1 10%
Max coil Temperature	110°C
Electrical Specifications	
Coil Resistance	1.4 Ohms, +/1 10%
Coil Inductance	350 μH, +/- 10%
Peak Current	25 Amperes, Max
Small Angle Step Response Time	1.0 ms with 0.1 g cm^2 load
Position Detector	
Linearity	99.9% over 40 degrees
Scale Drift	50 ppm/°C
Zero Drift	15 microradians/°C
Jitter	15 microradians
Repeatability	5 microradians
Output Signal, Common Mode	585 μA with AGC Voltage of 10VDC, +/- 20%
Output Signal, Differential Mode	14.5 μA/degree, at common mode current of 585μA
Servo/Amplifier Controller	650 size D rev E1
Position Input Scale Factor	Analog : 0.500 V/degree Digital: 1638 dac counts/degree
Position Output Scale Factor	0.5 V/degree
Non-linearity, 16 Bit Digital Input	0.006% of full scale
Temperature Stability	100 ppm/°C
Input Voltage requirements	+/- 28V
Input Current requirements	Upto 4A
Warm up time	1 minute to rated accuracy
Operating Temp Range	0-50°C

Variable Scan PCI Framegrabber Board DT3152

Data Translation, Marlboro, MA 01752-1192

Spatial Resolution	4-4096 x 1-4096 4M pixels max
Grayscale Resolution	256 levels (8 bits)
Standard Video	(4) RS-170, CCIR
Variable Scan	1KHz - 20 MHz
Host	PCI Bus

Appendix D

SGA Setup Option II

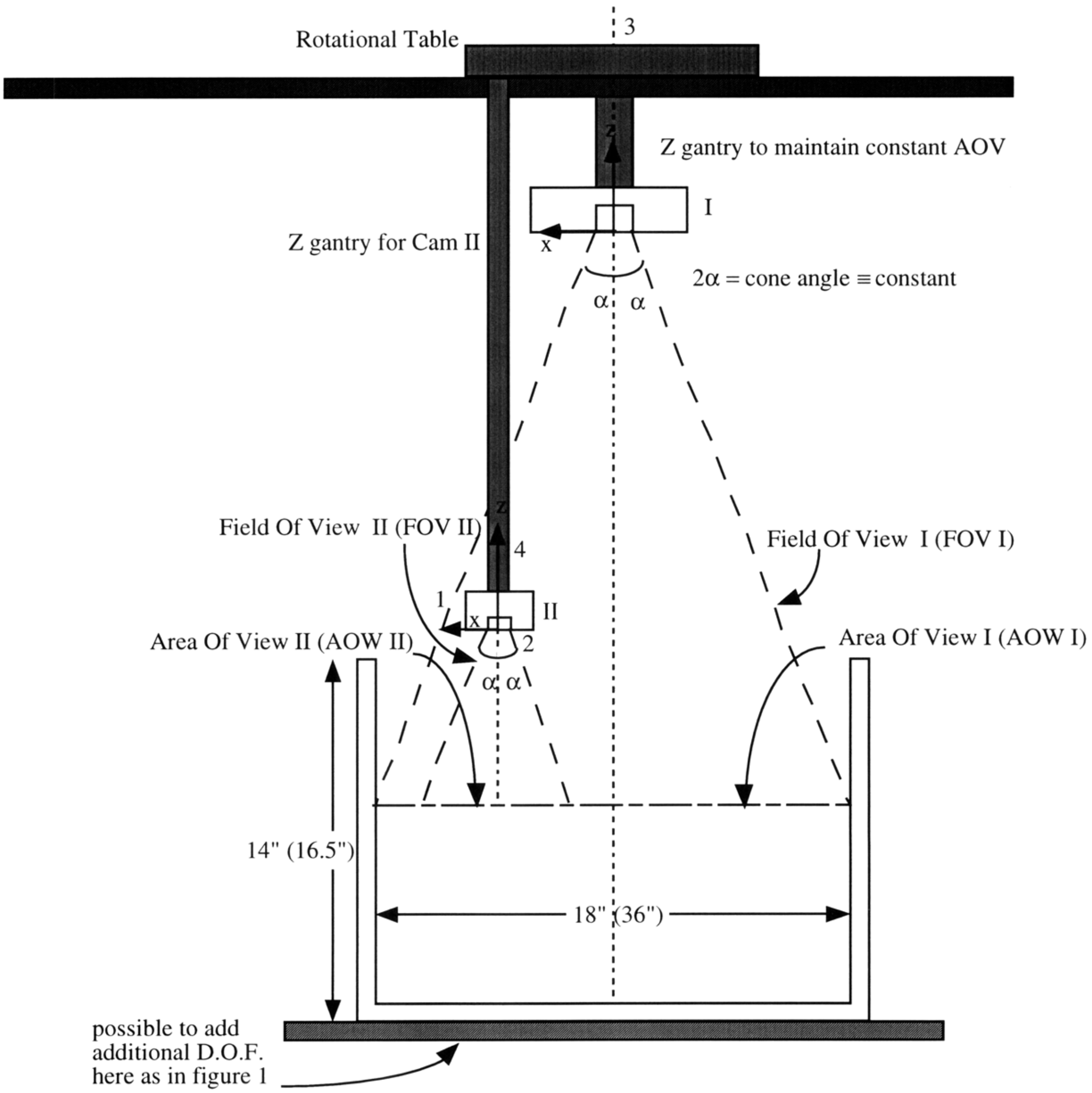

1(about about cam II x) + 2(about cam II y)
+ 3 (about cam I z) - rotations ≡ 3 rotational D.O.F
4 - z translational ≡ 1 vertical D.O.F.

For High resolution camera II

Note : Camera II needs to be pulled out of camera I's FOV when camera I is acquiring data, so as to prevent obfuscation.

Figure D-1 : SGA alternative II

SGA Setup Option III

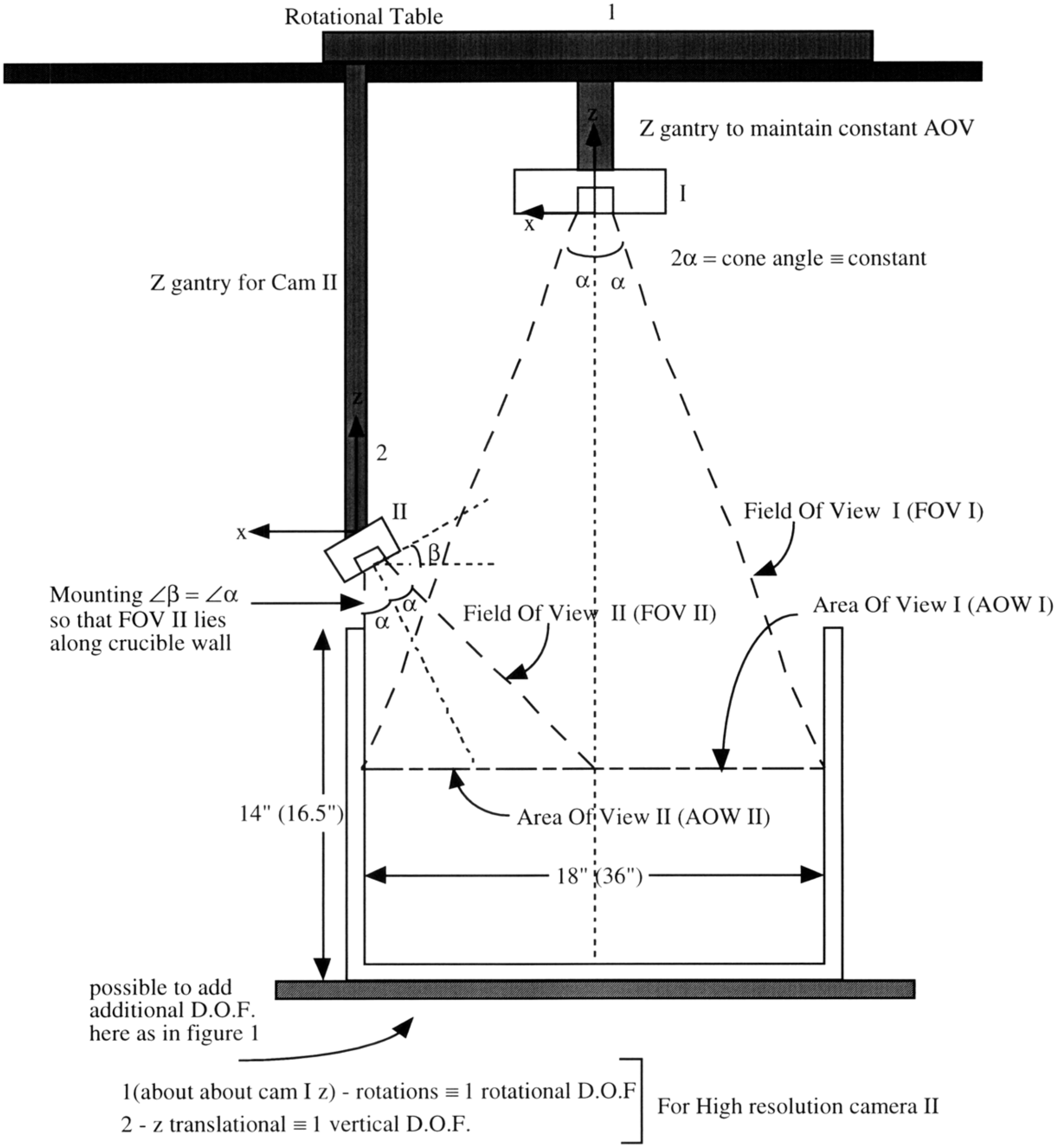

Note:

Camera II needs to be pulled out of camera I's FOV when camera I is acquiring data, so as to prevent obfuscation.

Z gantry for camera II & rotational mount can be just as easily mounted on the ground instead of the ceiling

By raising or lowering camera II, FOVII & AOV II change and so does resolution. Due to rotational + transnational D.O.F. high resolution is possible for any given sector.

Figure D-2 : SGA alternative III

NGA Setup Option II

The manipulator will be used as a positioner of the object and will stay unmoved for a given amount a time, during which, with the aid of an XY scanner system, the object will be mapped with the vision system components. The scanning may entail (i) the positioning of the illumination light or (ii) the positioning of the entire camera subsystem.

NGA Setup Option III

The manipulator will be used as a positioner of the object and will stay unmoved for a given amount of time, during which the object will be mapped using a touch sensor that will either (i) map the object along an XY grid or (ii) map the entire object at once using several parallel coupled sensors.

System Comparisons

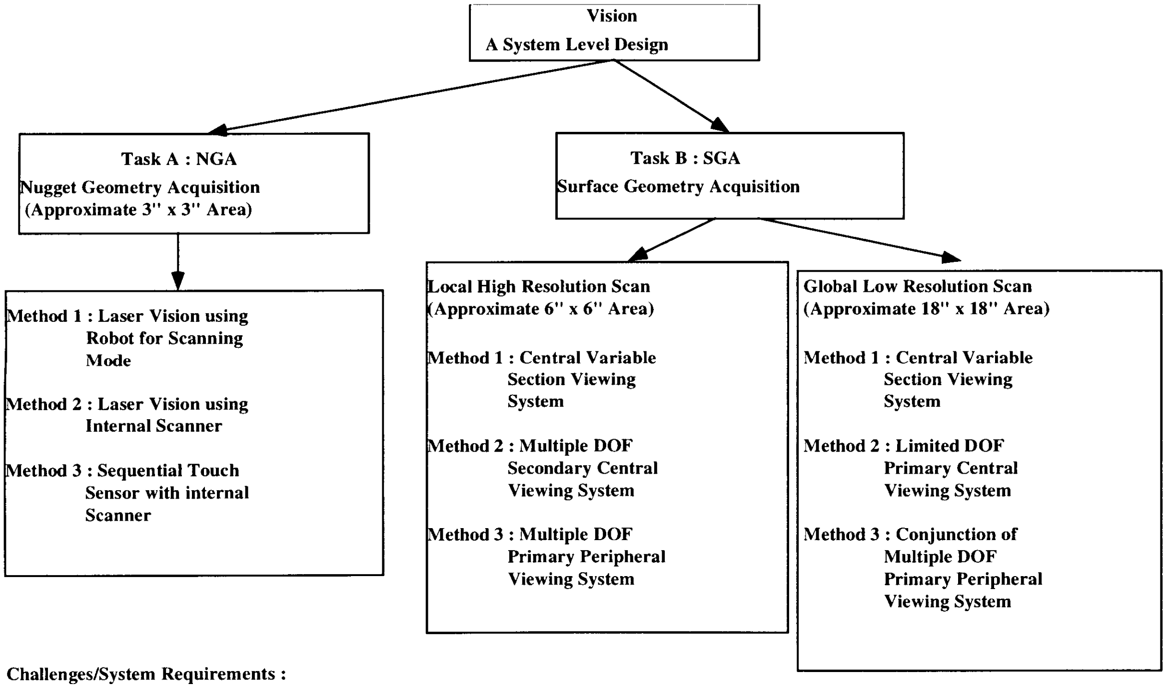

Challenges/System Requirements :
1. Rapid data acquisition and processing
2. High Accuracy and Resolution in the NGA and SGA (1mm)
3. Adaptive data acquisition for variable environment
  - variable reflectance
  - variable surface features
  - minimal computational power
4. Reliability

Appendix E

SGA Setup Option I - Design Parameters

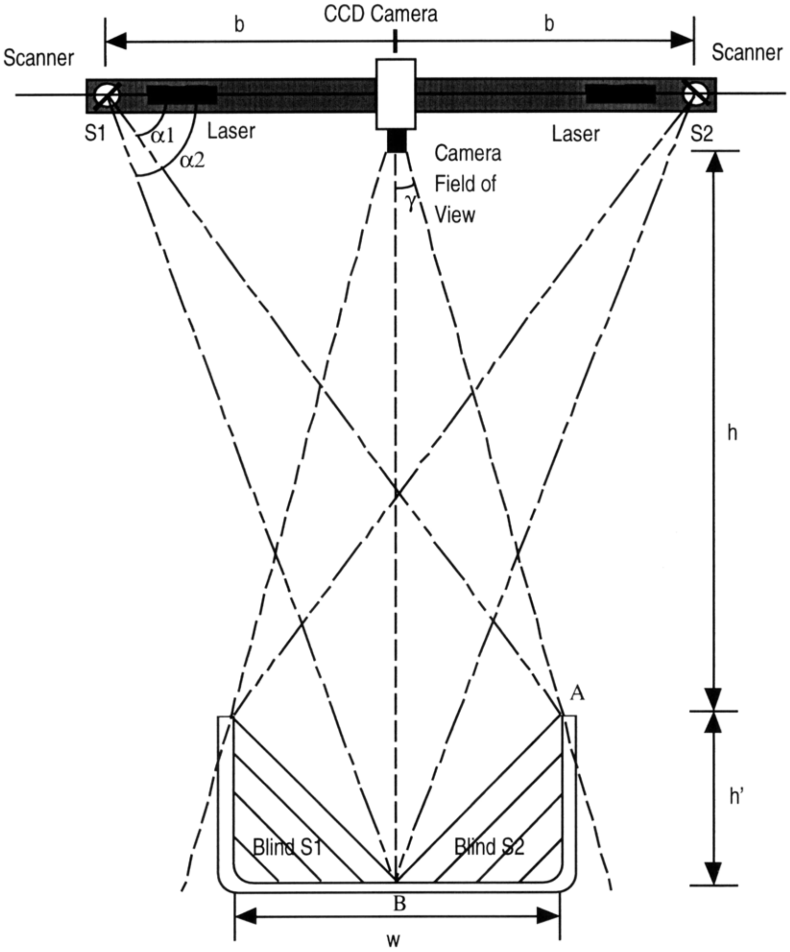

Figure E-1 : SGA design parameters

Parameters	Lab Design	Factory Design
H	54 inches	54 inches
h'	14 inches + crown	23.5 inches + crown
W	18 inches	36 inches
b	36 inches	47 inches
γ	9.5 degrees	22.0 degrees
α1	50.3 degrees	47.9 degrees
α2	63.4 degrees	56.8 degrees
Camera resolution in pixels	500x500	1000x1000
Z Resolution at A	1.1 mm	1.0 mm
Z Resolution at B	2.4 mm	2.3 mm
X,Y Resolution at A	0.9 mm	0.9 mm
X,Y Resolution at B	1.2 mm	1.5 mm

NGA Setup Option I - Physical Parameters

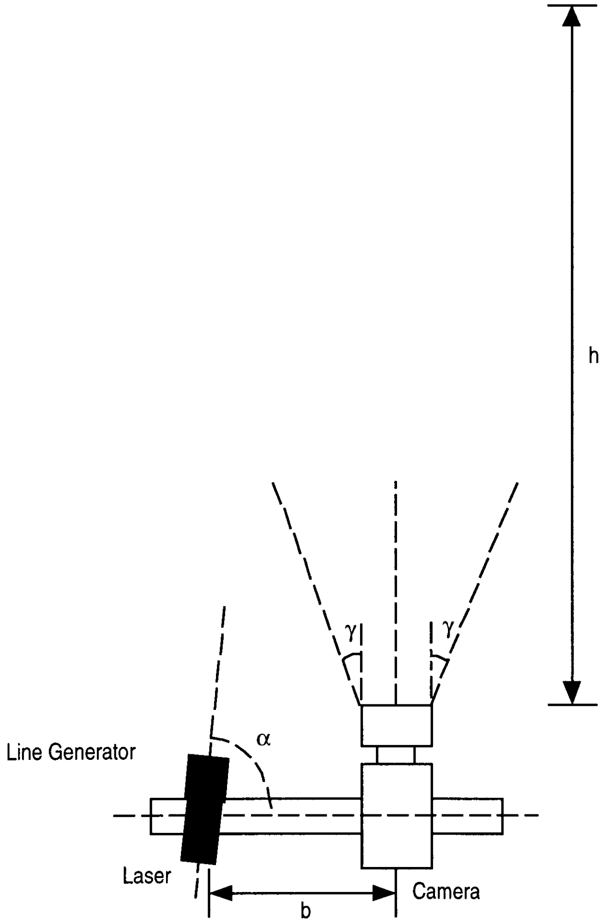

Figure E-2 : NGA design parameters

Parameters	Lab Design	Factory Design
h (dist to object -- nugget)	10 inches	10 inches
b	1.7 inches	1.7 inches
γ	21 degrees	12 degrees
α	70 degrees	84 degrees
Camera resolution in pixels	500x500	1000x1000
Z Resolution	1.07 mm	1.03 mm
X,Y Resolution	0.39 mm	0.11 mm

Appendix F

Circuit for 8 to 16 bit scanner converter

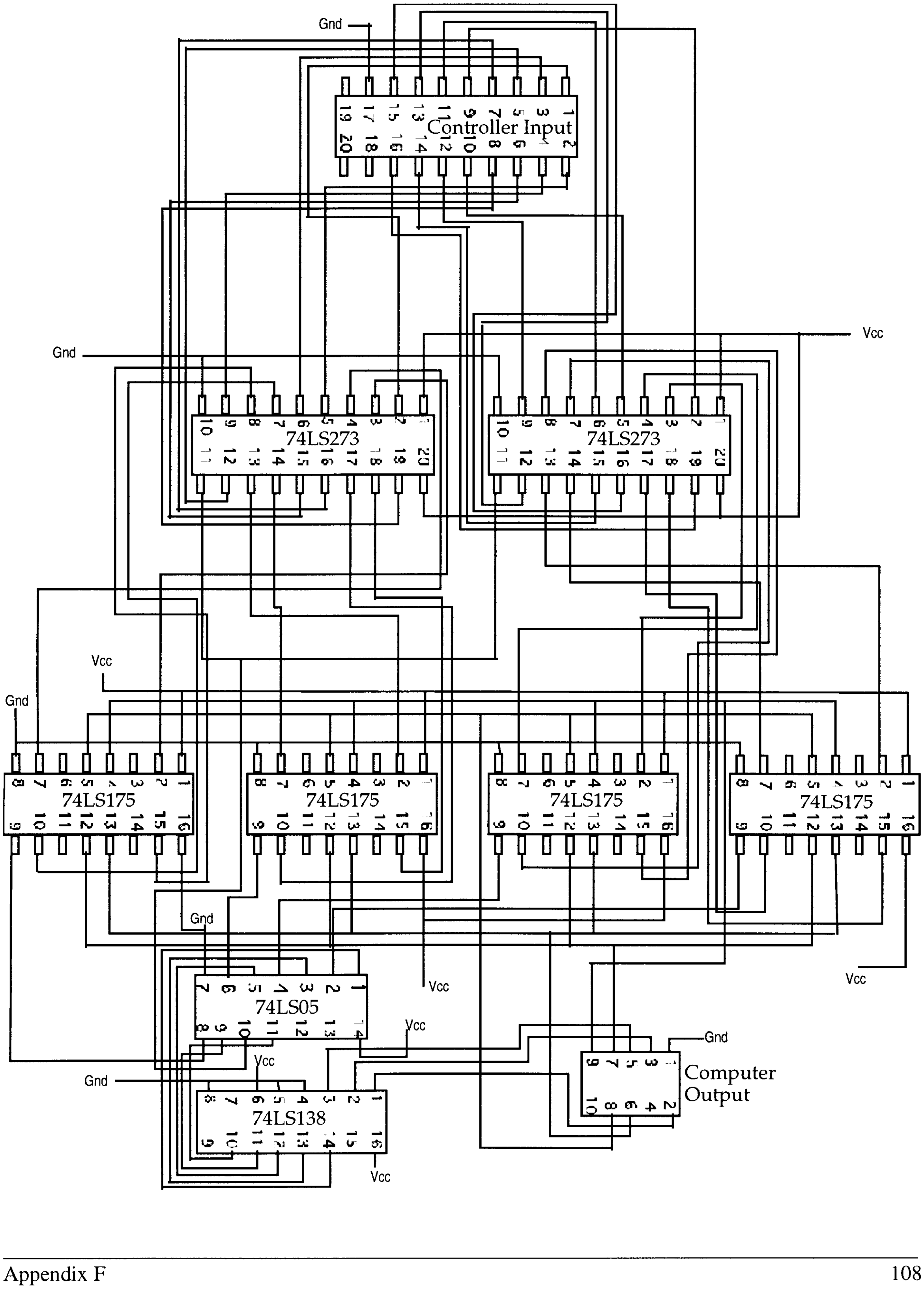

Appendix G

Vision System Calibration Guide (Aluminum) and Slider (Delrin)

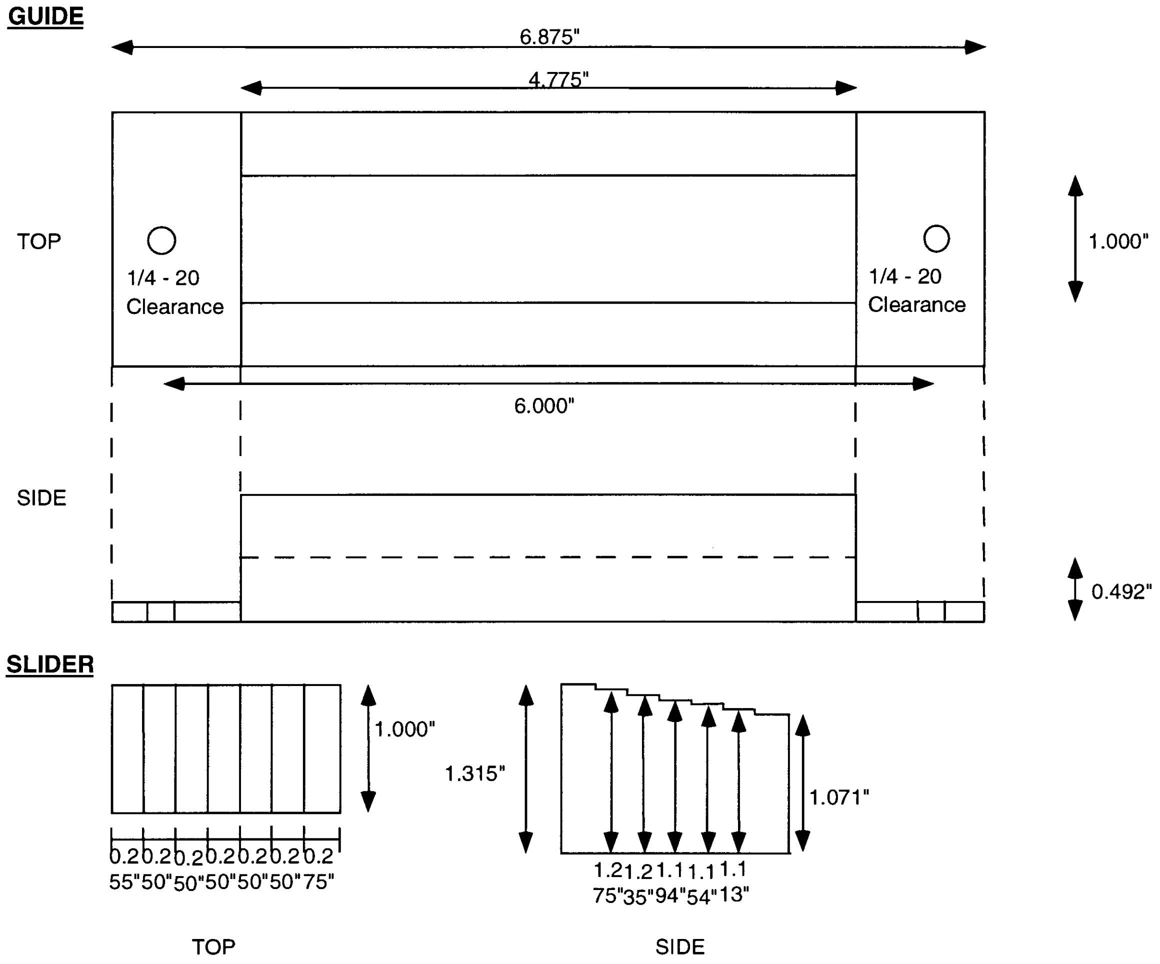

Figure G-1 : Calibration guide and slider

Appendix H

Nugget Distribution Properties for typical charge

Range	Frequency	Percent of Total Mass
<10 gms	**-- (total mass of 3kg)**	**4.9 %**
10-20 gms	**215**	**5.2%**
20-50 gms	**390**	**21.7%**
50-150 gms	**373**	**51.3%**
150-300 gms	**38**	**12.0%**
>300 gms (ranging from 312 to 548 gms)	**8**	**4.9%**

Glass Properties

	Window Glass	Fused Silica
Chemical Description	**72% SiO_2** **14% Na_2O** **10% CaO** **2% MgO** **1% Al_2O_3** **1% Impurities**	**99% SiO_2** **1% Impurities**
Density	**2180 Kg/m^3**	**2200 Kg/m^3**
Modulus of Elasticity	**69 Gpa**	**72 GPa**
Shear Modulus	**30.3 Gpa**	**29.6 GPa**
Poisson's Ratio	**0.23**	**0.17**
Indentation Hardness*	**400-600Kg/mm^2**	**400-600Kg/mm^2**
Moh Hardness*	**4.5 - 6**	**4.5 - 6**
Impact Abrasion Hardness	**1.0**	**3.5**
Tensile Strength*	**30 - 70 Mpa**	**30 - 70 MPa**
Compressive Strength*	**350 Mpa**	**350 MPa**
Working Stress*	**6.6 Mpa**	**6.6 MPa**
Coefficient of Thermal Expansion	**9.2e-6 /Celsius**	**5.6e-6 /Celsius**

*Explicit differences between window glass and fused silica not found